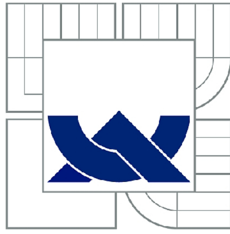

VYSOKÉ UČENÍ TECHNICKÉ V BRNĚ
BRNO UNIVERSITY OF TECHNOLOGY

FAKULTA STROJNÍHO INŽENÝRSTVÍ
ÚSTAV FYZIKÁLNÍHO INŽENÝRSTVÍ

FACULTY OF MECHANICAL ENGINEERING
INSTITUTE OF PHYSICAL ENGINEERING

RŮSTOVÉ DEFEKTY V MONOKRYSTALECH CZOCHRALSKIHO KŘEMÍKU

MICRODEFECTS IN CZOCHRALSKI SILICON

DISERTAČNÍ PRÁCE
DOCTORAL THESIS

AUTOR PRÁCE AUTHOR	Ing. LUKÁŠ VÁLEK
VEDOUCÍ PRÁCE SUPERVISOR	prof. RNDr. JIŘÍ SPOUSTA, Ph.D.
ŠKOLITEL SPECIALISTA EXTERNAL SUPERVISOR	Mgr. JAN ŠIK, Ph.D.

STŘÍTEŽ NAD BEČVOU 2012

Abstrakt
Disertační práce se zabývá studiem defektů v monokrystalech Czochralskiho křemíku legovaných bórem. Práce studuje vznik kruhových obrazců vrstevných chyb pozorovaných na povrchu křemíkových desek po oxidaci. Hlavním cílem práce je objasnit mechanismy vzniku pozorovaného rozložení vrstevných chyb na studovaných deskách a vyvinout metody pro řízení tohoto jevu.

Na základě experimentálních analýz a rozborů obecných mechanismů vzniku defektů jsou objasňovány vazby mezi vznikem defektů různého typu. Tyto jsou pak diskutovány v souvislosti s parametry krystalu i procesu jeho růstu. Takto sestavený model je využit pro vývoj procesu růstu krystalů, kterým je potlačen nadměrný vznik defektů ve studovaných deskách. Za účelem studia defektů jsou zaváděny a vyvíjeny nové analytické metody.

Disertační práce byla vytvořena za podpory ON Semiconductor Czech Republic, Rožnov pod Radhoštěm.

Abstract
The doctoral thesis deals with analyses of defects in single crystals of Czochralski silicon doped with boron. Mechanisms of formation of circular patterns of oxidation induced stacking faults are studied. The main goal of the work is to explain the mechanisms of formation of the observed defect patterns and to develop methods for control of this phenomenon.

Mechanisms of defect formation in silicon are analyzed and the material is experimentally studied in order to explain relations between formation of defects of various kinds and to link these processes to parameters of the crystal and its growth. A qualitative model capturing all these relations is built and utilized to develop an optimized crystal growth process for suppression of excessive formation of the oxidation induced stacking faults. Novel methods are developed and implemented to support effective analyses of crystal defects.

This doctoral thesis was written with the support of ON Semiconductor Czech Republic, Rožnov pod Radhoštěm.

Klíčová slova
Křemík, Czochralski, bór, defekty, vrstevné chyby, precipitace kyslíku

Keywords
Czochralski silicon, boron, microdefects, oxidation induced stacking faults, oxygen precipitation

VÁLEK, L., *RŮSTOVÉ DEFEKTY V MONOKRYSTALECH CZOCHRALSKIHO KŘEMÍKU.* Brno: Vysoké učení technické v Brně, FAKULTA STROJNÍHO INŽENÝRSTVÍ, 2012. 88 s. Vedoucí prof. RNDr. Jiří Spousta, Ph.D.

Prohlašuji, že jsem práci vypracoval samostatně za odborného vedení prof. RNDr. Jiřího Spousty, Ph.D., a Mgr. Jana Šika, Ph.D., a veškeré prameny, ze kterých jsem čerpal, jsou uvedeny v seznamu literatury.

Ing. Lukáš Válek

Děkuji prof. RNDr. Jiřímu Spoustovi, Ph.D., za to, že se mě ujal jako vedoucí disertační práce a pomohl mi projít celým doktorským studiem. Děkuji svému nadřízenému v ON Semiconductor a příteli Mgr. Janu Šikovi, Ph.D., za dlouhodobou podporu mého odborného růstu, podporu práce na tématu doktorského studia a cenné připomínky k textu disertační práce. Poděkování za revizi textu patří rovněž kolegům a přátelům Ing. Davidu Lysáčkovi, Ph.D., a Ing. Petru Kostelníkovi, Ph.D. Všem výše zmíněným patří veliké díky za psychickou podporu v mém disertačním úsilí.

Děkuji svým rodičům za možnost směřovat ve svém životě cestou, která mě dovedla až sem. Děkuji své ženě Zuzce za příjemné a motivující rodinné zázemí, bez něhož by kombinace rodinného života, pracovního nasazení a doktorského studia nebyla možná.

Ing. Lukáš Válek

Contents

1 **Motivation** **3**

2 **Silicon** **4**

3 **Production of silicon for electronics** **7**
- 3.1 Czochralski crystal growth . . . 7
- 3.2 Float zone crystal growth . . . 9
- 3.3 Manufacturing of silicon wafers . . . 10

4 **Defects in silicon** **11**
- 4.1 History . . . 11
- 4.2 Silicon crystal structure . . . 13
- 4.3 Classification and overview . . . 15
  - 4.3.1 Point defects . . . 15
  - 4.3.2 Line defects . . . 20
  - 4.3.3 Planar defects . . . 20
  - 4.3.4 Bulk defects . . . 21
- 4.4 Impact of crystal defects on device yield . . . 24

5 **Formation of grown-in defects in CZ silicon** **25**
- 5.1 Point defects — pathway to crystal defects . . . 25
- 5.2 Spatial distribution of defects . . . 27
- 5.3 Formation of defects in mixed-type crystals . . . 28
- 5.4 The critical v/G ratio . . . 30
- 5.5 OISF ring . . . 30
- 5.6 Oxygen precipitation . . . 31

6 **Methods of studying crystal defects** **34**
- 6.1 Fourier transform infrared spectroscopy . . . 34
- 6.2 Precipitation test . . . 35
- 6.3 Preferential etching . . . 35
- 6.4 X-ray topography . . . 37
- 6.5 OISF test . . . 38
- 6.6 Chromium-free OISF test . . . 38
- 6.7 COP test . . . 39
- 6.8 Copper decoration . . . 39
- 6.9 Computer simulations . . . 41

7 **Engineering of crystal defects in silicon** **42**
- 7.1 Denuding and precipitation of oxygen . . . 42
- 7.2 Wafer annealing . . . 43
- 7.3 Optimization of oxygen concentration . . . 43
- 7.4 Nitrogen doping . . . 45
- 7.5 Vacancy-controlled denuded zone . . . 45
- 7.6 Optimization of v/G . . . 47

8 **Crystal growth simulations in FEMAG** **48**

9 Study of crystal defects in heavily boron-doped silicon **50**
9.1 Experimental . . . 50
9.2 OISF on heavily boron-doped wafers . . . 51
9.3 Dependence of OISF distribution on doping level and position in the crystal . . . 53
9.4 Simulation of the V-I boundary . . . 54
9.5 Estimation of the critical value v/G . . . 55
9.6 Comparison of V-I boundary simulations with OISF distribution . . . 57
9.7 Radial OISF distribution . . . 59
9.8 Relation of OISF to bulk crystal defects . . . 61
9.9 Origin of the radial OISF pattern . . . 62
9.10 Verification of the V-I boundary . . . 64
9.11 Origin of the axial changes in the OISF pattern . . . 65
9.12 OISF test with pre-annealing . . . 66
9.13 Origin of the axial variations in the size of grown-in oxide precipitates . . . 68
9.14 Summary on formation of the OISF pattern . . . 70
9.15 Enhanced precipitation of oxygen . . . 71
9.16 Influence of boron on oxygen precipitation . . . 72

10 Summary **74**

Author‘s contribution **75**

References **76**

Author’s publications **85**

Abreviations **88**

1. Motivation

ON Semiconductor is a worldwide producer of silicon-based discrete devices and integrated circuits for electronics. ON Semiconductor Czech Republic (CR) supplies the corporation with starting material — silicon wafers — manufactured from the silicon single crystals grown by the Czochralski method. Various defects are formed in the lattice of the growing crystal, which can influence the performance and reliability of devices made on the silicon wafers. This work is focused on study of the crystal defects in silicon and implementation and development of tools for their control.

As a particular example, it was found that Zener diodes manufactured on silicon wafers heavily doped with boron suffer from severe leakage current. Further analyses revealed the correlation of the leakage currents to the presence of crystal defects in the wafers. Due to scrapping of the afflicted wafers, the company encounters financial loss. Hence, there is a need for control of wafer quality from the defect point of view.

2. Silicon

Silicon (lat. Silicium) is the second most abundant element in the Earth crust (after oxygen), making over 25% of its weight. Silicon is found in the nature usually in the form of quartz and other silicate minerals.

History of elemental silicon (reviewed e.g. in [1,2] starts in the 18th century, when A. Lavoisier proposed that silica is actually an oxide of some important element (1787). First man-made silicon, amorphous and impure at that time, was prepared in 1811 by J.L. Guy-Lussac and L.J. Thénard through heating of potassium with silicon tetrafluoride. The discovery of element silicon is attributed to J.J. Berzelius, who in 1824 prepared amorphous silicon by essentially the same method as Gay-Lussac and Thénard, and purified the product by repetitive washing. The first crystalline silicon was made by H.E.St.C. Deville in 1854 from silicon tetrachloride and aluminum. The first "pure" silicon was prepared in 1907 by N. Potter through reaction of silica with carbon.

The early beginning of the semiconductor era dates back to 20's and 30's of the 20th century, when fundamental work on silicon band structure and transistor effects was carried out (see e.g. [1, 3] and references herein). During the World War II the semiconductor development was driven by British and American interest in radar. The real "semiconductor age" started in Bell Labs after the war. In 1947 J. Bardeen and W. Brattain [4] created the germanium bipolar point contact transistor. In 1949-1951 W. Shockley [5] invented the junction transistor (also germanium based) and drove further developments in this field. In 1956, Bardeen, Brattain and Shockley received the Nobel price for the invention of the transistor effect. The growing industrial interest in semiconductors drove development of techniques of crystal growth, purification and doping in 1940's and 50's. The work was primarily focused on germanium due to its availability in purer form and easier production allowed by lower melting point compared to silicon.

The early work performed with polycrystalline material showed that there is a need for material with higher minority carrier lifetime, which started the interest in single crystals. G.K. Teal and J.B. Little (Bell Labs) started work on manufacturing single crystalline germanium in 1948; in 1950 they employed the technique of crystal growth by pulling from the melt ([6–8]). They introduced use of the monocrystalline seed crystal of given crystallographic orientation, control of crystal shape through programmed temperature control of the melt, and rotation of the crystal and pull rate modulations for control of dopant distribution. Teal and Little laid grounds to the modern method of semiconductor crystal growth. In 1951, H.E. Buckley [9] (University of Manchester) "renamed" their method of pulling from the crucible by Jan Czochralski, who accidentally discovered the principle of crystallization by pulling from the melt in 1916 [10]. Writing down the notes on his experiments, he dipped his pen into the crucible with molten tin instead of his inkwell. Pulling the pen out the melt he found that a thin metal wire was hanging on the tip. Consequently he reproduced the experiment using a capillary instead of the pen and verified that the crystallized metal was a single crystal. Although the contribution of Teal and Little to development of the method of crystal growth from the crucible for industrial application is far more important then the early basics laid by Czochralski (they might even not know of the Czochralski work), the term Czochralski (CZ) growth has become generally used.

The development of germanium technology was accompanied by the search for other semiconductor materials. The hunt for higher carrier mobility started development of III-V compound materials in the early 1950's. At the same time research on silicon began, but rather on the background due to some doubt on semiconducting properties of silicon (which originated in the polycrystallinity and impurity of studied samples). Measured carrier mobility was about a factor of three lower than for germanium, thus only few researchers devoted themselves to silicon. Teal, e.g., experimented with silicon crystal growth in addition to his main task

on germanium in Bell Labs, and built up a silicon research team also in Texas Instruments (TI), where he moved in 1953. In 1954 TI commercially produced the first silicon transistor.

In 1955 Shockley became the director of Shockley Semiconductor Laboratory at Beckman Instruments. Several of his researchers left the company after he decided to not continue research of silicon-based semiconductors and started Fairchild Semiconductor with S. Fairchild in 1957 (R. Noyce and G.E. Moore later left Fairchild to set up Intel). Another company entering the semiconductor market in the beginning of 1950's was the Siemens Group [11]. During purification of silicon by reducing trichlorsilane with hydrogen, Siemens laboratory produced silicon rod with single-crystalline parts showing (to that time) superior purity. The potential of silicon for electronic applications was recognized and part of Siemens became entirely focused on silicon development. Purification efforts led to development of the "C-process" — deposition of silicon on inductively heated silicon rod from trichlorsilane in hydrogen atmosphere. This method, today known as the Siemens process, became the worldwide used procedure for manufacturing of polycrystalline silicon for electronics. Consequently, the zone-refining process for manufacturing of monocrystalline rods, which was concurrently invented also in Bell Labs (W.G. Pfann, 1952 [12]) was developed. The zone-refining technique opened the way to development of the Float Zone (FZ) technique in 1953 [13] which started up industrial mass production of silicon.

The breakthrough of silicon came in late 50's due to two innovations originated from Fairchild: (a) passivation of silicon surface by silicon dioxide and (b) the concept of device integration. Easy and stable passivation of silicon surface, which was unattainable for germanium, provided control over the surface states and opened the way to development of metal-oxide-semiconductor field effect transistor (MOSFET). The first MOSFETs were realized in 1960 in Bell Labs. Integration of electronic devices into a single chip solved the many problems associated with device contacting and significantly improved process yield and device reliability. First integrated circuit was created in TI in 1958, when J. Kilby connected about 25 transistors on 5-inch germanium wafer. It was again the unique masking properties of silicon oxide which allowed huge integration achieved on silicon during further development. Advanced MOS technologies and very large-scale integration (VLSI) allowed by Si-SiO_2 system opened the way to cost effective technologies and mass market with silicon integrated circuits. Silicon has finally won over germanium and become the crucial material for electronics during late 50's.

Concerning the crystal growth, the breakthrough happened in 1959 when W. Dash (General Electric) introduced the necking step for elimination of dislocations in the growing crystals [14]. Due to dislocation-free silicon, electrical performance of devices was substantially improved. The FZ technique adopted by Wacker in 1958 (licensed by Siemens) in Europe competed with the CZ pulling process used in USA (TI, Fairchild). The FZ silicon was used mainly for power devices; the CZ silicon dominated the manufacturing of integrated circuits. While FZ silicon seemed originally more attractive due to its extreme purity, CZ silicon has finally become more popular because its higher mechanical stability related to content of oxygen. In 1980's CZ silicon has become dominating material due to limited ability of FZ process to follow increase in crystal diameter above 125 mm. Step to 150 mm was much more difficult for FZ process and even today, 200 mm is the size limit for FZ crystals while 450 mm capability was demonstrated for CZ process. Another reason for CZ silicon was the discovery of gettering properties also related to oxygen content.

The interesting "tale" of semiconductor silicon outlined in this chapter is comprehensively described e.g. in [1, 15].

Finally, let us summarize the most important properties that predetermined silicon to become the material of choice for semiconductor industry of the 20th century:

- silicon is widely abundant in the nature,
- using clean precursors, silicon can be produced in a very clean form,

- silicon lattice provides wafers with high mechanical stability,
- silicon can be produced in single crystalline quality in large crystal diameters,
- silicon electrical properties can be well controlled, doping with both p- and n-type dopant is available over many decades of concentration,
- silicon oxide can be easily formed on the silicon surface allowing passivation, patterning and providing electrically insulating layer,
- silicon devices can operate in wider temperature range compared to germanium,
- silicon technology is already established as the mass production,
- silicon has low price compared to other semiconducting materials.

3. Production of silicon for electronics

3.1. Czochralski crystal growth

Today´s Czochralski (CZ) grown silicon single crystal are routinely produced in a mass scale in diameters up to 300 mm and the capability of diameter increase up to 450 mm has been demonstrated [16]. ON Semiconductor Czech Republic produces silicon crystals of 6” in diameter. The typical 6” CZ process will be introduced below; general aspects of CZ crystal growth can be found e.g. in [17–19].

A typical CZ puller is shown in Fig. 3.1. The puller consists of an upper and lower chamber formed by steel water-cooled shells. The lower chamber contains a graphite hot zone with active central part and thermally insulating outer parts. A silica crucible is placed in the heart of the hot zone which is supported by a graphite susceptor on the pedestal attached to the lower shaft. The seed holder is fastened onto the upper shaft (or affixed to a cable). The heater is a meandering-coil element heated by high electric current. Both chambers are piped to a vacuum system. The puller is typically purged with inert gas (usually argon). In the beginning of the process the quartz crucible is loaded with a charge of polysilicon chunks and the single crystalline seed is fitted into the seed holder. After closing the puller the chambers are evacuated and re-filled by inert gas to the desired process pressure (in the order of tens of mbar).

The process starts with melting the polysilicon charge by applying high power to the heater. Once the charge is molten, the melt flow is stabilized under steady conditions and the seed crystal is lowered towards the melt. The seed, a monocrystalline rod about 10 mm in diameter, predetermines the crystallographic orientation of the crystal. The seed and all parts of a crystal are schematically shown in Fig. 3.2.

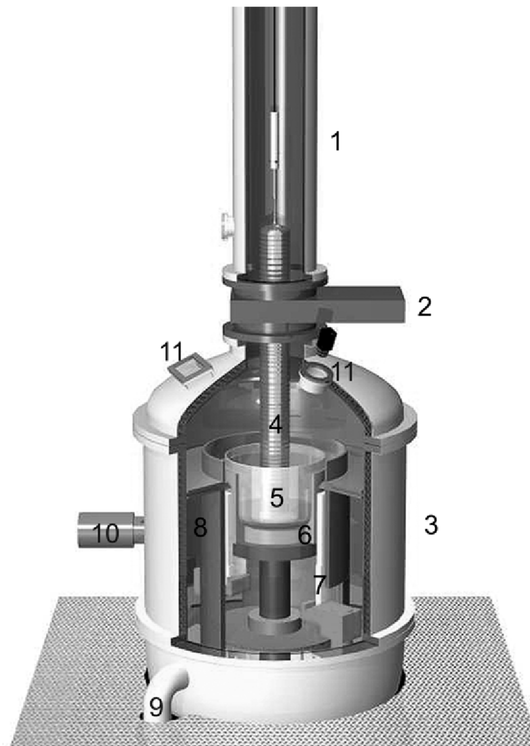

Figure 3.1: A typical configuration of a CZ silicon puller. (1) Upper chamber, (2) isolation valve, (3) lower chamber, (4) growing crystal, (5) silica crucible, (6) graphite susceptor, (7) heater, (8) insulation, (9) vacuum pipe, (10) heater pyrometer window, (11) operator and camera windows.

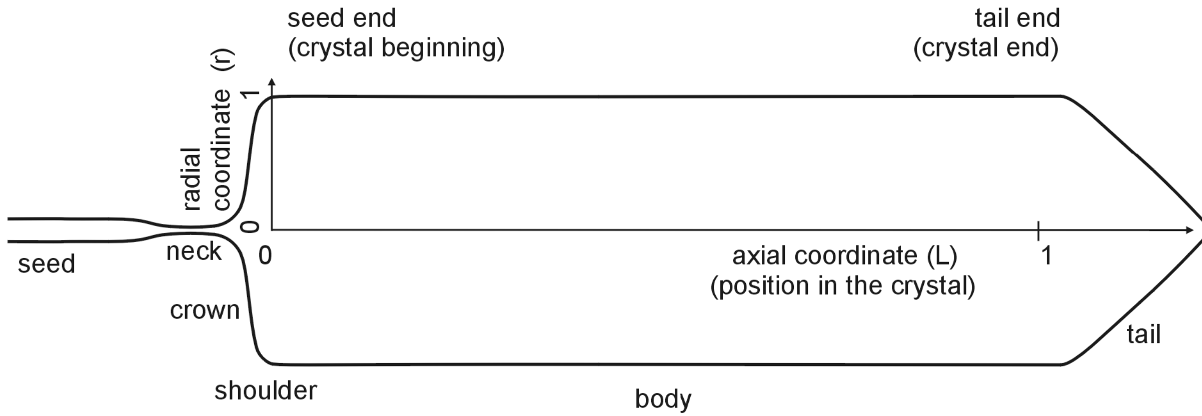

Figure 3.2: Schematic drawing of a silicon single crystal showing nomenclature and coordinate system used in this work.

After the seed is dipped into the melt, the system is adjusted to achieve a stable interface between the melt and the seed. Pulling the seed upwards crystallizes the melt at the solid-liquid interface and the crystal starts to grow.

Once the seed touches the melt surface, it is subjected to a huge thermal shock leading to generation of numerous dislocations. In order to achieve dislocation-free growth, necking is performed. To achieve this condition, the crystal is pulled with the rate of about 3–6 mm/minute and the crystal diameter is reduced to about 5–2 mm, which allows dislocations to partially freeze in the neck and partially move to the crystal surface. This effect is the consequence of inclination of the slip planes with respect to the seed axis for common crystal orientations. Dislocation-free growth is usually achieved after several centimeters of the neck growth. Then the pulling rate is significantly decreased and the diameter is slowly increased. The crystal grows into the form of a cone called the crown. As the diameter increases the pull rate is gradually increased (so called shouldering stage) until the crystal grows with the desired diameter and the proper growth rate. Then the cylindrical portion of the crystal, the crystal body, is grown.

The melt and the crystal are in intimate contact at the solid-liquid interface. The melt surface forms a meniscus to the crystal which reflects the light from the hot crucible to the chamber windows. This results in the appearance of a shiny ring on the melt surface around the crystal. As the meniscus height increases with crystal radius, changes in the meniscus height can be sensed and used for the control of crystal diameter during the growth of the crystal body. Another option for crystal diameter control is a measurement of the meniscus diameter with a CCD camera. The crystal diameter is controlled by the pulling rate. Simultaneously the pulling rate is adjusted by the heater power to be within the empirically-determined process window for dislocation-free growth, typically at or below 1 mm per minute. Solidification heat is conducted to the crystal surface and radiated to the chamber. For longer ingots the conductive heat flux is reduced and therefore the pulling rate has to be reduced. During the whole crystal growth process the crystal is rotated to homogenize the distribution of impurities and to suppress inhomogeneities in the temperature field. The crucible is rotated in the opposite sense to the crystal to stabilize the melt flow and control the oxygen concentration in the crystal.

The final stage of the crystal growth is the tail growth where the diameter is slowly decreased and a conical shape is achieved. As the diameter of the solidification interface is reduced dislocation formation is suppressed due to minimization of the thermal shock. Once the crystal has detached from the melt, the power to the puller is decreased and the crystal is cooled down while being lifted into the upper chamber. At the end of the process, the crystal is removed from the puller for further processing.

3.2. Float zone crystal growth

Float Zone (FZ) silicon is not the topic of this work, but it will be briefly introduced here since it is mentioned in the text several times.

The FZ technique [18, 20] is based on melting and re-crystallization of the polysilicon rod by an RF heating coil. Scheme of the process is shown in Fig. 3.3. First, the tip of the polycrystalline rod is molten by heat radiated from the graphite susceptor (heated by eddy currents induced by the coil). Once molten, eddy currents are induced directly in the silicon; the susceptor is removed and a single crystal seed of predetermined crystallographic orientation is dipped into the melt. The crystal is grown by lowering the seed, while crystal diameter is controlled by adjusting the seed and rod lowering rates. The first zone pass usually yields a polycrystalline ingot while single crystal is obtained after the second pass. The dislocation-free crystal growth is obtained (similarly to the CZ crystal growth) by using very high pull rate.

As the melt in FZ growth does not have any contact to solid material, silicon of very high purity is achievable. Hence, crystal resistivity of up to tens of kΩ is available while content of other impurities (oxygen among all) is negligible. These advantages make FZ silicon the material of choice for specific applications even through its higher price compared to CZ silicon.

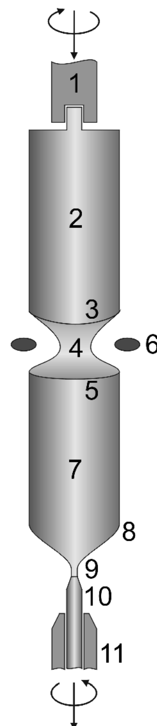

Figure 3.3: Schematic drawing of the Float Zone crystal growth.(1) Feed rod holder, (2) feed rod (polysilicon) , (3) melting interface, (4) molten zone, (5) freezing interface, (6) RF heating coil, (7) single crystal silicon, (8) crystal shoulder, (9) neck, (10) seed, (11) seed holder.

3.3. Manufacturing of silicon wafers

Manufacturing of silicon wafers involves a series of mechanical, physical and chemical processes, all optimized to provide superior properties of the final wafer. A simplified manufacturing flow of the silicon wafer is shown in Fig. 3.4.

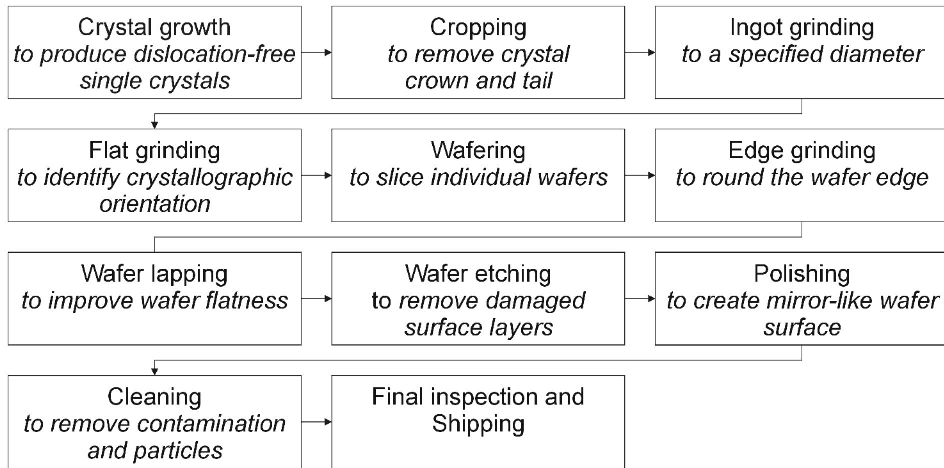

Figure 3.4: Schematic manufacturing flow of the polished silicon wafer production.

Wafer manufacturing follows the crystal growth process. First, the crystal crown and tail are cut off and the crystal body is divided into several pieces (Fig. 3.5a). Then the crystal quality (resistivity, oxygen and carbon content, dislocation-free state) is assessed on test wafers. Each piece of the crystal is then surface-ground to the desired diameter, the crystal is oriented, and the flat is ground onto the cylindrical ingot. The flat identifies the orientation of the silicon wafers with respect to specific crystallographic directions; usually it corresponds to the (1 1 0) plane. Silicon wafers are sliced from the crystal sections using wire-saws or the inner-diameter (ID) saws. After edge grinding the wafer is lapped, etched and polished. Finally, the polished silicon wafer may have an epitaxial layer deposited on the front surface by silicon epitaxy methods. Optionally the wafer backside can be coated with a polysilicon layer and/or a protective layer of silicon oxide. After final cleaning and inspection the silicon wafers are suitable for device or integrated circuit (IC) manufacturing. The box with polished silicon wafers is shown in Fig. 3.5b.

Figure 3.5: (a) Silicon single crystal cut into pieces. (b) Polished silicon wafers in the cassette.

4. Defects in silicon

Single crystal of CZ silicon, thought well defined material of high quality, still may contain various defects, which are formed either during the crystal growth or during processing of the silicon wafer. Basic overview of defects in silicon is given e.g. in [2] and [21]; extensive treatise of this topic can be found in [22–25] and others. Section 4.1 treats the topic from the historical point of view. Defects most relevant for the silicon technology will be introduced in section 4.3 and details are discussed in section 4.3 subsections. Section 4.2 provides a brief note on the crystal structure of silicon.

4.1. History

Early after the start-up of the mass production of dislocation-free silicon in 1960's it was realized that the highly pure FZ silicon wafers suffers from two diseases — enhanced formation of slip lines and degraded device yield compared to formerly used dislocated silicon. Later it was found that the yield issues are related to impurities and crystal defects [26]. Other problems, formerly shaded by a high density of dislocations, started to appear. Swirl-like distributed etch pits were observed after selective etching [27, 28]. In 1973, de Kock [29] distinguished two types of the swirl defects — the A- and B-swirl defects. De Kock concluded that the swirl defects are vacancy agglomerates. The right nature of the swirl defects was identified two years later by Foel and Kolbessen [30]. Using TEM microscopy, A-defects were identified as dislocation loops formed by agglomeration of silicon-self interstitials. B-defects were identified as coherent precipitates [31]. Later it was proposed [32] that the B-swirls also originate from self-interstitial agglomeration. Though the initial investigations were focused on FZ silicon, the swirl defects were observed in CZ silicon as well [33]. The nature of the swirl defects was still a matter of discussion, when another type of defect appeared [34–36]. These defects called C- and D-defects were supposed to be vacancy agglomerates [36, 37]. It was established that the B-defects are indeed interstitial agglomerates [38]. It might be interesting to note that the initial interest in point defects in silicon was motivated, besides the defect formation, especially by the studies of diffusion, which is necessary for fabrication of electronic devices.

The intensive research in the field revealed that formation of crystal defects depends on crystal growth conditions [36, 37, 39] — interstitial type defects are formed at lower growth rates and vacancy type defects at high growth rates. Several attempts were made to explain the occurrence of the various defects observed in silicon under miscellaneous experimental conditions. The models were different mainly in assumptions concerning the dominant type of point defects in silicon crystal, their concentration and interactions. Some models assumed that self-interstitials are the dominant point defects in silicon crystals at high temperatures [30–32], other presumed vacancies as the dominant point defect [37, 40], and simultaneous coexistence of both was also considered [41, 42]. Finally, a unifying, later generally accepted theory satisfactorily explaining the published observations was provided by Voronkov in 1982 [43].

According to Voronkov, both vacancies and interstitials are present in the crystal near the melting temperature. Point defects are transported by crystal growth and by diffusion to the region of lower temperature, where they recombine until only one of the species remains. Prior recombination, concentration of vacancies and interstitials varies spatially and there are regions where vacancies dominate over interstitials and vice versa. After the recombination stage, these regions contain only vacancies or interstitials, respectively. Voronkov showed that the dominant point defects after recombination are determined by the crystal growth conditions, namely by the V/G parameter, where V is the crystal growth rate and G the temperature gradient on the melt-crystal interface. If V/G is higher than a critical value ξ, vacancies dominate in the crystal; if V/G is lower than ξ, silicon self-interstitials dominate in the crystal. Further

cooling leads to supersaturation of point defects and results in their agglomeration into swirl-defects or D-defects, respectively. Formation of crystal defects in silicon is thus pre-determined by the crystal growth conditions. The theory of defect formation will be detailed in chapter 5.

The situation with defects in silicon crystals is even more complicated due to impurities inherently tied to silicon. In 1956, oxygen in concentrations higher than dopant concentration was found in CZ silicon [44] and silica crucible holding the silicon melt was identified as the source [45]. While most of oxygen evaporates from the melt free surface, some portion is incorporated into the crystal through the melt-crystal interface [46]. Based on the infrared absorption analyses it was established that oxygen occupies interstitial sites in the silicon lattice [44]. It was soon realized that oxygen in heated silicon forms electrically active centers, called thermal donors [47, 48]. It was established that oxygen is present in silicon in a supersaturated state below about 1200°C and tends to precipitate under favorable conditions. Patel and Chaudhuri first reported that severe oxygen precipitation can degrade mechanical strength of silicon [49]. These observations were verified later [50, 51] and it was found that also warpage of silicon wafer can be related to precipitation of oxygen [52, 53]. The nature of oxygen precipitates and associated extended defects — dislocations and stacking faults — was revealed consequently [54, 55].

Carbon was another extensively studied impurity in silicon [21, 56, 57] as substantial volume of device failures in 1970's was attributed to high carbon concentration. Carbon is incorporated into the crystal through the melt absorbing carbon monoxide, which is formed mainly by interactions of the puller atmosphere with graphite parts of the hot zone. It was found that carbon enhances oxygen precipitation, swirl formation and in high concentration precipitates into silicon carbide particles [32, 58–61]. With the course of time, the crystal growth process was improved and carbon contamination decreased typically below 0.1 ppma. The importance of carbon for defect formation so has become gradually suppressed.

Because of its detrimental effect on electrical and mechanical properties, oxygen was initially considered as a harmful impurity. The situation, however, started to turn over due to discovery of intrinsic gettering [62–64]. Rozgonyi and Tan and coworkers recognized the unique property of oxygen precipitates which can withdraw the impurities such as metal atoms from active area of the silicon wafer into the bulk, where metals cannot degrade device performance. It was also found that the as-grown CZ silicon shows higher resistance against thermal stress during device fabrication process compared to FZ silicon, which is on account of dislocation pinning by oxygen [49, 51, 65, 66]. It has to be reminded, however, that excessive precipitation may degrade wafer strength, as mentioned above. Anyway, due to beneficial effects of oxygen through intrinsic gettering and its influence on mechanical properties, CZ silicon has dominated the IC industry over FZ silicon since the 1980's.

The effectiveness of internal gettering and effect of oxygen on mechanical properties depend on annealing conditions, concentration of oxygen and interactions with intrinsic point defects. Hence, a lot of effort was put in investigation of defect formation in CZ silicon during following decades. In mid 1980's, interesting ring-like distribution of stacking faults was observed after oxidation of silicon wafer [67]. The feature has been called Oxidation Stacking Fault ring (R-OSF) or Oxidation-Induced Stacking Fault ring (OISF ring). Later it was found that interior of the OISF ring contains defects deteriorating the gate oxide integrity (GOI) of MOS devices, while the outer region of the OISF ring shows excellent GOI performance [68]. As the origin of the defects was traced back to the crystal growth, they became called Crystal Originated Particles (COPs) [69–71]. The defects could be delineated by chemical etching as Flow Pattern Defects (FPD) and they were associated with the known vacancy agglomerates, D-defects [72]. Finally, the D-defects were found to be octahedral voids formed by agglomeration of vacancies [73, 74]. Due to its easy observation, OISF-ring became widely utilized tool for studying and controlling defects in silicon. Besides, it was attractive in itself due to its interesting appearance and relation to other defects (see section 5.5 for details).

In late 1990's, the picture of microdefects in silicon was rather well established (see chapter 5 for details): CZ silicon crystals might contain a vacancy-interstitial boundary separating a vacancy-type core and interstitial-type rim; the distribution of the point defects is determined by the Voronkov´s V/G parameter. The vacancy-type region is characteristic by formation of voids, COP or FPD defects and by appearance of the OISF ring on its outer rim. The interstitial-rich region contains A- and B-defects, which are agglomerates of silicon self-interstitial. Oxygen precipitation is enhanced in the vacancy-type region and suppressed in the interstitial-type region. This behavior originates from the precipitate growth which is accompanied by emission of silicon self-interstitials.

Engineering of defects in silicon, which appeared several decades ago, has been continually developing until the present day. Every step in increasing wafer size and decreasing dimensions of electronic devices creates new needs for optimization of internal gettering and elimination of the harmful defects. Intensive investigation was applied on detailed models of mutual interactions of point defects, oxygen, dopant species and impurities such as nitrogen from the crystal growth, through the wafer thermal treatment up to the device manufacturing process. Advances in computing techniques promoted significant employment of numerical modeling of the crystal growth process and defect formation, which became inseparable part of defect engineering science.

The problem of defects in silicon covers such a large area that is not within the compass of the author to provide complete overview on the topic. Basic aspects and historical context were given in this chapter, more information can be found in references mentioned in the introduction to chapter 4, and details on topics relevant for the thesis will be provided in following chapters.

4.2. Silicon crystal structure

Silicon crystallizes in the diamond cubic lattice [2], which structure can be constructed as two interpenetrating face-centered cubic (fcc) lattices displaced along the unit cell body diagonal by the quarter of its length. The lattice is shown in Fig. 4.1. The lattice constant of pure silicon is representing the length of the side of the fcc cube and has the value of 0.5431 nm at room temperature. Each silicon atom from one fcc lattice is covalently bound to its four nearest neighbors which belong to the other fcc lattice. In principle silicon wafer can be manufactured with the silicon lattice being oriented in any arrangement with respect to wafer surface. The common crystallographic orientations of wafer surface, described by Miller indexes, are (100), (111) and (110). The crystal planes belonging to the families of these low-index crystal planes, i.e. $\{100\}$, $\{111\}$ and $\{110\}$ family, are the most important planes in the silicon lattice with the largest differences in various properties among these planes.

The closely spaced planes of the $\{100\}$ family are the $\{400\}$ planes with the interplanar distance of 0.1358 nm. The $\{220\}$ planes with spacing of 0.1920 nm are the closely spaced planes of the $\{110\}$ system. While spacing of all the $\{400\}$ and $\{220\}$ planes is equidistant, the situation is more complicated in case of the $\{111\}$ system. The $\{111\}$ planes of the fcc lattice are stacked in an ...ABCABC... manner, where none of the atoms in each layer is aligned with atoms in other layers when viewed perpendicularly to the stack. The $\{400\}$ planes follow the ...ABCDABCD... scheme and the $\{220\}$ planes follow the ...ABAB... scheme. Since the diamond lattice consists of two fcc lattices displaced along the direction perpendicular to $\{111\}$ system, stacking along $\langle 111 \rangle$ follows the ...AaBbCcAaBbCc... scheme. Here atoms in planes of the same letter overlap each other when viewed in $\langle 111 \rangle$ direction and capitalization distinguishes planes belonging to the two interpenetrating fcc lattices. The distance between adjacent planes of the same set (A–B, B–C and C–A) is 0.3135 nm; the distance between the closely spaced planes of the system a–B, b–C and c–A is 0.0784 nm and 0.2352 nm for the system A–a, B–b, C–c, which is the length of covalent bond silicon–silicon. The closely spaced planes are bound strongly and

often appear as one double plane. Different spacing of the crystal planes corresponds to different surface atom densities of 6.78×10^{14} cm^{-2} for {100} planes, 7.83×10^{14} cm^{-2} for {111} planes and 9.59×10^{14} cm^{-2} for {110} planes. The {111} plane shows the lowest surface energy and crystallizing silicon therefore tends to be bound by the {111} planes. Also the growth rate of the epitaxial layer is the lowest for the {111} oriented surface.

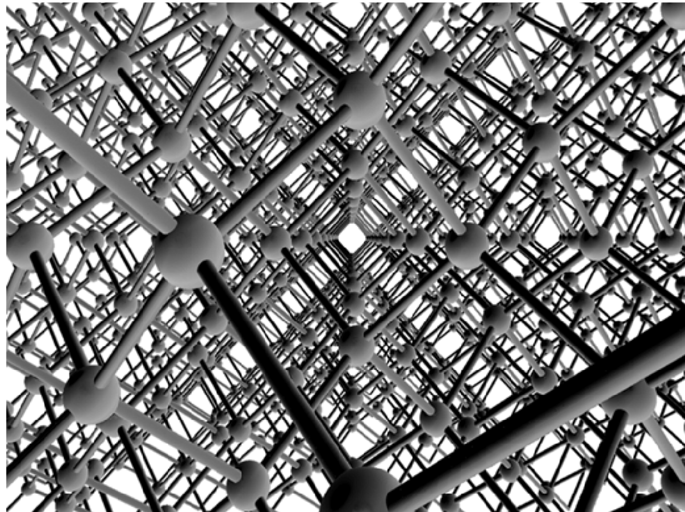

Figure 4.1: Silicon lattice viewed paralel to the $\langle 100 \rangle$ direction.

4.3. Classification and overview

Crystal defects are usually classified according to their shape and dimension. Silicon crystals and wafers may contain variety of defects [2]:

(a) point defects (silicon self-interstitials, vacancies, interstitial impurities such as oxygen, substitutional impurities such as dopant atoms and carbon),
(b) line defects (edge and screw dislocations, dislocation loops),
(c) planar defects (stacking faults),
(d) bulk defects (agglomerates of point defects).

Some of the crystal defects are schematically shown in Fig. 4.2.

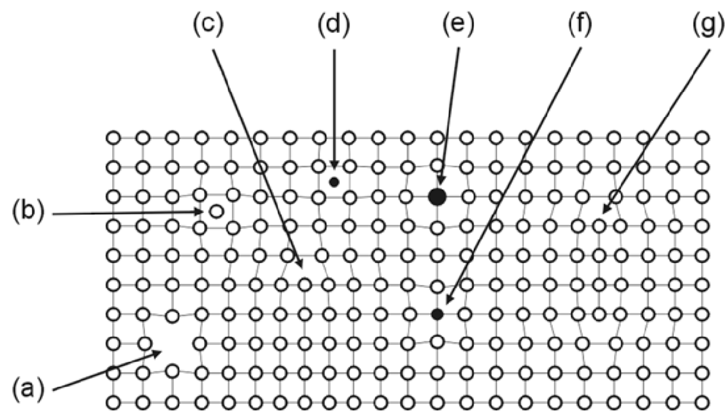

Figure 4.2: Schematic 2D representation of crystal defects in silicon. (a) Vacancy, (b) self-interstitial atom, (c) edge dislocation, (d) interstitial impurity atom, (e) substitutional impurity atom of larger atomic radius, (f) substitutional impurity atom of smaller atomic radius, (g) extrinsic stacking fault.

4.3.1. Point defects

Intrinsic point defects

Vacancies (missing atoms) and silicon self-interstitials (extra atoms) are intrinsic point defects inherent to the material whose occurrence in the lattice arises from the thermodynamic considerations [75]. Intrinsic point defects are assumed to be incorporated into the growing crystal at the melt crystal interface in their equilibrium concentrations. Additional mechanisms of formation/annihilation of intrinsic point defects once the material has crystallized are:

(a) Shottky mechanism, when a silicon atom ”jumps” into the interstitial position and diffuses to the surface where it becomes a surface atom, leaving a vacancy in its original site. The Shottky mechanism forms vacancies in the bulk. In case of the CZ silicon, this mechanism takes place only near the crystal periphery due to relatively low diffusivity of silicon self-interstitials.
(b) Frenkel mechanism, when silicon self-interstitial and vacancy are formed by ”jumping” of the lattice atom into the interstitial site. The inverse process is recombination, when silicon self-interstitial occupies a vacancy site forming a regular lattice atom in final.
(c) Interaction with bulk defects, which can serve as sources or sinks for the intrinsic point defects.
(d) Thermal wafer processing. Wafer oxidation introduces self-interstitials below the surface while annealing in nitrogen leads to formation of vacancies.

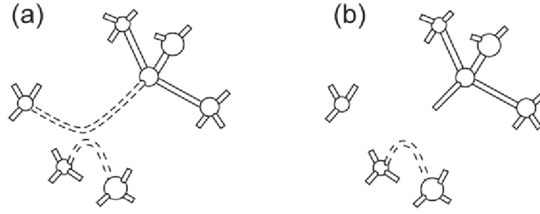

Figure 4.3: Model of (a) a neutral vacancy and (b) a singly positively charged vacancy [22].

Silicon atom removed from its lattice site leaves behind four broken covalent bonds which can be arranged in several configurations [22] (examples in Fig. 4.3). When two and two of the bonds form molecular orbitals, a neutral vacancy is formed. The orbitals are strained and can be relatively easily broken. Interaction with charge carriers results in formation of singly and doubly positively or negatively charged vacancies.

Silicon self-interstitial is considered as an additional, more or less free, atom occupying tetrahedral or hexagonal interstitial sites [22] (Fig. 4.4a, b). More recent works favor a dumbbell configuration (called also split interstitial), when two atoms share a lattice site (Fig. 4.4c).

Several works suggest even more complex structure of intrinsic point defects, such as extended nature with the disorder spread over several atoms both for vacancies and interstitials [22], or semi-vacancy pair with one silicon atom occupying two vacant sites. Small clusters of vacancies and interstitials can be still considered as point defects. Divacancies (V_2) were identified in silicon and the existence of tri- up to hexa-vacancies was concluded from electron paramagnetic resonance (EPR) and deep level transient spectroscopy(DLTS) spectra and theoretical calculations. Similarly, di-interstitials up to octo-interstitials were described. For more details, the reader is referred to [22] and references within. In conclusion, the atomic arrangement of vacancies and interstitials in silicon still remains somewhat uncertain. Yet, their effective thermodynamical properties such as concentration and diffusivity are experimentally determined and widely employed.

Introduction of intrinsic point defects into a perfect crystal lattice increases both enthalpy H and entropy S of the system. The thermodynamic potential of the crystal - the Gibbs energy G - is given by:

$$G = H - TS. \tag{4.1}$$

The entropic and enthalpic terms act against each other and minimum in G can be found. This minimum corresponds to the equilibrium state of the system. The increment of the Gibbs energy can be expressed in terms of formation enthalpy H^f and formation entropy S^f of individual point

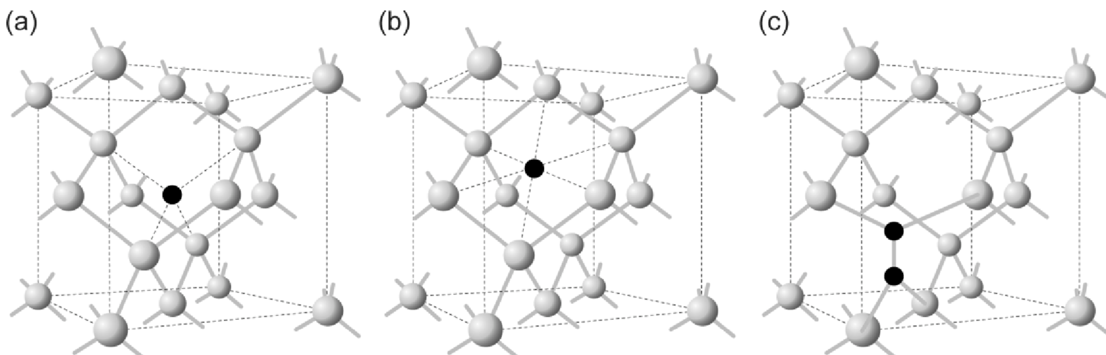

Figure 4.4: Model of a silicon self-interstitial in (a) a tetrahedral position, (b) a hexagonal position and (c) a dumbbell configuration [22].

defect multiplied by the number of point defects. Minimization of G with respect to number of defects yields the equilibrium defect concentration C^{eq} [22],

$$C^{eq} = C_s \exp\left(\frac{S^f}{k}\right) \exp\left(-\frac{H^f}{kT}\right), \tag{4.2}$$

where C_s is the concentration of lattice sites in silicon. The values are usually reported in the form of Arrhenius law

$$C^{eq}_{I,V} = K_{I,V} \exp\left(-\frac{H^f_{I,V}}{kT}\right), \tag{4.3}$$

where I and V denote silicon self-interstitials and vacancies, respectively, and H^f is the enthalpy of formation of a defect. The pre-exponential factor accounts for all terms explicitly independent of temperature. Unfortunately, the published values vary significantly for both the K and H^f values [22]. Similar variations are observed for the reported values of vacancy and interstitial diffusivities [22].

Extrinsic point defects

Dopant atoms are primary extrinsic point defects in CZ silicon. Dopants — boron, arsenic, antimony and phosphorus — introduced deliberately into silicon during the crystal growth occupy substitutional sites in the lattice. Their concentration varies typically in the range of 10^{10}–10^{15} cm^{-3}. The effect of dopant atoms on silicon (besides the primary electronic effect) originates from different atomic radius (Tab. 4.1) , interactions with intrinsic point defects, formation of clusters and effect on diffusion of impurities [22].

Element	Atomic radius [Å]	Ratio to silicon at. radius
Sb	1.35	1.16
As	1.18	1.01
Si	1.17	1.00
P	1.10	0.94
B	0.88	0.75

Table 4.1: Tetrahedral covalent radius of common doping elements in silicon — absolute values and ratios to value of silicon [76].

After dopants, *oxygen* is perhaps the most important impurity in silicon [2,21]. Oxygen appears in CZ silicon during the crystal growth. Silica crucible dissolves into the silicon melt and oxygen is transported by diffusion and melt flow to the melt-crystal interface, where it is incorporated into the growing crystal. Most of the oxygen evaporates from the melt free surface and only about 1–2% reaches the crystal. Oxygen concentration in the CZ silicon crystals is typically in the order of 10^{17} cm^{-3}, oxygen solubility in silicon at the melting temperature is about 2×10^{18} cm^{-3} [76]. In this work, oxygen concentration will be given in accordance with the ASTM´79 standard [77] (commonly known as "old ASTM"). Oxygen atoms occupy an interstitial position in the silicon lattice, where it is covalently bound to two nearest silicon atoms [22]. Model of interstitial oxygen in silicon is shown in Fig. 4.5.

Interstitial oxygen is known to form electrically active chains known as thermal donors. The family of oxygen thermal donors includes sixteen different complexes [78]. Oxygen also forms complexes with intrinsic point defects [22]. The existence of numerous oxygen-vacancy complexes $\mathrm{V_mO_n}$ (m,n = 1–6) were reported. Similarly $\mathrm{I_mO_n}$ complexes were identified with m,n = 1–2. These complexes may play role during formation of bulk defects and promote oxygen diffusion.

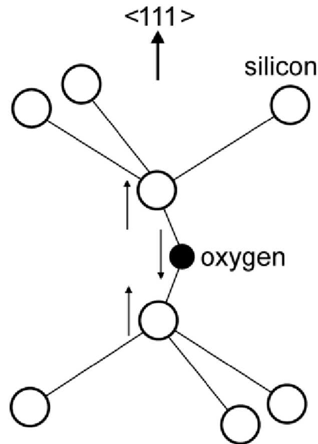

Figure 4.5: Atomic configuration of interstitial oxygen atom in the silicon lattice [79]. The arrows demonstrate the antisymmetric vibrational mode utilized for FTIR measurement of oxygen concentration.

Extremely undesirable point defects are *atoms of metals* [2,80]. Deep energy levels near the middle of the silicon band gap arising from metallic centers and pose serious issues for device performance and process yield. The transition metals such as copper, nickel and iron are the most abundant contaminants. At high temperatures, metal atoms are usually dissolved in the lattice occupying both interstitial and substitutional sites. With lowering the temperature, metals can form complexes with dopant atoms; eventually can precipitate into bulk defects. The state of the metals in the lattice depends on their solubility in silicon and imposed thermal cycles. Solubility of selected metals in solid silicon is plotted in Fig. 4.6. The level of metallic contamination in semiconductor silicon for today's processes is typically below 10^{11} cm^{-3}. The steep

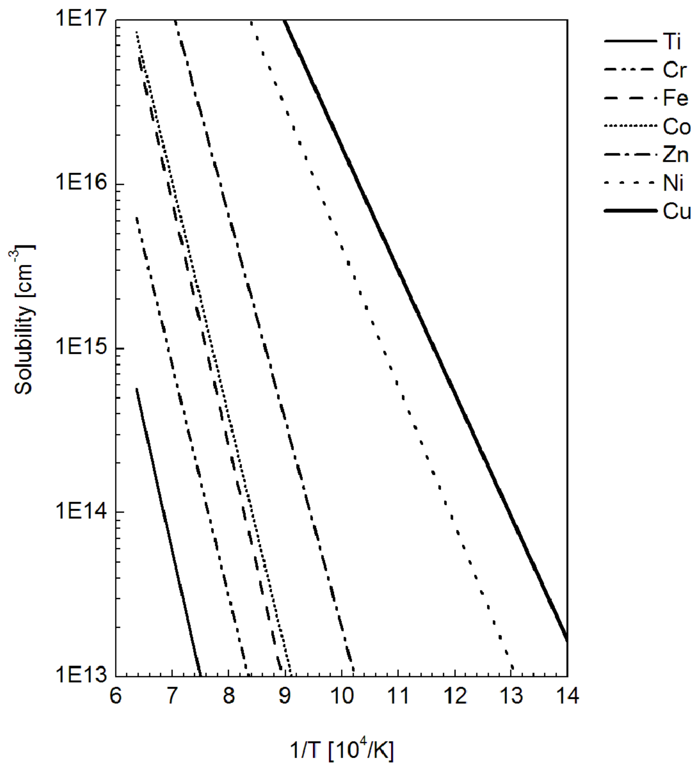

Figure 4.6: Solubility of selected metals in silicon (data were taken from [80]).

decrease in solubility with decreasing temperature is commonly used by relaxation-type gettering techniques for removing the metals from active device regions.

Unavoidable impurity in CZ silicon is *carbon* [2, 21, 22], introduced into the crystal growth system mainly from the graphite elements of the hot zone. Typical concentration of carbon in semiconductor silicon is below 0.1 ppma (5×10^{15} cm^{-3}). Carbon occupies predominately substitutional sites of silicon lattice. Due to four-valence electrons, substitutional carbon is electrically inactive. Substitutional carbon forms complexes with oxygen. Interaction with silicon self-interstitial may lead to displacement of carbon into interstitial position. Interstitial carbon readily forms complexes with intrinsic point defects, substitutional carbon or dopants. These complexes may be electrically active. Carbon was reported to promote oxygen precipitation. However, due to low concentration of carbon in today's silicon, the role of carbon in microdefect formation is of minor importance.

Nitrogen [21, 22] is impurity intentionally incorporated into silicon for special applications. Nitrogen is introduced into silicon melt from nitrogen ambient or from solid silicon nitride put into or contained in the silica crucible. Nitrogen incorporated into the growing crystal adopts predominantly interstitial positions, only about 5% occupies electrically active substitutional sites. Nitrogen forms numerous complexes with itself, intrinsic point defects, oxygen and dopants. Nitrogen-oxygen complexes act as shallow thermal donors and nuclei for oxygen precipitation. Vacancies conserved in nitrogen-vacancy species provide free space for growth of oxygen precipitates and prevent vacancies from agglomeration into voids. Nitrogen has also been used for improvement of mechanical properties (especially of FZ silicon) due to its dislocation pinning effect.

4.3.2. Line defects

Today's CZ silicon crystals are grown in a dislocation-free mode (see Fig. 4.7), hence are typical by absence of dislocations [2, 81] (A-defects are not taken into account). Dislocations appear in silicon mainly due to stress generated by high temperature operations during the manufacturing of the wafer and devices on it. Edge and screw dislocations and dislocation loops have been observed in silicon mainly accompanying oxygen precipitates, self-interstitial agglomerates and slips.

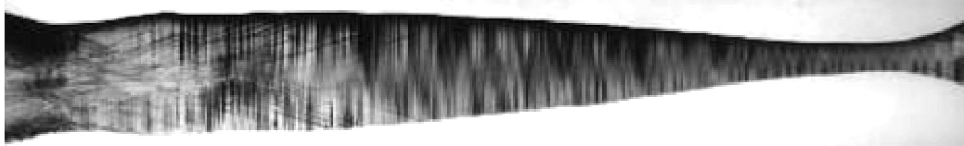

Figure 4.7: X-ray topograph of the Dash neck formed during CZ crystal growth. Dislocations propagating from the left hand side of the figure were generated by thermal shock during seed melting. Dislocations are effectively eliminated due to inclination of the dislocation propagation planes with respect to the growth axis.

4.3.3. Planar defects

Two types of stacking faults (SFs) are generally distinguished, namely intrinsic and extrinsic faults. Intrinsic SF is formed by several missing atomic planes while the extrinsic SF is formed by excess atomic planes. SFs in silicon are always of the extrinsic nature [2] formed by discs of double planes inserted into the regular AaBbCc order of silicon {111} atomic planes. As the layers in the SF have to be added in pairs, one can abandon the double index notation and describe the packing of the sequence with ...ABCABC.... In the SF region the order of planes is changed, such as ...ABCACABC.... SFs are considered to be low-energy faults because they involve no change in the covalent bonds of the four nearest neighbors in the lattice [82]. On the other hand, faults which disturb the nearest-neighbor covalent bonds are called high-energy faults (these are, for example, dislocations). The SF is bound by a Frank-type partial dislocation. A schematic drawing of such a SF is shown in 4.2. Other types of planar defects such as twin planes or grain boundaries are not present in properly-grown single crystal silicon.

SFs originate from the condensation of silicon self-interstitials [83], preferentially on suitable nucleation sites such as oxide precipitates, metal precipitates or mechanically damaged locations in the lattice. Surface and bulk SFs are distinguished according to the location of their nucleation site. Stacking faults can be delineated by selective etching of the sample surface and studied

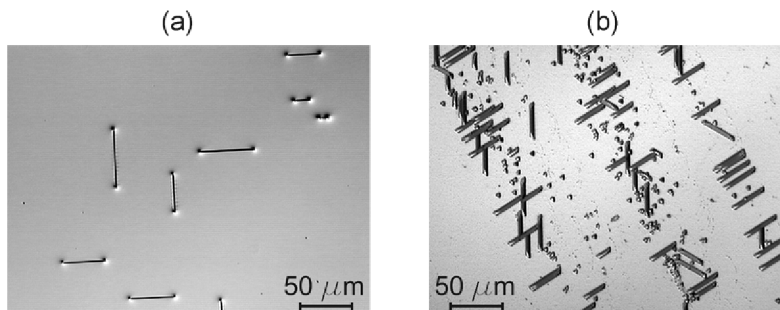

Figure 4.8: (a) Bulk stacking faults on a (100) silicon surface. The varying SF length originates from the various depths of nucleation sites below the etched surface. (b) Surface stacking faults and dislocations on a (111) silicon surface. Predominantly equal SFs length confirms nucleation on the surface.

by optical microscopy or other inspection methods. The crystallographic origin determines the appearance of the SFs on the surface of silicon wafers of different orientations (see Fig. 4.8).

Bulk SFs in the silicon wafer may grow in the regions of strong oxygen precipitation [21], which is accompanied by a massive ejection of silicon self-interstitials. Growth of the surface SFs can be also enhanced by an increased population of self-interstitials created by surface oxidation. SFs observed on the surface of polished silicon wafer after oxidation are referred to as "oxidation induced stacking faults" (OISFs).

4.3.4. Bulk defects

Vacancy-type defects. Supersaturated free vacancies present in silicon crystal at high temperatures agglomerate into voids [73, 74, 84]. Voids (Fig. 4.9b) take the octahedral form bound by {111} planes. The octahedral shape may be incomplete, truncated by {100} planes. Under favorable conditions, double- or triple-voids appear [85]. The inner void surface is covered by an oxide layer of typically 2–4 nm. The typical void size is around 100 nm and density is about 10^6 cm^{-3}.

Void intersected by the wafer surface creates a pit referred to as the Crystal Originated Particle (COP) [69–71] (Fig. 4.9a). Fig 4.9a-b show this relation between voids and COPs. The typical dimension of a COP does not allow direct observation on the polished wafer surface by common industrial equipment; AFM is often used for the analyses. It was found that COPs can be observed by commercial laser particle counters after repetitive SC1 cleaning [70]. The SC1 cleaning slightly etches the COP and enlarges it above the detection limit of the used instruments, which can be up to 200 nm. The size of COP defects after SC1 treatment is typically 100–300 nm and the surface density (corresponding to the bulk density mentioned above) is in the order of 10^0–10^1 cm^{-2}. Being the vacancy agglomerates, COPs are observed only in the vacancy-type silicon. Hence, on a wafer containing the vacancy-interstitial boundary (see chapter 5.2), COPs are distributed in a circle corresponding to the vacancy-rich core (Fig. 4.9c). COPs on the wafer surface can be delineated also by other methods such as Secco etching, when they appear as the wedge shaped Flow Pattern Defects (FPDs) [72]. Voids detected by Infra Red Light Scattering Tomography are denoted as LSTD [86].

Interstitial-type defects. Supersaturated silicon self-interstitials agglomerate into so called A- and B- defects (swirls). The B-defects are considered to be coherent globular clusters [31, 32], the A-defects are large dislocation loops [30] possibly formed by the collapse of the B-defects. The large dislocation loops appear in size ranging from units to few tens of micrometers and

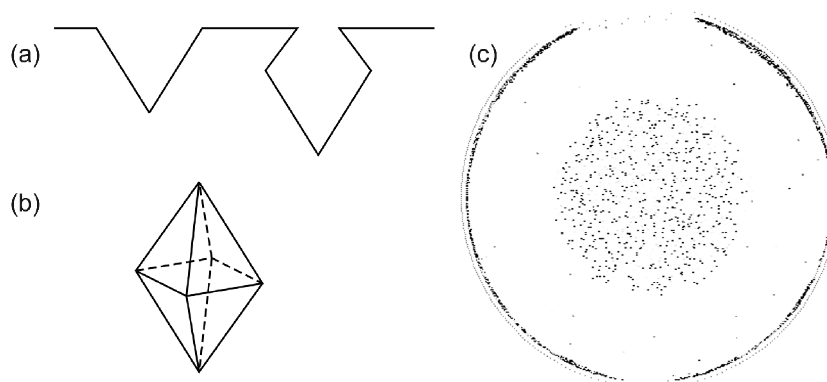

Figure 4.9: Schematic representation of (a) COP defects on the wafer surface, and (b) a void defect in the wafer bulk. (c) COP distribution observed by laser-type particle counter after dedicated SC1 treatment of the wafer with a vacancy-type core. The "particles" detected around the wafer edge are a measurement artefact.

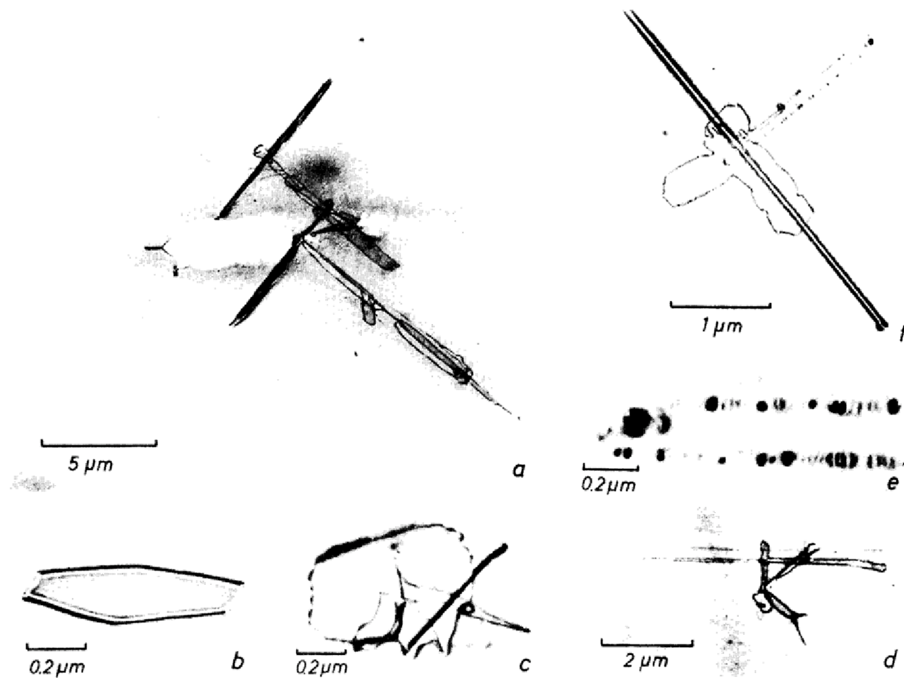

Figure 4.10: Examples of A-defects observed by TEM in silicon. Adopted from [32].

density typically around 10^8 cm^{-3}. Examples of the A-defects are shown in Fig. 4.10; the B-defects were found too small for direct TEM observation.

Oxide precipitates. Due to solubility rapidly decreasing with temperature and rather high oxygen concentration in CZ silicon crystals, oxygen in silicon is usually in a supersaturated state at common process temperatures (about 600–1200 °C). Resulting precipitation of oxygen interstitials [87] leads to formation of oxide particles referred to as oxide precipitates or oxygen precipitates (both names may be used in this work). Oxide precipitates are considered to be formed by amorphous SiO_x, where x ranges from 1 to 2; the definite conclusion is still missing [88]. Oxide precipitates of various morphologies were observed [89–92]; from rod-like, square platelet, truncated octahedral, polyhedral to sphere shape (examples are shown in Fig. 4.11). Morphology of oxide precipitates depends on formation conditions — mainly temperature and supersaturation — and in principle is determined by the stress energies associated with the precipitate growth [88, 93].

As the silicon atom in the oxide phase occupies higher volume than in the silicon matrix (roughly 2 times for the case of SiO_2), formation of an oxide particle is accompanied by local volume expansion. The resulting stress is relieved by emission of silicon interstitials into the surrounding lattice. At low temperatures, the emission of silicon interstitial is difficult (due

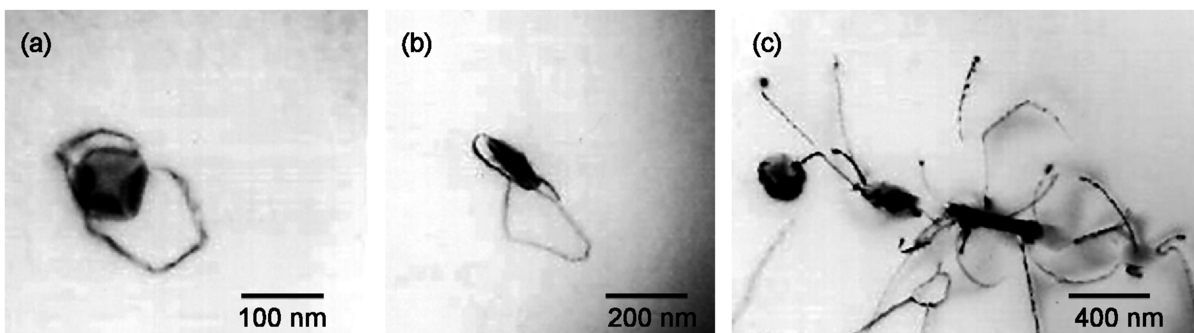

Figure 4.11: Example of (a) polyhedral and (b) platelet oxygen precipitates with associated dislocations. (c) Complex of oxide precipitates and dislocations. Photographs adopted from [95].

to the low equilibrium concentration of interstitials) and the precipitate takes the form exhibiting the lowest possible stress. The strain energy is lowest for the plate-like shape; hence platelet precipitates tend to dominate at lower temperatures. At higher temperatures the emission of self-interstitials is easier, the volume-related stress loses importance and the interface energy becomes the determining factor. Hence, mainly polyhedral or even spherical precipitates are formed at high temperatures. The typical formation temperature is about 400–650 °C for rod-like precipitates, 650–950 °C for the platelets and above 950 °C for octahedral and polyhedral precipitates [93, 94], the values vary a bit among various authors.

The precipitate morphology depends also on oxygen concentration. Low oxygen supersaturation can result in formation of small octahedral precipitates independently of the formation temperature, because the growth rate of the precipitate (and accompanied emission of interstitials) is so low that the stress relaxation proceeds easily and the influence of minimal surface energy becomes dominant [88]. Annealing time also plays a role, since it influences the stresses through the size of the grown precipitates [94].

Growth of oxide precipitates is usually accompanied by formation of extended defects such as stacking faults and punched-out dislocation loops [54, 89, 90, 95] (see Fig. 4.11 for example).

4.4. Impact of crystal defects on device yield

While the vacancy- and interstitial-type crystal defects have detrimental effect on yield and performance of electrical devices, oxygen precipitates and associated extended defects can act both in negative and positive sense.

COP defects were shown to degrade Gate Oxide Integrity (GOI) [72–74, 96, 97] causing, e.g., extrinsic dielectric breakdowns of MOS capacitors or failures of the DRAM modules. Voids below the surface can result in leakage currents of power devices. The gate oxide grown across a COP may be locally thinned or stressed on the COP edges where even the electric field is concentrated; both these effects then lead to dielectric breakdowns. Procedures for improving the quality of the void-containing silicon are based on annealing of polished wafer in argon or hydrogen ambient [98, 99], introducing nitrogen into the growing crystal [72, 100, 101], or surface overgrow by a thin epitaxial layer [102]. The additional treatments of the polished wafer, however, increase the wafer cost.

The interstitial-type dislocation loops in active regions of the devices cause degradation of carrier lifetime, p-n junction characteristics or diffusion profiles [103]. Due to their large size, they are especially harmful for today′s processes characteristic by a high degree of device integration. The dislocations serve as diffusion and conductive paths. Especially when decorated by metals, dislocations are sources of shorts and huge reverse currents.

Oxygen thermal donors [78] induce resistivity shift in very lightly doped silicon, which affects numerous resistivity-dependent device parameters. The thermal donors are formed by rather weak binding energies and can be easily dissolved at elevated temperatures (typically above 600 °C). As oxygen thermal donors are formed around 450 °C, cooling rates during the device manufacturing process should be optimized in order to control resistivity of the sensitive material. The oxide precipitates are, on the other hand, quite stable defects whose existence at a given temperature is determined by the critical radius. Oxide precipitates in the active region of the device result in increased reverse leakage currents of p-n junctions, reduced refresh time in DRAM memories and breakdown voltage in bipolar devices, degraded minority carrier generation/recombination lifetime, and other serious failures (see e.g. [93, 104–106] and references within). The root-causes of the failures are the precipitates themselves as well as the associated extended defects. On the other hand, oxide precipitates have also positive effect through mechanical strengthening [49, 51, 65, 66] and internal gettering [62–64]. However, oxygen precipitation has to be controlled in an optimal range, and a defect-free near surface region (so called denuded zone) should be guarantied.

The effect of crystal defects on manufacturing process and properties of silicon wafers and electronic devices is multifarious and the impact is often radical. Hence, engineering of crystal defects is inseparable, and, due to continuous evolution of silicon devices, also never-ending part of the technology of CZ silicon growth and wafer manufacturing.

5. Formation of grown-in defects in CZ silicon

In order to control formation of the crystal defects in silicon wafers one has to understand the mechanisms of their formation from the very early stages of the crystal growth. The basic mechanisms of defect formation during the silicon crystal growth are described by the Voronkov theory [43, 107], which will be briefly introduced in following sections.

5.1. Point defects — pathway to crystal defects

Voronkov´s theory describes the formation of the crystal defects consisting of several stages [43]:

1. incorporation of silicon self-interstitials and vacancies into the crystal,
2. transport, diffusion and recombination of the point defects,
3. nucleation and growth of defect clusters.

It is assumed that both silicon self-interstitials and vacancies are incorporated into the growing crystal at the melt–crystal interface. High diffusivity near the melting temperature and proximity of the crystal surface acting as an effective source/sink allows the intrinsic point defects to exist in their equilibrium concentrations.

The concentrations are changing during cooling of the crystal induced by its growth. It is assumed that the recombination rate of the point defects is high enough to maintain the product $C_I C_V$ near its equilibrium value $C_I^{eq} C_V^{eq}$ (mass action law). As the equilibrium concentrations of the point defects decrease very fast with the temperature, the $C_I^{eq} C_V^{eq}$ product quickly drops, one of the point defects vanishes, and only the second specie survives the recombination. The type of the surviving defect is determined by the concentration of vacancies and interstitials prior recombination and this in turn is determined by the flux of the defects towards the region of effective recombination.

Vacancies and interstitials in the crystal diffuse by Fickian diffusion and thermodiffusion and are drifted by the growing crystal. The axial flux of point defect into the crystal (in the z-direction) is given by [107]:

$$j_z = vC - D\frac{\mathrm{d}C}{\mathrm{d}z} + \alpha GC, \tag{5.1}$$

where the meaning of individual symbols is following:

j_z... axial flux of point defect into the crystal,
v... crystal pull rate,
C... concentration of point defects,
D... coefficient of diffusion,
z... distance from the melt-crystal interface,
α... coefficient of thermodiffusion (thermal drift),
G... temperature gradient.

As the thermodiffusion can be neglected in the first approximation, there are essentially two flux components for each point defect — the drift component vC and the diffusion component $-D\mathrm{grad}C$. Voronkov assumed that the equilibrium concentrations of interstitials $C_I^{eq}(T_m)$ and vacancies $C_V^{eq}(T_m)$ at the melting temperature T_m are comparable, but $C_V^{eq}(T_m)$ is somewhat higher than $C_I^{eq}(T_m)$. Therefore, the drift flux of vacancies is higher than that of interstitials. Thus, the drift (convection) is responsible for supplying vacancies into the crystal and the flux of vacancies into the crystal is proportional to the growth rate v.

The diffusion flux is proportional to the concentration gradient. The concentration gradient arises from the defect recombination occurring few centimeters above the melt-crystal interface in the region at about 1300 °C. Hence, the temperature profile above the melt-crystal interface determines the concentration gradient, which drives the diffusion flux of point defects into the crystal. The steeper is the decrease in temperature, the higher is the concentration gradient, and the faster is defect diffusion. The diffusion flux is scaled in proportion with the temperature gradient G. It is assumed that the diffusion coefficient of the self-interstitials $D_I(T_m)$ is somewhat higher compared to vacancies $D_V(T_m)$, and so the diffusion flux of interstitials dominates over the diffusion flux of vacancies. Hence, the diffusion is responsible for supplying interstitials into the crystal and the flux of interstitials into the crystal is proportional to the temperature gradient G.

Due to the effective recombination, the defect of lower concentration vanishes and only the other type of the point defect survives in the crystal. The concentration of the point defects above the melt-crystal interface is determined by the competition of the drift flux supplying vacancies and the diffusion flux supplying interstitials. These fluxes are proportional to the crystal growth rate v and to the temperature gradient G, respectively. Finally, the v/G ratio determines the point defect which survives the recombination stage. Point defect recombination proceeds roughly above 1300 °C and a typical temperature profile in the crystals grown in modern CZ pullers results in a recombination length of about 2–3 cm. The v/G ratio in fact determines, whether silicon crystal few cm above the melt crystal interface (or at about 1300 °C) contains vacancies or interstitials.

There is a critical value of the v/G parameter corresponding to the state when the drift and diffusion fluxes (or the vacancy and interstitial fluxes) are balanced. I such case the concentrations of vacancies and interstitials before the recombination are comparable and recombination leaves essentially defect-free crystal. The critical value of v/G, also referred to as ξ, is given by the point defects properties at the melting temperature T_m [43, 107]:

$$\left(\frac{v}{G}\right)_{crit} = \frac{E}{kT_m^2}\frac{D_I C_I^{eq} - D_V C_V^{eq}}{C_V^{eq} - C_I^{eq}}. \tag{5.2}$$

In (5.2), subscripts I and V denote interstitials and vacancies, respectively, E is the defect formation energy averaged over the two species, D and C are the defect diffusivity and concentration and the superscript eq denotes the equilibrium value. A more generalized expression includes the effect of thermal drift (thermodiffusion) [108], which has recently been recognized very important [109]. As it is not critical for explanation of crystal defect formation, we will not go into much detail.

The critical ratio ξ separates two cases: (a) when the crystal growth process results in $v/G < \xi$, defect recombination results in a crystal populated by self-interstitials; while (b) when $v/G > \xi$, the crystal contains vacancies. The two cases are known as the interstitial-type crystal and the vacancy-type crystal. The survived point defects become supersaturated during cooling of the growing crystal, which results in formation of bulk defects — vacancy-type defects in the vacancy-type crystal, or interstitial-type defects in the interstitial-type crystal. Also other features, such as oxygen precipitation, may differ substantially between the vacancy-type and interstitial-type crystals. Silicon lattice rich in vacancies can easily absorb silicon interstitials emitted during the growth of an oxide precipitate, while emission of interstitials into a matrix already rich in interstitials in unfavorable. Oxygen precipitation in a vacancy-type silicon is generally stronger compared to oxygen precipitation in interstitial-rich material.

Taking into consideration the influence of crystal defects on wafer properties and device performance (see section 4.4) one realizes the importance of the crystal growth process, which determines the value of v/G.

5.2. Spatial distribution of defects

Principal distribution of defects in a silicon crystal is determined by the relation of the v/G value to the critical ratio ξ. The crystal growth rate at a given crystal length can be considered constant across the melt-crystal interface from a macroscopic viewpoint. The temperature gradient, however, strongly varies across the radius. Due to cooling of the crystal surface by radiation and convective heat loss to the atmosphere the axial temperature gradient at the melt-crystal interface increases from the crystal center to the perimeter. The v/G parameter thus decreases from the center to the perimeter (see Fig. 5.1).

The relation of the ξ value to the v/G curve determines whether an interstitial-type, a vacancy-type, or a mixed-type crystal is grown, as illustrated in Fig. 5.1. The transition between the vacancy-type and interstitial-type portion of the crystal is called the vacancy-interstitial boundary (V-I boundary).

Let us consider a growing crystal in certain stage of the growth. The growth process yields a radial curve $v/G(r)$. There are three possible relations of the critical value ξ with respect to the $v/G(r)$ curve:

1. if the $v/G(r)$ curve lies below the critical value ξ then the crystal is of interstitial-type in full cross-section;
2. if the $v/G(r)$ curve contains the critical value ξ then the crystal contains a vacancy-type core and an interstitial-type rim separated by a vacancy-interstitial (V-I) boundary at the radius r_{V-I} defined by the equation $v/G(r_{V-I}) = \xi$. The crystal cross-section is of a mixed-type;
3. if the $v/G(r)$ curve lies above the critical value ξ then the crystal is of vacancy-type in full cross-section.

The cross-sections of the three crystal types are demonstrated in Fig. 5.1.

In addition, both the crystal growth rate v and the temperature gradient G vary during the crystal growth, which means that the $v/G(r)$ curve can be shifted up or down for different

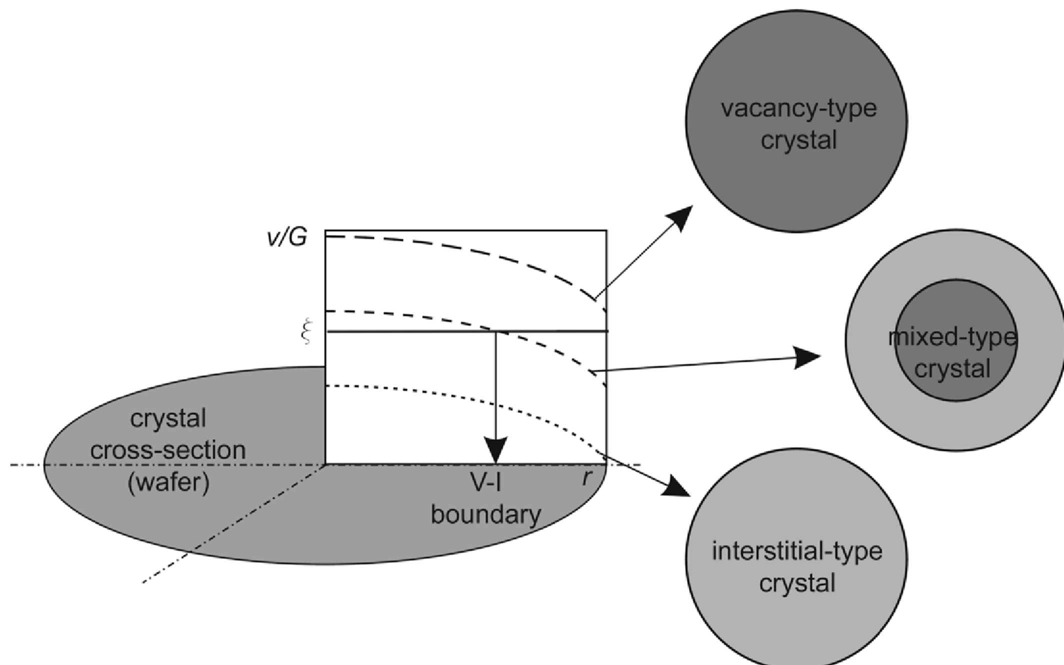

Figure 5.1: Left: A typical radial dependence of the v/G ratio and three possible relations of the $v/G(r)$ curve to the critical ratio ξ. Right: Crystal (wafer) types determined by the relation of $v/G(r)$ to ξ. The cross-section image corresponds to a wafer sliced from the crystal.

positions in the crystal. As a result, the radius of the V-I boundary may not stay constant through the crystal.

Today's FZ silicon crystals are typically of fully vacancy-type due to high growth rate which is typically 2–3 times higher compared to CZ silicon crystals. On the other hand, CZ silicon crystals of all three types shown in Fig. 5.1 can be found. First CZ silicon crystals were of the interstitial-type, due to a relatively high value of G in the crystals of small diameter. Today's 150 mm and 200 mm crystals produced at a rather high pull rates are usually of vacancy-type. The 300 mm crystals may be of the mixed-type and even larger crystals may become fully interstitial-type because of the pull rate which has to be decreased when increasing the crystal diameter up to these levels [110].

As noted above, formation of bulk defects in silicon is strongly influenced by the type of the material. The nature of the crystal from the defect point of view (distribution of the vacancy-type and interstitial-type regions) in principle determines the presence and distribution of bulk defects in the silicon wafers.

5.3. Formation of defects in mixed-type crystals

Let us consider a position in a mixed-type crystal after the point defect recombination. We will focus on the vacancy-rich portion which is interesting from the point of view of oxygen precipitation. The mixed-type crystal contains a vacancy-rich core and an interstitial-rich rim separated by the V-I boundary. The concentration of vacancies is zero in the interstitial-rich region and increases towards the crystal center with increasing distance from the V-I boundary (Fig. 5.2a). Similarly, the concentration of interstitials is zero in the vacancy-rich region and increases towards the crystal rim with the distance from the V-I boundary. Voronkov shows that formation of crystal defects proceeds in several successive stages and significantly modifies these initial concentrations of the point defects [108, 111].

As the temperature is decreased beyond the recombination stage, vacancy supersaturation increases, which results in vacancy agglomeration into voids. The vacancy loss to voids is so strong that the nucleation rate is quickly suppressed and the void nucleation proceeds effectively only in a rather narrow interval around the void nucleation temperature T_n. The void nucleation temperature is assumed to be typically slightly below 1100 °C. Free vacancies tend to bind to oxygen atoms at certain binding temperature T_b which is assumed to lie near 1020 °C. Below T_b vacancies exist in the form of O_2V and OV complexes and are saved from consumption by existing voids. So the voids nucleate and grow only in the temperature range of T_n–T_b. The onset temperature of void nucleation depends on the initial vacancy concentration. The higher vacancy concentration results in higher supersaturation and earlier void nucleation. The higher T_n consequently results in longer time for void growth, which results in higher vacancy consumption into voids. The void formation therefore significantly reduces the initial concentration of vacancies near the crystal center where the initial vacancy concentration is the highest. On the other hand, the initial vacancy concentration near the V-I boundary is so low that T_n is very close to T_b and vacancy consumption to voids is negligible. Here the vacancy concentration remains essentially the same as the initial vacancy concentration. The consumption of vacancies into voids changes the concentration profile of vacancies shown in Fig. 5.2a into a single-peak function shown in Fig. 5.2c. The void concentration is schematically shown in Fig. 5.2b.
At temperatures below T_b interstitial oxygen becomes sufficiently supersaturated to precipitate. Precipitation of oxygen results in formation of oxide particles. The specific volume of oxide is about twice as high as of silicon, so formation of oxide molecule from two interstitial atoms of oxygen and one lattice atom of silicon results in local volume expansion. The excessive volume roughly equals the volume of one silicon lattice atom. For formation of unstrained oxide particle, one vacancy per two oxygen atoms is needed for accommodation of the stress. These vacancies

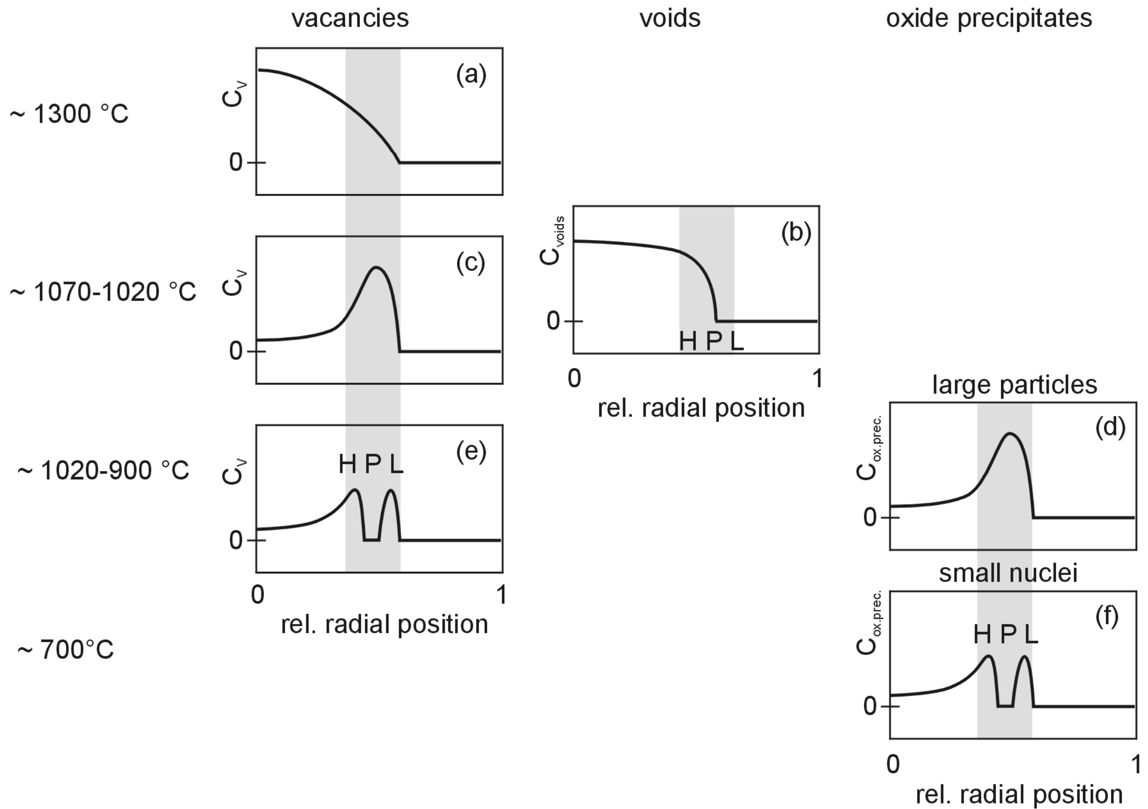

Figure 5.2: Scheme of formation of crystal defects in the vacancy-rich core of a mixed-type crystal.

are considered as consumed during formation of oxide particles. It is assumed that vacancies bound in O_2V and OV species can act in this way. Formation of oxide particles represents the second stage of vacancy consumption. Only the peak of the vacancy profile in Fig. 5.2c provides sufficient vacancy concentration for appreciable nucleation of oxide particles. The growth of the nucleated particles reduces the vacancy concentration and prohibits further nucleation of new particles. The vacancy loss to the growing particles is so strong that essentially all vacancies are consumed and nucleation rate quickly drops. The particle nucleation rate on sides of the vacancy peak of Fig. 5.2c is too low to cause such appreciable vacancy consumption. The vacancy consumption during the oxide particle formation stage transforms the single-peak concentration profile of Fig. 5.2c into a double-peak concentration profile of Fig. 5.2e. The profile represents the "residual" vacancies which survived the consumption into voids and oxide.

The residual vacancy profile sets the basis for banded distribution of defects in silicon crystals. The band where oxide particles were formed and no residual vacancies were left is called a P-band, its neighboring bands are called H- and L-band. The nomenclature originates from observations of oxygen precipitation in silicon wafers [108, 111]. The P-band is characteristic by the strong oxygen precipitation after a high temperature annealing (above 1000 °C), the marginal H- and L- bands are typical by a strong oxygen precipitation after a thermal treatment including a mid temperature nucleation step (700–800 °C). The oxide particles in the P-band are nucleated during the crystal growth at the temperature around 1000 °C. Nucleation of oxide particles proceeds in a limited time interval until free vacancies are consumed, thus the particle density is also limited. The typical density of oxide particles in the P-band is in the order of 10^8–10^9 cm^{-3}. The particles in the P-band reach the size of about 5 nm (10^3 atoms). The nucleation rate in the H- and L- bands around 1000 °C is negligible, but appreciable nucleation is driven by increased oxygen supersaturation at lower temperatures. Growth of the particle nuclei at lower temperatures is rather slow, so the nuclei reach the typ-

ical size of only a few hundreds of atoms and both oxygen and vacancy concentrations do not decrease essentially. The nucleation stage in the L- and H-band, being limited only by temperature, is much longer compared to the nucleation in the P-band, which results in higher defect density. Representative density of oxide nuclei in the L- and H- bands is 10^{10} cm^{-3} and higher. The oxide particles nucleated and grown during the crystal growth will be called the grown-in oxide precipitates in the following text. Their spatial distribution is given by Fig. 5.2d,f.

The distribution of grown-in oxide precipitates leads to a typical precipitation behavior during the subsequent heat treatment of silicon wafers sliced from the crystal [108, 111]. Size of the grown-in precipitates determines their stability at elevated temperatures. A single-step annealing at high temperature (e.g. 1100 °C) therefore results in appreciable oxygen precipitation only in the P-band, which contains supercritical precipitates. The grown-in precipitates in the H- and L-band dissolve during the ramp-up to the high temperature. On the other hand a lower temperature annealing allows growth of all grown-in precipitates to a size that is supercritical at the higher temperatures. The two-step annealing so results in heavy precipitation in the L- and H- bands and in the central area bound by the H-band. The precipitation of oxygen in silicon wafers follows the density and size distribution of the grown-in nuclei formed during the crystal growth.

5.4. The critical v/G ratio

Voronkov estimated the value of v/G_{crit} — the critical value of v/G, denoted also as ξ — to be 0.12 mm^2/min K [107]. The values reported by other authors for a lightly boron-doped silicon and non-doped silicon vary mostly in the range of about 0.12–0.14 mm^2/min K (e.g. [112, 113]). It was found that the critical value ξ is influenced by various impurities, such as dopant atoms, oxygen, nitrogen or carbon [112–114]. The defect distribution thus can vary significantly among crystals of different doping type or level, though being grown by the same growth process. Particularly for boron, the ξ value was shown to increase with increasing boron concentration [112, 114].

5.5. OISF ring

The high thermal stability of the grown-in oxide precipitates in the P-band results in an interesting feature observed on some types of silicon wafers after fast (wet) oxidation of the surface. Due to the difference in bulk density of silicon and silicon oxide, transformation of silicon lattice into oxide lattice is accompanied by huge compressive stress, which is relieved by emission of silicon interstitials [115]. When suitable nucleation sites are present, the supersaturated silicon interstitials agglomerate into extrinsic stacking faults [83, 116]. Considering the prime polished wafer surface, the only nucleation sites present in the near-surface region of the wafer are the grown-in oxygen precipitates. Wet oxidation is usually performed at the temperature above 1050 °C, when most of the grown-in oxide precipitates dissolve, but only the large precipitates in the P-band survive. These precipitates serve as a nucleation center for stacking faults [117]. Oxidation of the wafer so can lead to formation of ring-like distributed stacking faults [118] which decorate the P-band. This feature is referred to as the Oxidation Stacking Fault Ring (in the literature abbreviated as OISF ring or Ring-OSF). The OISF ring is schematically shown in Fig. 5.3.

The OISF ring can be easily visualized on the wafer by stripping the oxide and selective etching of the surface. The etched OISFs are visible by optical microscopy and the OISF ring is detectable even by naked eye.

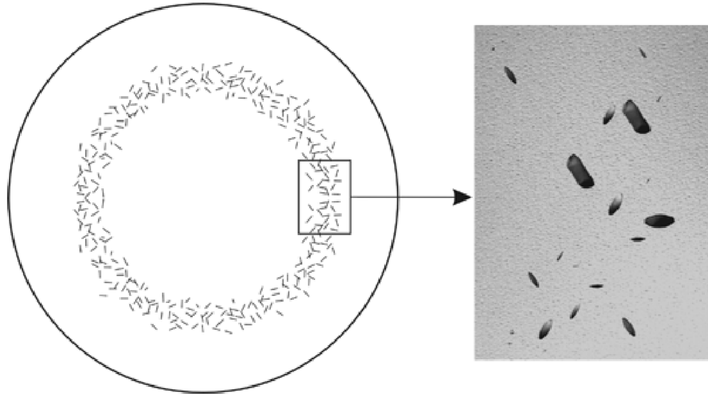

Figure 5.3: Schematic representation of an OISF ring on the surface of a silicon wafer.

The OISF ring decorating the P-band is located on the rim of the vacancy-rich core, close to the V-I boundary. Due to its easy detection it has been widely used for delineation of the V-I boundary and study of defect distribution in silicon crystals.

5.6. Oxygen precipitation

Oxygen precipitation, i.e. formation and growth of oxide (oxygen) precipitates from the supersaturated solid solution of oxygen in silicon, can be characterized as a two-step process consisting of the nucleation stage and the growth stage. Exhaustive introduction into oxygen precipitation theory can be found e.g. in [87, 93].

Nucleation is the process of formation of aggregates of a few oxygen atoms — the nuclei (precipitate embryos). Due to relatively low annealing temperatures (typically 600–800 °C) the supersaturation is high but the diffusivity of oxygen is low. The change in the concentration of interstitial oxygen in the silicon lattice is usually negligible and mainly the precipitate density is established.

Precipitate growth (often referred to as the precipitation stage) is caused by diffusion of oxygen atoms and attachment to the existing nuclei at higher temperatures (typically 1000–1100 °C). While the generation of new nuclei during the precipitation stage is negligible the existing nuclei grow substantially while forming oxide particles of sizes reaching up to the micrometer scale. The supersaturation in this stage is lower but the diffusivity of oxygen is much higher than in the nucleation step. The reduction in the concentration of interstitial oxygen during the precipitation stage may therefore be dramatic.

The influence of various annealing steps on the reduction of interstitial oxygen is shown in Table 5.1. Although shorter annealing at low temperature (750 °C/10h) reduces the interstitial oxygen concentration only by about 1%, the nuclei have sufficient size for further growth during a precipitation step at 1050 °C. It is also shown that even low temperature annealing can reduce interstitial oxygen significantly if the annealing time is extremely long and the initial interstitial oxygen concentration is sufficiently high.

Table 5.1: Influence of annealing temperature and time on the amount of precipitated oxygen in a lightly boron doped wafer with an initial interstitial oxygen content of 38 ppma.

Annealing Step		Precipitated oxygen [%]
750 °C/10h	-	1.0 ± 0.5
750 °C/40h	-	46 ± 3
750 °C/10h	1050 °C/20h	91.4 ± 0.5

Capturing the nucleation stage has been the most disputable problem over the decades of oxygen precipitation studies. The precipitate nuclei are too small to be observed directly, hence only indirect observations were used for model validations. Further complications resulted from uncertainties in thermophysical properties of the involved defects. The topic has been treated by numerous authors, who assumed both homogeneous and heterogeneous nucleation mechanism (see e.g. references in [93]). Regardless of the precise nucleation mechanism, there is a parameter crucial for all theoretical considerations — the critical radius of the nucleus. Starting with a classical nucleation theory [119], the change in the Gibbs free energy (G) related to formation of a (spherical) nucleus of radius r for homogeneous nucleation is given as:

$$\Delta G = 4\pi r^2 \Gamma - \frac{4}{3}\pi r^3 \Delta G_v, \tag{5.3}$$

where

$$\Delta G_v = \frac{kT}{V_p} \ln\left(\frac{C_{ox}}{C_{ox}^{eq}}\right). \tag{5.4}$$

In Eq. (5.3) and (5.4) Γ is the interface energy per unit area, ΔG_v is the volume Gibbs energy related to the variation of the chemical energy of supersaturation per unit volume after oxygen atom is removed from the solution, and V_p is the volume per oxygen atom in the precipitate phase. The first term in Eq. (5.3) corresponds to the gain in the energy of the system related to formation of a new surface; the second term corresponds to the reduction of the energy of the system due to transition of the oxygen atom from the supersaturated solution into the precipitate phase. While the surface energy acts against formation of the nucleus, the decrease in the volume energy drives the nucleation. As the result, the ΔG as a function of the nucleus radius has a maximum at r_c which separates two regions:

(a) for $r < r_c$, energy increase due to large surface/volume ratio of the nucleus makes its existence unfavorable and the nucleus tends to dissolve;

(b) for $r > r_c$, the energy change is negative due to lower surface/volume ratio and the decreasing Gibbs energy of the system favors formation of such nuclei.

The critical radius thus defines the conditions for stable nuclei. The critical radius derived from Eq. (5.3) is written as:

$$r_c = \frac{2\gamma V_p}{kT \ln\left(\frac{C_{ox}}{C_{ox}^{eq}}\right)}. \tag{5.5}$$

The values of critical radius calculated from Eq. (5.5) with equilibrium oxygen concentration after Mikkelsen [120] are shown in Fig. 5.4 for three levels of oxygen concentration. It is shown that the critical radius steeply increases above 1100 °C, hence small oxide precipitates dissolve at high temperatures.

Taking the impact of intrinsic point defects and strain energy into account, Vanhellemont [121] derived a more general expression:

$$\Delta r_c = \frac{2\gamma V_{SiO_x}}{(1+\delta+\epsilon)^3 xkT \ln\left(\frac{C_{ox}}{C_{ox}^{eq}}\right)\left(\frac{C_I}{C_I^{eq}}\right)^{-\gamma}\left(\frac{C_V}{C_V^{eq}}\right)^{\beta} - 6\mu\delta\epsilon}, \tag{5.6}$$

where δ is the linear misfit, ϵ the constrained strain and μ shear modulus of silicon and V and I stand for vacancies and interstitials, respectively. The strain originates from the fact that molecular volume of all oxide phases SiO_x is larger than that of silicon. The expression assumes partial relief of the strain by emission of γ interstitials and absorption of β vacancies per precipitated oxygen atom.

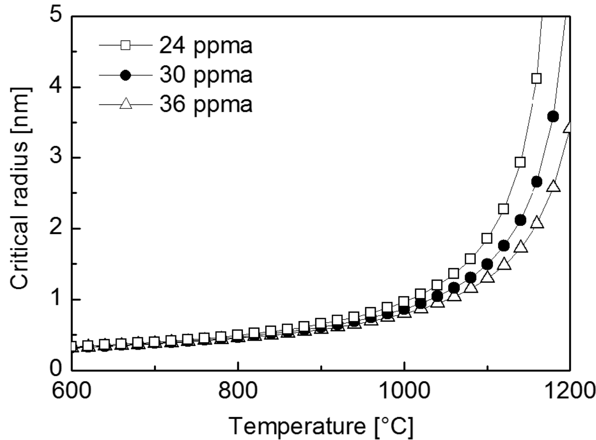

Figure 5.4: Critical radius calculated after Eq. (5.5) with equilibrium oxygen concentration after Mikkelsen [120]. The legend shows actual oxygen concentration in [ppma] per ASTM '79.

Eq. (5.6) corresponds to process of oxygen precipitation described by Eq. (5.7) [177]:

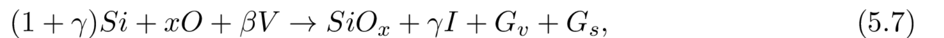

$$(1+\gamma)Si + xO + \beta V \rightarrow SiO_x + \gamma I + G_v + G_s, \tag{5.7}$$

where G_v and G_s stand for energy associated with volume and interfacial strain per molecule, respectively; and $1 < x < 2$, $0 < \gamma$, and $\beta < 1$.

In order to overcome the lack of analytical methods for the nucleation stage, the experimental studies often utilize thermal treatment of the wafers for growing oxide precipitates to the detectable size and deducing nucleation processes from the precipitation behavior. The early work resulted in the establishment of procedures for optimization of oxygen precipitation, e.g. for intrinsic gettering. Classical precipitation treatment of silicon wafer consists of a low temperature nucleation step (around 700 °C) followed by a high temperature precipitation step (around 1000 °C). The amount of oxygen precipitated during heat treatment is often expressed in terms of reduction in the concentration of interstitial oxygen measured by IR spectroscopy as in Tab. 5.1.

While the nucleation stage of oxygen precipitation has remained rather mysterious until today, the growth of oxide precipitates became soon experimentally well described. As showed by many authors (e.g. [122] and references within), oxide precipitates formed during wafer thermal treatment usually show the diffusion-limited growth according to the theory of Ham [119]. The growth controlled by oxygen diffusion results in the square-root dependence of precipitate size on annealing time at a given temperature. However, due to several assumptions, the Ham's theory is not always applicable. The early works usually considered silicon wafer as "clean" input material, but it has been gradually recognized that some nuclei are formed already during the silicon crystal growth [93, 123] and the importance of the so called thermal history and intrinsic point defects became recognized [111, 121, 124].

The present investigations of defect formation in silicon thus start from the early beginning of the crystal growth and the interplay of all intrinsic and extrinsic point defects present in the crystal is considered.

6. Methods of studying crystal defects

In order to capture the distinctive nature of crystal defects and the wide range of their size and density, various methods are used for defect analyses. The most common techniques are briefly introduced in following section.

6.1. Fourier transform infrared spectroscopy

Fourier transform infrared spectroscopy (FTIR) is the most common technique for determining the concentration of interstitial oxygen in silicon materials. The polychromatic source radiates infrared (IR) light through a Michelson interferometer. The radiation is transmitted through the silicon wafer and directed to a detector. Undoped silicon is transparent to the IR radiation. Impurities cause localized absorption from lattice vibrations. The absorption at 1107 cm^{-1} has been assigned to the anti-symmetric vibrational mode of interstitial oxygen and it is thus used for determining the oxygen concentration. In order to suppress the influence of the silicon lattice vibrations and to allow the quantitative analysis, a reference spectrum is subtracted from the measured spectrum. The reference spectrum is measured on float-zone silicon prepared with very low oxygen content (less than 1×10^{16} cm^{-3}). After signal processing and taking the wafer thickness into account, the intensity of the oxygen absorption peak is calculated, and thus, the concentration of oxygen may be determined as the product of the peak intensity and a tabulated conversion factor. The selected conversion factor has to be reported together with the concentration value. The oxygen concentrations presented in this work are given in accordance with the ASTM standard [77] (commonly referred to as "Old ASTM" or ASTM '79). The FTIR method is not applicable for heavily-doped silicon as this material is not transparent to IR radiation due to the high concentration of free carriers.

As the contribution of precipitated oxygen atoms to the absorption peak of interstitial oxygen is small (absorption energies are shifted), the FTIR measurements of interstitial oxygen concentration can be used for characterization of oxygen precipitation. The difference in the content of interstitial oxygen prior to, and after, the heat treatment is the measure of oxygen precipitation, relevant for the specific sample material and thermal cycles. For overall characterization of a crystal grown by a particular growth process the dependence of the precipitated oxygen on the initial oxygen concentration is constructed for a standardized thermal cycle. The dependence is called the "S-curve" because of its typical sigmoidal shape (Fig. 6.1). Another

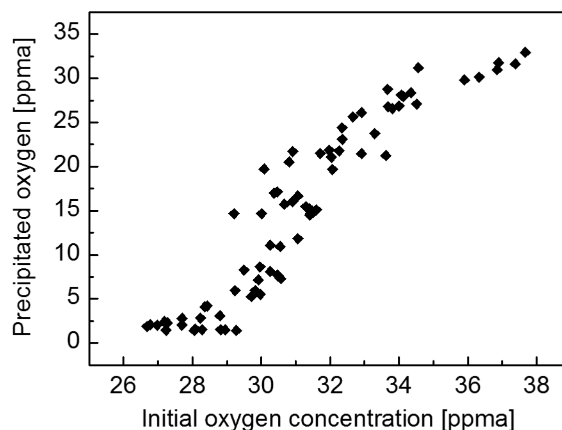

Figure 6.1: Example of an "S-curve" characterizing oxygen precipitation in the crystal grown by a particular crystal growth process.

application of the S-curves is the comparison of different thermal cycles (e.g., in IC production) with respect to oxygen precipitation.

The shape of the S-curve demonstrates that the concentration of interstitial oxygen in the wafer is the primary driving force for oxygen precipitation. Precipitation for low oxygen concentration is rather week, hence there is no significant reduction in interstitial oxygen. At sufficiently high oxygen concentration almost all interstitial oxygen is transformed into oxide precipitates. The intermediate region connects these two extremes. Oxygen precipitation can be effectively controlled by optimization of oxygen concentration only within this region.

6.2. Precipitation test

This test is aimed at assessing the precipitation behavior in the wafers. Oxide precipitates formed in the crystal during growth (grown-in precipitates) are usually too small to be detected directly as noted previously. Oxygen precipitation is therefore evaluated in silicon wafers subjected to a standardized thermal treatment sequence.

Generally, two types of the heat treatment are used: (a) single step annealing at high temperature when the grown-in oxide precipitates are allowed to grow, and (b) two-step annealing which includes also a low-temperature nucleation step. Typical representatives of such treatments are the ASTM standard A-test (1050 °C/16h) and B-test (750 °C/4h + 1050 °C/16h) [125]. The extent of oxygen precipitation is evaluated as the difference in interstitial oxygen concentration before, and after, the thermal treatment as measured by FTIR, or by "cleave-and-etch" analyses. In such cases, the wafer cross-section is prepared by cleaving or grinding, the sample is preferentially etched, and the defect distribution and density is evaluated under the microscope. An example of the cleave-and-etch analysis is shown in Fig. 6.2.

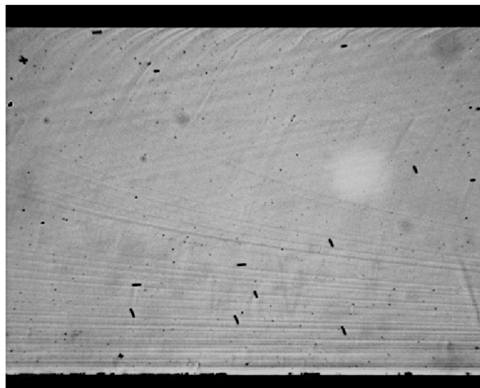

Figure 6.2: A wafer cross-section prepared by the cleave-and-etch method. The wafer front surface (polished) is at the top of the figure. The analysis reveals oxide precipitates (dots) and stacking faults (short lines) in the bulk of the wafer.

6.3. Preferential etching

Analytical methods based on preferential etching of silicon are frequently used for studying defects in silicon technology [126]. All modern defect etchants for silicon are based on the chemistry of formation and dissolution of silicon dioxide, and therefore all etchants include hydrofluoric acid. The formation process is enhanced at and around defects due to weakened bonds and coalescence of impurities around them. The electronic properties may play a role, too. Etching anisotropy with respect to various crystallographic planes (atom density) also has to be taken into account. In general, the etch rate is lowest for planes with the highest densities, i.e.,

the {111} crystal planes [127]. Various etchants were developed which are optimized for delineating defects by etching of particular crystal planes, dopant type and concentration. The most common etching solutions are listed in Tab. 6.1.

Table 6.1: Common etchants for delineating defects in silicon. For more details on use and application see e.g. [127] or [126].

Etchant	Formula	Usage
Wright [128]	HF(49%):HNO_3(70%):CrO_3(5M): HAc(100%):H_2O:$Cu(NO_3)_2 \cdot 3H_2O$ 2:1:1:2:2:2g/240 ml	good for all orientations
Sirtl [129]	HF(49%):CrO_3(5 M) 1:1	optimized for (111)
Schimmel [130]	HF(49%):CrO_3(5 M) 2:1	optimized for (100)
Yang [131]	HF(49%):CrO_3(1.5 M) 1:1	good for all orientations good for grown-in dislocations
Secco [132]	HF(49%):$K_2Cr_2O_7$(0.15 M) 1:1	optimized for (100) unsuitable for heavily doped p-type
MEMC [133]	HF(49%):HNO_3(70%): HAc(100%):H_2O:$Cu(NO_3)_2 \cdot 3H_2O$ 36:25:18:21:1g/100 ml	chromium-free unsuitable for heavily doped
Dash [134]	HF(49%):HNO_3(70%):HAc(100%) 1:3:10	chromium-free unsuitable for heavily doped n-type

Preferential etching allows for rather simple detection of dislocations, stacking faults, slip lines, and oxide precipitates as shown in Fig. 6.3. Individual defects on the etched surface may be observed by optical microscopy or SEM, while defect distributions across a wafer can be observed by the naked eye in most cases.

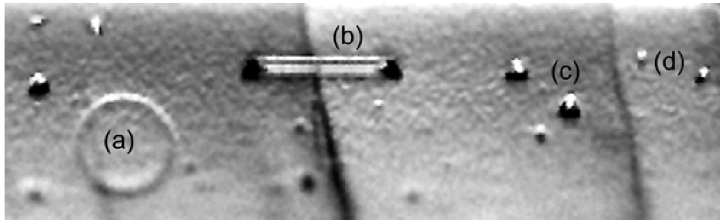

Figure 6.3: Defects in silicon revealed by preferential etching of a cleaved surface. (a) A stacking fault in the cleavage plane, (b) a stacking fault tilted with respect to the cleavage plane (note the bounding dislocation), (c) dislocations, (d) oxide precipitates.

6.4. X-ray topography

X-ray topography [135] is based on Bragg diffraction. Incident monochromatic X-ray beam of wavelength λ is reflected by atomic planes of the crystalline sample and constructive interference occurs when the Bragg condition is fulfilled:

$$n\lambda = 2d \sin\theta. \tag{6.1}$$

Here θ is the angle between the incident beam and the diffracting planes, d is the interplanar distance of the diffracting planes, and n is an integer. The diffraction pattern is recorded on the detector either in reflection geometry (Bragg geometry) or transmission geometry (Laue geometry).

In the case of section topography, a very narrow beam of dimensions in the order of 10 μm is used (a slit or hole is used to restrict the beam). The section topograms therefore investigate only a small volume, the section, of the sample. The beam is diffracted at different depths, each one contributing to the image on a different location on the detector. Section topography is therefore used for depth-resolved defect analysis. When the sample and detector are simultaneously moved with respect to the incident beam, the sample is scanned over a larger volume and a projection topogram is formed. The geometry of section/projection topography in Laue geometry is shown in Fig. 6.4a; Fig. 6.4b and c show typical topograms of silicon wafers.

Homogeneous crystal lattice generally results in homogeneous distribution of intensity across the topogram. The section topography, however, results in spatial variation of intensity of diffracted rays even on perfect crystal (so called Pendelösung fringes) due to dynamic nature of diffraction and small investigated volume [136]. Irregularities of the crystal lattice, such as defects and strain, are captured as distortion of the image of the perfect crystal. X-ray topography can detect irregularities as phase boundaries, defective areas, cracks, scratches, growth striations, and most common crystal defects such as dislocations, oxygen precipitates, stacking faults, and interstitial-type defects.

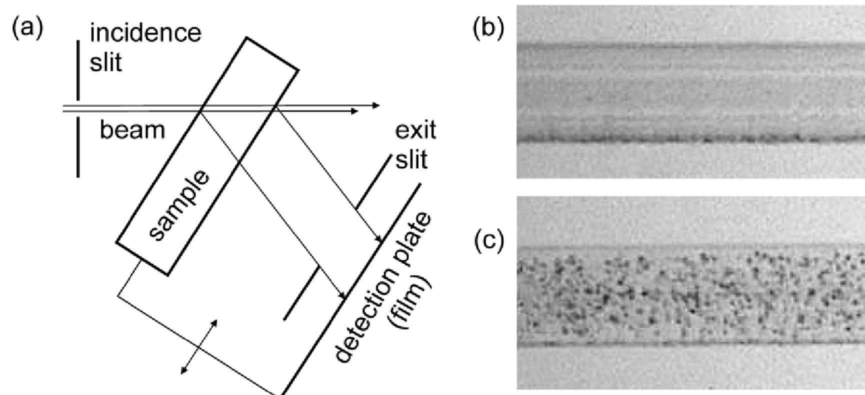

Figure 6.4: (a) Geometry of the X-ray section and projection topography in Laue geometry. (b) Section topogram of defect-free silicon wafer. Horizontal Pendelösung fringes are clearly visible. Strain related to the polysilicon layer on the wafer back side (bottom) results in dark features in the topogram. (c) Section topogram of a silicon wafer showing oxygen precipitates (dark spots) and residual damage on the wafer back side (bottom).

6.5. OISF test

OISF test utilizes the fact that silicon interstitials injected below the wafer surface during its oxidation under usual conditions need a suitable nucleation site for formation of OISF (section 4.3.3) [83, 116]. The tested wafer passes an oxidation cycle (e.g. 1000 °C/1h in wet atmosphere, [137]), the grown oxide is stripped by HF acid and the surface is preferentially etched. The stacking faults observed on the surface decorate the nucleation centers in the near-surface wafer region. The nucleation sites can arise from the surface and subsurface damage caused by manufacturing processes, handling, etc., from wafer contamination, and defects such as dislocations and oxygen precipitates. The OISF test is therefore used as a general test for the quality of wafer surface. Supposing that the wafer manufacturing process is optimized and wafer contamination avoided, OISF test can be used for delineation of crystal defects in the wafer as in the case of the OISF ring (section 5.5).

6.6. Chromium-free OISF test

While the appearance and local density of OISF (after the OISF test) is evaluated under optical microscope, there is no "user-friendly" method for analysis of OISF distribution over the wafer surface. OISF distribution is observed by naked eye under collimated light, but mapping and digitalization are unattainable. There are, of course, tools for mapping of wafer surface (routinely used for particle measurement), but these are used for analysis of prime production wafers. However, analysis of wafers after the OISF test comprises unacceptable risk for wafer production line because of chromium contamination originating from etchants such as Wright, Sirtl etc., used for preferential etching of OISF. In order to overcome these obstacles, we have introduced, in the scope of this PhD work, a modification of the OISF test yielding uncontaminated wafers suitable for analysis by production particle detectors. Example of the OISF map taken using this technique is shown in Fig. 6.5.

The process was designed while taking into account the chemicals, procedures and tools available in a wafer manufacturing line. First, well known chromium-free etchant, the Dash etch [134], was explored, but the results were unsatisfying. We have therefore optimized the HNA system (mixture of the Hydrofluoric, Nitric, and Acetic acids) for our purposes and obtained the best results with a mixture of HF:HNO_3:HAc 1:4.4:4.4. Using this etchant instead of conventional,

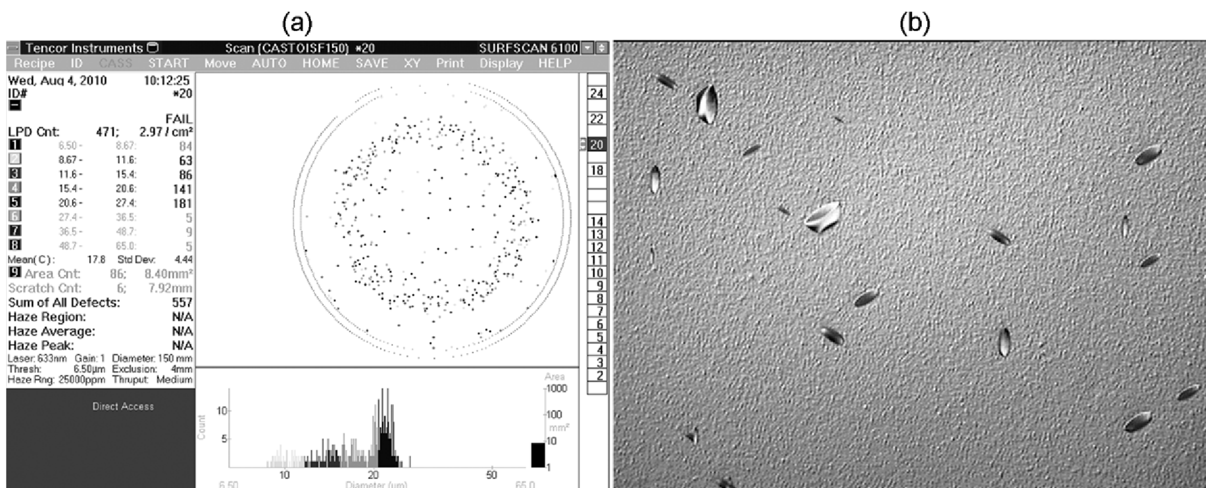

Figure 6.5: (a) Picture of OISF distribution taken on the KLA-Tencor Surfscan 6200 particle detector after the chromium-free OISF test. (b) Optical microscope picture of the OISF after the chromium-free OISF test.

chromium containing, etchants, we delineated OISF on the surface of the wafer and were able to analyze the OISF distribution over the wafer surface with a commercial particle counter (KLA-Tencor Surfscan).

6.7. COP test

Delineation of COPs (section 4.3.4) is based on SC1 cleaning and "particle" inspection [70]. As the typical COP dimensions do not allow direct observation on the polished wafer surface by common industrial equipment, the SC1 cleaning is utilized to slightly etch the COPs and enlarge them above the detection limit of the used instruments. The size of COP defects after the SC1 treatment is typically 100–300 nm and the surface density is in the order of 10^0–10^1 cm^{-2}.

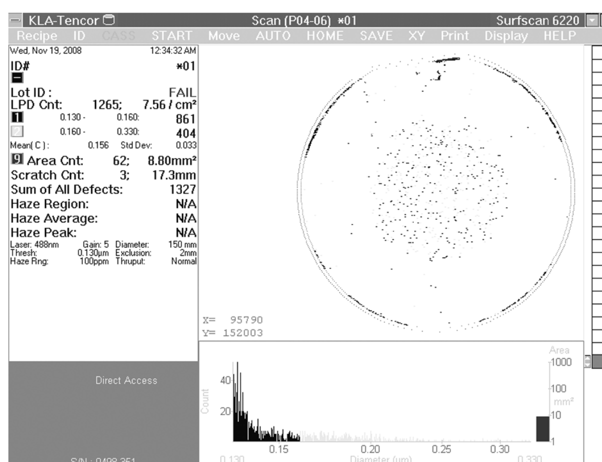

Figure 6.6: Measurement of the COP distribution on polished silicon wafer after SC1 treatment. COPs are concentrated in the vacancy-rich core of the wafer; particles detected outside the vacancy-rich core demonstrate the cleanliness level of the test. Majority of detected COPs are of the size close to 130 nm, which is the lower detection limit of the equipment.

The COP detection technique was introduced to ON Semiconductor Czech Republic in the scope of this PhD work. Suitable wet hood was found and the etch bath was designed, purchased and installed. The etching process was set up to a commonly used procedure: polished silicon wafers are rinsed in the SC1 solution ($NH_4OH : H_2O_2 : H_2O$ = 1:1:5) at 70–80 °C for 4 h, cleaned in DI water, dried and inspected by an industrial particle counter (KLA-Tencor Surfscan). Example of the measurement output is shown in Fig. 6.6.

6.8. Copper decoration

Development of crystal growth needs, among others, fast evaluation of grown-in crystal defects. The fastest information is gained just after crystal cropping on thick (1–3 mm) wafers (called slugs) sliced from several positions in the crystal. However, preferential etching of defects on non-polished silicon is very difficult because of huge density of etch pits originating from surface damage. A very useful technique was developed by Mule'Stagno [138] which is capable of defect analysis on rough silicon surface.

The copper decoration technique utilizes intentional contamination of the wafer by copper, which precipitates on crystal defects during cooling from elevated temperature. Copper is introduced into the wafer by spreading a film of Copper Nitrate ($Cu(NO_3)_2{\cdot}5H_2O$) solution on the wafer surface. The film is then left to dry; the wafer is annealed at 900 °C for about 15 min

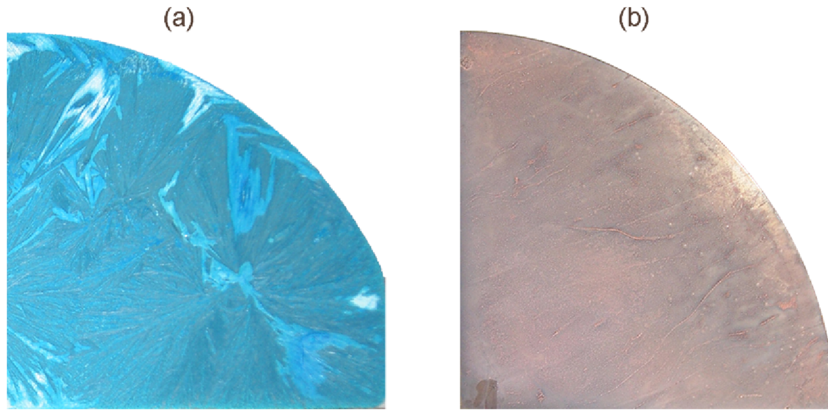

Figure 6.7: Quarters of silicon slugs after copper application (a) from the Copper Nitrate solution, and (b) deposition of metallic copper.

and air-cooled to room temperature. After chemical polishing, the wafer surface is preferentially etched and defect distribution evaluated by naked eye under bright or room light.

The copper decoration technique was introduced to ON Semiconductor Czech Republic in the scope of this PhD work and the method was further enriched by improved procedure of introducing copper into the wafer (see ref. [VII]). The film of metallic copper was deposited on the wafers by immersion into 1 mol/l solution of $Cu(NO_3)_2$ with the addition of HF for 5 min. This solution (a) is environment-friendly, because it avoids formation of nitrogen oxides during annealing of the Copper Nitrate film, and (b) allows simple application of copper on several samples simultaneously. Samples after copper application are shown in Fig. 6.7. The decorated wafers are heated at 900 °C for 30 min, air cooled, chemically polished in the solution of HNO_3, HF and CH_3COOH acids, and preferentially etched.

While Mule'Stagno reports that both the interstitial-type and vacancy-type defects as well as oxide precipitates are delineated by copper decoration, we were able to delineate only oxide precipitates. As the growth of oxide precipitate requires free vacancies, appreciable oxygen precipitation usually takes place only in the vacancy-rich region. Indeed, the V-I boundary was detected as the outer diameter of the oxygen precipitation region. Various preferential etchants were tested, see [VII] for details. While common etchants such as Secco or Wright delineated individual precipitates, the silver-based solution (HNO_3(65%) + HF(50%) + aqueous solution of $AgNO_3$(1%) + DI water) resulted only in the higher etch rate in the region of high

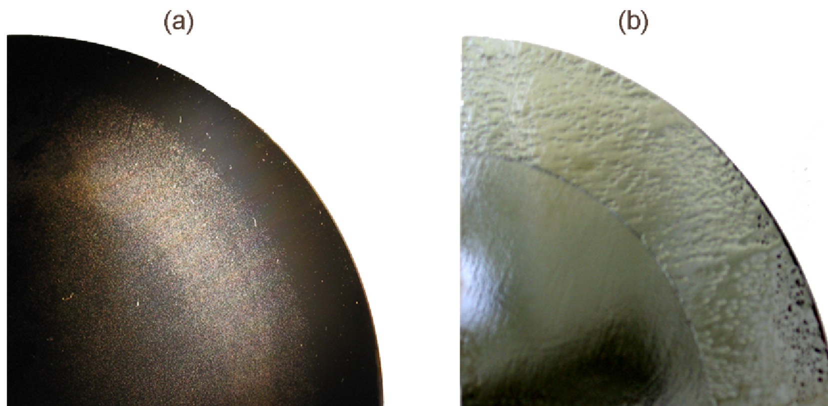

Figure 6.8: V-I boundary delineated via oxide precipitates in the vacancy-rich region by modified copper decoration method on two different wafers. The samples were preferentially etched with (a) Wright, (b) silver-based solution.

oxygen precipitation (see Fig. 6.8 for examples of the results). The V-I boundary was, however, successfully delineated by all used variants.

6.9. Computer simulations

Distribution of crystal defects in silicon wafers is significantly predetermined by formation of defects during the crystal growth. Incorporation of point defects into the crystal and formation of crystal defects are driven by the time evolution of temperature, which governs solubility and diffusivity of the involved species. However, measurement of the temperature field (necessary for its control) in the growing crystal is practically impossible. The analysis of grown-in defects after the crystal growth is very difficult due to their small size, which is often below the detection limit of common techniques. Dedicated numerical models have been developed to overcome these obstacles by computer simulations, which help to describe and predict defect formation from the crystal growth up to wafer processing and device manufacturing (e.g. [139–149]).

The most advanced simulations of the thermal field in the puller, which is the bridge between process parameters and defect evolution, are provided by so called global models. Global simulations take into account heat exchange among all parts of the crystal growth system and consider most complete physics of the process. Several models dedicated for simulation of the Czochralski crystal growth became available during last years [150–153]. The finite element code FEMAG [151], used in ON Semiconductor CR, is introduced in more details in chapter 8.

Computer simulations are not only a powerful tool for study and control of crystal defects, but have been widely utilized for development and optimization of the crystal growth process [154–156]. Simulations are extremely useful especially for introduction of new products such as large-diameter silicon crystals [154–160], and new processes such as magnetic Czochralski growth [161–163] or continuous growth [164].

7. Engineering of crystal defects in silicon

Defect engineering in production manufacture of silicon wafers comprises modifications of the crystal growth process and dedicated heat treatment of the wafers. The primary objective is usually the control of oxygen precipitation and the associated defect structures. The specific requirements on the spatial distribution, size and density of oxide precipitates may differ for various devices, but the basic features are essentially the same. It is desirable to achieve a defect-free region near the surface of the wafer so that the devices fabricated there do not suffer from the electrical effects resulting from the presence of the defects. On the other hand, a high density of oxide precipitates is usually required in the bulk of the wafer in order to provide effective intrinsic gettering. The near-surface region free of oxide precipitates is called a "denuded zone".

7.1. Denuding and precipitation of oxygen

The classical procedure for forming the desired denuded zone and achieving intrinsic gettering utilizes a three-step thermal treatment [165] demonstrated in Fig. 7.1a. The first step is the denudation at high-temperature which results in dissolution of the grown-in oxide precipitates and subsequent out-diffusion of the oxygen from the wafer surface. Oxygen diffusivity above 1100 °C is sufficiently high to result in a depleted zone of several tens of micrometers deep, while the oxygen concentration in the bulk far from the wafer surface retains its initial value. The shape of the transition from the solubility limit value at the surface to the bulk value is determined by the annealing time (Fig. 7.1b, $C_0 = 31$ ppma).

The second step causes the nucleation of new oxide precipitates at temperatures around 700 °C. During the third step, called the precipitation stage, nucleated oxide precipitates grow in the regions of sufficiently high oxygen concentration, while no oxide precipitates grow in the depleted region near the surface and the denuded zone is formed. The experimentally observed limit of oxygen concentration necessary for appreciable precipitation is around 26 ppma (see Fig. 7.1b) and varies depending on the type and concentration of dopant species.

The depth profile of the precipitated oxygen in the silicon wafer can be calculated on the basis of the interstitial oxygen depth profile [93]. As shown in Fig. 7.1b, the oxygen concentration

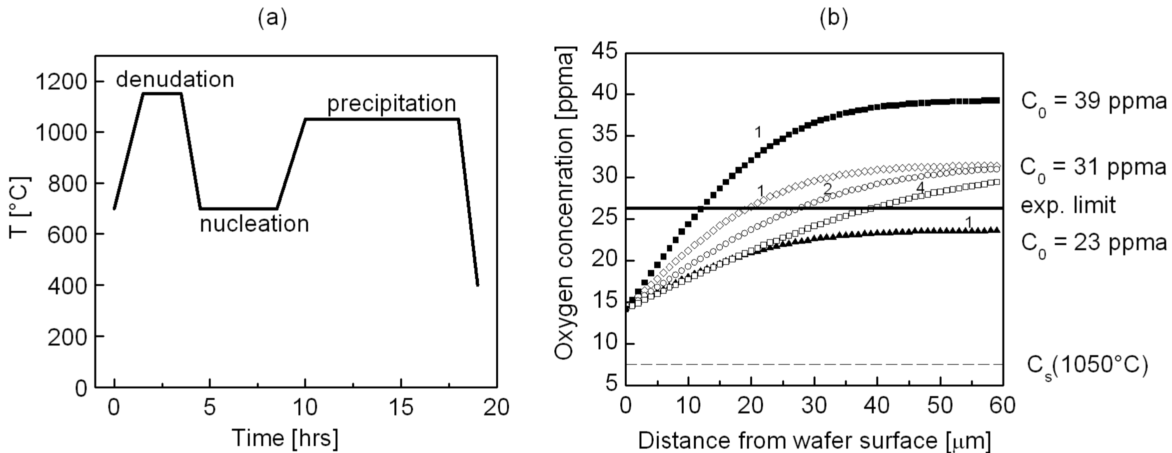

Figure 7.1: (a) An example of a thermal cycle for formation of the denuded zone and effective intrinsic gettering. (b) The concentration of oxygen in the wafer with initial oxygen concentration C_0 denuded at 1150 °C. Denuding duration in hours is noted in the plot below the curves. The thin horizontal line in (b) represents the equilibrium concentration of oxygen at the temperature of the precipitation step (1050 °C); the thick solid line represents the experimental limit of oxygen precipitation. Out-diffusion profiles in panel (b) were calculated after [166].

after out-diffusion provides certain supersaturation even in the denuded zone, but the amount of precipitated oxygen depends more strongly on the density of nuclei than on the level of oxygen supersaturation during precipitation. This latter point is critical in making material stable to large thermal budget wafer processing. The nucleation rate during the second step is very strongly reduced for low oxygen concentrations in denuded zone, e.g., the rate was reduced by more than ten times for oxygen concentration reduced by 8 ppma [93]. As a result the region near the surface is precipitate-free and the bulk region is precipitate-rich. The transition between the bulk and the surface is not sharp; it follows the initial oxygen profile (see Fig.7.3 below).

7.2. Wafer annealing

It was found that high temperature annealing can help control and manage also other types of crystal defects, not simply oxide precipitates. The COP defects on the wafer surface can be annihilated during high temperature annealing in hydrogen [167], or in argon ambient [168]. As shown in Fig. 7.2, proper treatment of the polished wafer can significantly reduce or even eliminate COP defects on the surface of polished silicon wafers. However, attention has to be paid to oxygen precipitation in the bulk of the wafer, since during the high temperature annealing applied for annihilation of COPs (above 1200 °C) the grown-in oxide precipitates tend to dissolve. Subsequent oxygen precipitation in the annealed wafer may become suppressed and the wafer can loose its gettering capability.

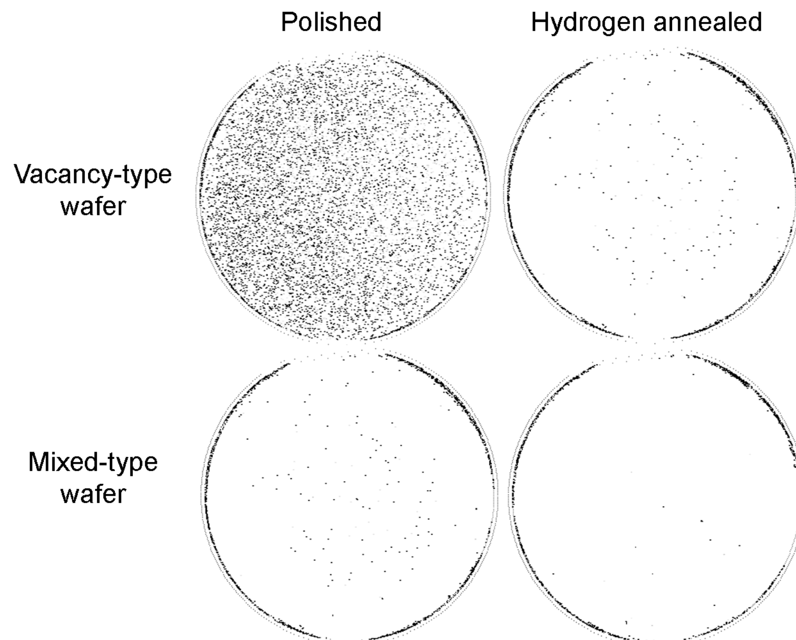

Figure 7.2: COP distributions measured by a particle detector (lower dimensional detection limit is 0.13 μm) on polished and hydrogen annealed wafers, respectively.

7.3. Optimization of oxygen concentration

The denuded zone and intrinsic gettering are closely related to oxygen precipitation, which in turn strongly depends on the oxygen concentration in the wafer. Fig. 7.1 demonstrates the thickness of the denuded zone, and Fig. 7.3 shows the density of oxide precipitates, both as the function of oxygen concentration. As the oxygen concentration in silicon is determined

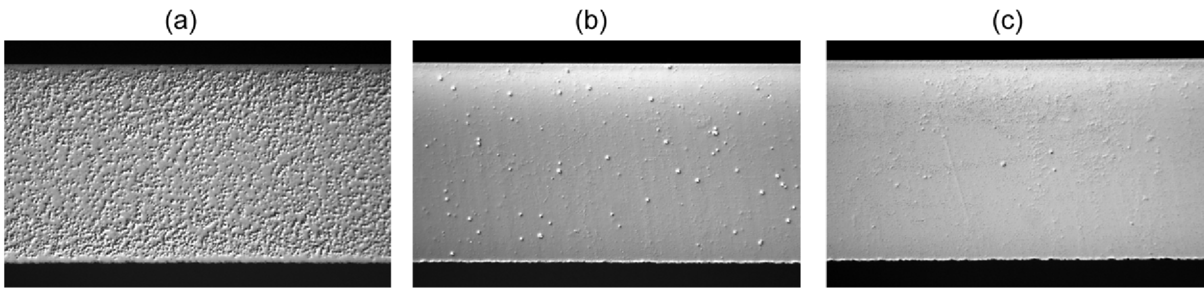

Figure 7.3: Oxide precipitates delineated by preferential etching after 750 °C/4 h + 1050 °C/16 h annealing in lightly phosphorus-doped silicon wafers with oxygen content of (a) 31.5 ppma, (b) 27.5 ppma, (c) 23.5 ppma.

during the crystal growth process, control of the oxygen concentration in the growing crystal is one of the primary tasks for crystal growers.

As was previously discussed, oxygen is incorporated into the crystal at the melt-crystal interface, while its concentration in the crystal relates to concentration in the melt. The concentration of oxygen in the melt below the crystal interface is determined by the strength of the source (crucible materials), by the effectiveness of the transport in the melt, and by the strength of the sink, i.e., by the dissolution rate of the silica crucible, by the melt flow, and by the evaporation from the melt surface. Critical process parameters driving these phenomena are the hot zone design, the crucible rotation rate, and gas atmosphere parameters. All of the parameters are usually optimized to reach a desired oxygen concentration in the whole crystal with limited variation and good reproducibility. Typical concentrations of oxygen in CZ silicon crystals range from about 40 ppma down to about 24 ppma; special designs of the hot zone (usually utilizing shields for gas flow control) allow decreasing oxygen concentration slightly below 20 ppma.

There are applications which require extremely low oxygen concentrations or very uniform distributions of oxygen in the crystal. These requirements are beyond the capability of most standard Czochralski crystal growth processes. Magnetic Czochralski process (MCZ) has to be used to achieve reduced concentrations of oxygen in the silicon crystals. The principal aspect of MCZ lies in the influence of the Lorentz force on the convection in the melt, which arises from the interaction of magnetic field with the fluid flow of the highly electrically conductive silicon melt. The effect of various kinds of magnetic fields has been studied extensively [169]. Based on many investigations, only transverse (horizontal) and cusp magnetic fields are used in indus-

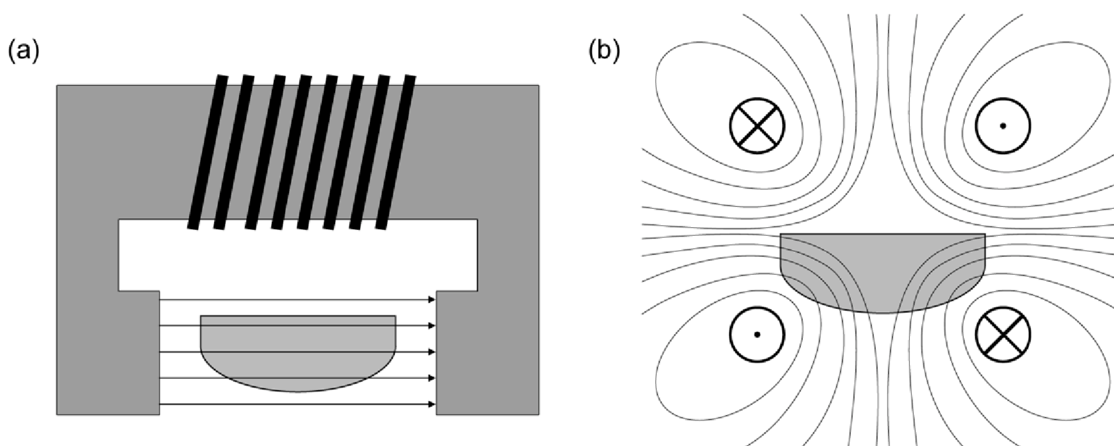

Figure 7.4: Schematic drawing of (a) transverse and (b) cusp magnetic fields for control of the melt convection during crystal growth.

trial applications. The two configurations are schematically shown in Fig. 7.4. The horizontal magnetic field is used for growth of large diameter crystals, while for smaller diameter crystals the cusp field is applied. The two most important effects of the magnetic field generally consist in damping of micro-scale growth rate instabilities at the melt-crystal interface through damping of melt temperature fluctuations, and in the possibility of tuning the incorporation of impurities into the growing crystal. Application of the magnetic field adds additional degrees of freedom to the crystal growth process which widens the capability of the process, but simultaneously brings complexity related to the higher technological level of the process.

7.4. Nitrogen doping

Extremely low oxygen concentration allows for the formation of very deep denuded zones, but also results in negligible oxygen precipitation in the bulk. Oxygen precipitation is generally low also in heavily-doped n-type wafers due to enhanced evaporation of dopant atoms in the form of oxides. Tis drawback can be solved by nitrogen doping for applications requiring effective intrinsic gettering. Introducing nitrogen in silicon crystal results in enhanced precipitation of oxygen during subsequent wafer annealing due to stable nuclei formed during the crystal growth, an increased concentration of free vacancies available for oxygen precipitation and consumption of the interstitials emitted during the precipitate growth [170]. Effective intrinsic gettering then can be achieved even at low oxygen concentrations or under conditions of unfavorable thermal treatments, such as argon or hydrogen annealing [171]. The effect of nitrogen doping on oxygen precipitation is demonstrated in Fig. 7.5.

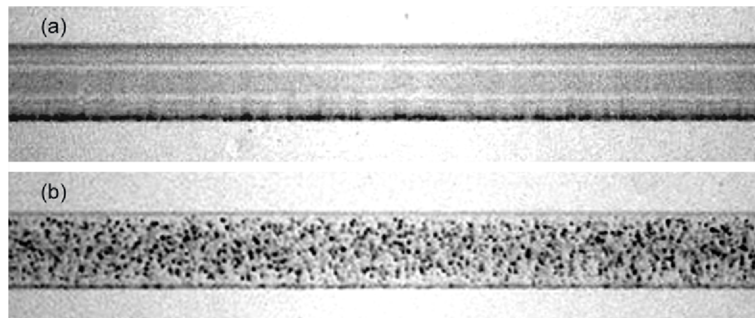

Figure 7.5: An X-ray section topogram showing the effect of nitrogen doping on oxygen precipitation in heavily antimony-doped wafers with low oxygen concentration. (a) Standard wafer. (b) A wafer co-doped with nitrogen at the level of 5×10^{14} cm^{-3}. Wafer (a) is "defect-free". The horizontal Pendelösung fringes are clearly visible (see section 6.4). Strain related to the polysilicon layer on the wafer backside (bottom) results in dark features in the topograph. A section topogram of wafer (b) shows oxide precipitates (dark spots) and residual damage on the wafer backside (bottom). The wafer thickness is 625 μm.

7.5. Vacancy-controlled denuded zone

An elegant solution to overcome the dependence of denuded zone parameters on the oxygen concentration was developed by Falster et al. [172]. The concept of so-called "Magic Denuded Zone" (MDZ) utilizes the importance of vacancies for oxygen precipitation. The concentration profile of vacancies in the wafer is modified via rapid thermal annealing (RTA). Annealing at temperatures of about 1200 °C forms a population of vacancies and interstitials in equal concentrations through the generation of Frenkel pairs. Point defects reach their equilibrium concentrations

in a short period (a few tens of seconds) throughout the thickness of the thin wafer by diffusion to and from the surface. During cooling of the wafer to low temperatures, the equilibrium concentrations of point defects decreases, providing a driving force for enhanced diffusion and recombination. This favors diffusion to the surface, where equilibrium is maintained. However, when the cooling rate is fast enough, the diffusion is effective only in the near-surface region. In the bulk of the wafer, only point defect recombination takes place leaving behind a population of excess vacancies at a concentration given by $C_V^{eq}(T_a) - C_I^{eq}(T_a)$, where T_a is the annealing temperature. The MDZ wafer finally contains an essentially vacancy-free surface and a transition region below the surface with steadily increasing vacancy concentrations up to the bulk level.

When an MDZ wafer passes through a high temperature anneal oxide precipitates nucleate and grow only in the region with sufficient vacancy concentrations which results in the denuded zone at the wafer surface. The depth of the Magic Denuded Zone can reach even deeper into the bulk than the classical denuded zone, but the solution has another major advantage — the result is practically independent of oxygen concentration in the wafer. Although the MDZ comprises an extra treatment of the wafer it suppresses the need for complicated oxygen control in CZ silicon crystals.

7.6. Optimization of v/G

Sometimes annealing of the wafer cannot meet the requirements of the wafer processing thermal budget. In such cases, formation of defects in the wafer can be adjusted by controlling the distribution of point defects in the growing crystal. As described above, vacancy-type or interstitial-type regions are formed in the crystal depending on the v/G parameter. The different regions within the crystal contain different types of defects and also substantially differ in oxygen precipitation characteristics. Tuning of the crystal growth rate v, and/or the temperature gradient G can shift the V-I boundary and so influence defect formation.

There are often issues with excessive oxygen precipitation in heavily-boron doped wafers which results in electronic devices with excessive leakage currents. Analyses of our material showed that the strong precipitation is confined within the vacancy-type region in the seed-end of crystal (which is the crystal portion with the highest oxygen concentration) [V, VI]. If the oxygen profile of the particular crystal growth process cannot be altered, then the crystal growth rate may be optimized to eliminate the vacancy-type region from the crystal (Fig. 7.6). The low growth rate shifts the v/G curve below the critical value ξ (see Fig. 5.1), the material becomes interstitial-type in full cross-section and oxygen precipitation is suppressed.

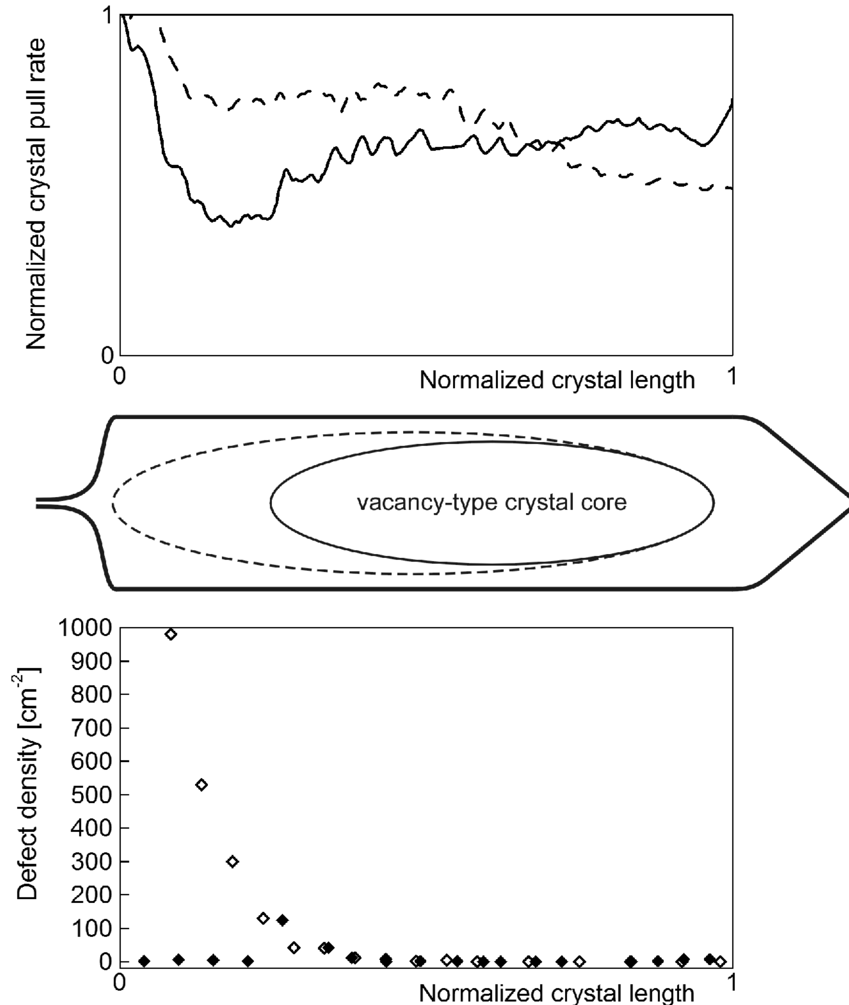

Figure 7.6: An example of defect engineering through v/G control. The axial profile of the crystal pull rate (top), the distribution of point defects (middle), and the corresponding defect density (bottom) of the original (dashed lines, open symbols) and optimized (solid lines, solid symbols) crystal growth process.

8. Crystal growth simulations in FEMAG

As mentioned in section 6.9, computer simulations of crystal growth are extremely useful tool for development and optimization of crystal growth as well as prediction and control of crystal defects. ON Semiconductor CR uses a commercial software FEMAG [173, 174] dedicated for simulations of the Czochralski crystal growth.

FEMAG is a code based on finite element method, which provides simulation of the temperature field in the puller, i.e. in the components of the hot zone, gas ambience, silicon melt, and the growing crystal. The global model takes into account heat transfer by radiation, conduction and convection, and considers mutual heat exchange between all components of the system. Simulation of the temperature and convective fields are coupled. The model uses axially symmetric approximation of the problem. Example of the model geometry and computed results is shown in Fig. 8.1.

FEMAG provides several modes of simulation. Quasi-steady simulation models one point in the growth process, i.e. picture of the process at given crystal length and fixed process parameters. The system, however, never really stays in such stationary state — the geometry as well as process parameters continuously vary during the whole growth. Nevertheless, changes of these parameters can be neglected in first approximation, because their time scale is much larger compared to the typical time scale of heat transfer, convection and diffusion in the system. The temperature and the velocity fields are assumed to be stationary, but evolution of the crystallization heat on the phase interface is considered in proportion to the pull rate. This approximation is fast and easy to perform, but is applicable only to the stage of the growth of the cylindrical portion of the crystal (the body).

During the other growth stages, changes of the geometry and process parameters cannot be neglected and time-dependent simulation has to be used. Time-dependent simulation starts from the quasi-steady simulation as the initial condition. The equations describing the system now

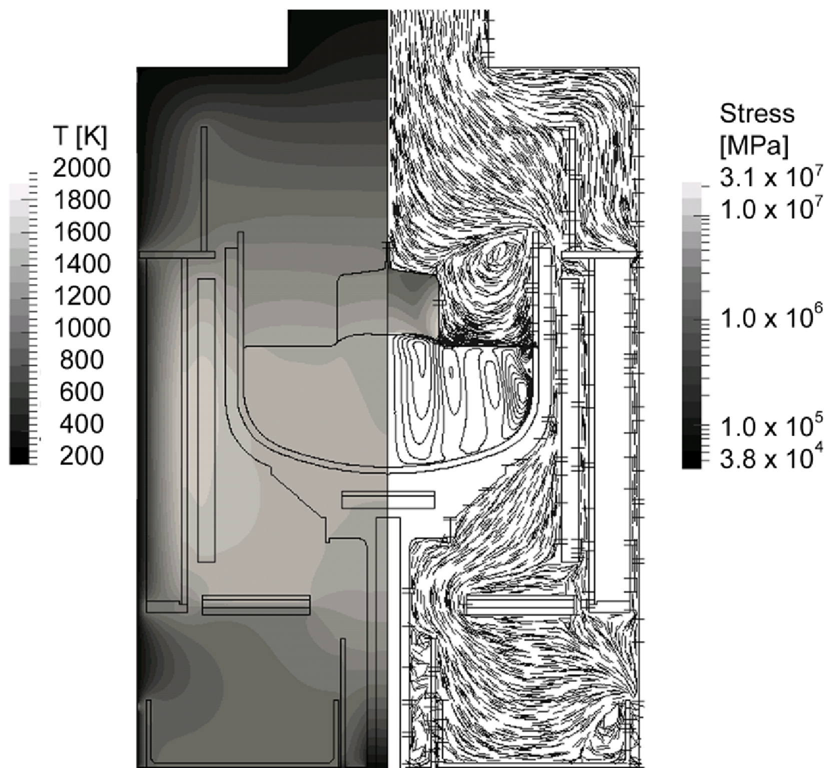

Figure 8.1: Left panel: Modeled temperature field in the puller and growing crystal. Right panel: Modeled argon flow, melt flow, and stress in the crystal.

include time derivatives, the geometry and process parameters are changed during the simulation. The crystallization heat is calculated from the evolution of the melt-crystal interface shape; hence the pull rate and the growth rate are distinguished. Time-dependent simulations are used for transient stages as the crown growth or the tail growth, but also for simulation of the body growth, when the process history is important.

The simulation can be performed in so called direct mode, when heater power and pull rate are prescribed and crystal diameter is calculated. More frequently, inverse mode is utilized, when crystal diameter and pull rate are prescribed, and heater power is calculated. The problem is then determined by melting temperature prescribed on the tri-junction point (crystal-melt-gas) and by the boundary condition, which is the temperature of the water-cooled puller shell.

We use the quasi-steady simulation in inverse mode for most of our simulations; simulations of several points of the process (at various crystal lengths) are used to capture the dependences on position in the crystal. Temperature gradient on the melt-crystal interface is used for construction of the $v/G(r)$ curves, which are utilized for simulation of the V-I boundary.

9. Study of crystal defects in heavily boron-doped silicon

Specifications of some types of polished silicon wafers include a requirement for maximal allowed surface density of OISF. In such case, monitoring wafers are sampled from the whole crystal; these wafers pass OISF test and OISF density is checked. The 150 mm heavily boron-doped wafers produced in ON Semiconductor CR are the typical representatives of products with such specifications. Heavy doping corresponds roughly to the level of above 10^{17} cm^{-3} atoms of boron in silicon.

Evaluation of OISFs on these products revealed unacceptably high OISF density in the seed-end portion of the crystals. These crystal portions cannot be used for production of silicon wafers with specified OISF density. In case this material fulfills specification of other required product, it is utilized for its manufacturing; otherwise it is scrapped. The resulting financial and capacity losses drove the requirement to solve the problem. In order to control the OISF density effectively one has to understand the mechanisms of their formation.

9.1. Experimental

Single crystals of silicon of 6" diameter, (111) oriented, boron-doped were grown by the Czochralski method in ON Semiconductor CR from a standard 16"hot zone and 35 kg polysilicon charge. The cylindrical part of the crystal of total length of about 620 mm was cut into several peaces (usually 3–4). Thick wafers (2–3 mm), so called slugs, were sliced from the faces of the crystal parts for measurement of oxygen concentration and resistivity. Resistivity was measured by the four-point-probe and the measured values were converted into volume concentration of boron in silicon according to the ASTM standard [175]. Oxygen concentration in heavily doped crystals was measured by secondary ion mass spectroscopy (SIMS). FTIR was used to measure oxygen concentration in lightly doped crystals grown by the same process as the heavily doped crystals (recipe, hot zone). Oxygen concentration in the heavily doped crystals was assumed to be the same as in the lightly doped ones (this was verified earlier on different boron-doped products). The conversion factor of 4.815×10^{17} cm^2 after ASTM 1979 [77] was used ("old ASTM"). Boron concentration in the studied crystals was 9×10^{14}–5×10^{19} cm^{-3} (resistivity 15–0.002 Ω cm); oxygen concentration was in the range of 25–35 ppma. The crystals were processed into single-side polished silicon wafers of diameter of 150 mm and thickness of 625 μm.

Crystal defects in the wafers were analyzed by OISF test, COP test and X-ray section topography. OISF test was performed by oxidation of polished wafers in wet atmosphere at 1150 °C for 3 h. Silicon oxide grown during the OISF test was stripped by hydrofluoric acid (42%, 5 min) and the wafer was selectively etched by Yang etchant [131] for 1 min. Part of the wafers was annealed prior to the OISF test in a non-oxidizing ambient (N_2:O_2 in ratio 20:1) at 1050 °C for 10 h. OISF distribution across the wafer surface was observed by naked eye under collimated light and by optical microscope. Radial profile of OISF surface density was constructed by counting of OISF along wafer diameter in two perpendicular directions; OISF density was averaged from these two measurements. COP test was performed by wafer etching in SC1 solution (NH_4OH:H_2O_2:H_2O in ratio 1:1:5) at 70–80 °C for 4 h. COP distribution was analyzed using the particle counter KLA Tencor Sufscan 6220. X-ray section topographs were taken with JEOL JMX-8H micro-focus X-ray diffractometer in Laue geometry using Ag $K_{\alpha1}$ radiation and $\langle 440\rangle$ diffraction. Bulk defects were observed on digitalized pictures.

9.2. OISF on heavily boron-doped wafers

The status of the problem at the beginning of my work was as follows. The seed-end portions of the heavily boron-doped crystals could not be utilized for manufacturing of polished wafers because of the very high counts of OISFs. This portion was the first 150 mm out of total 600 mm of the crystal length. The rest of the crystal was sampled and OISF density was checked to verify that the OISF specification is met. Some of the tested wafers were completely OISF-free; some contained certain amount of OISF. Circular pattern of OISFs could be recognized on some of the wafers. The pattern was either a circle or a circle with an extra outer ring (Fig. 9.1). It was believed that the OISF patterns have some relation to the OISF ring described in the literature but their origin remained unclear due to a different shape compared to the OISF ring (compare Fig. 9.1 and Fig. 5.3). An example of observed OISF pattern is shown in Fig. 9.2.

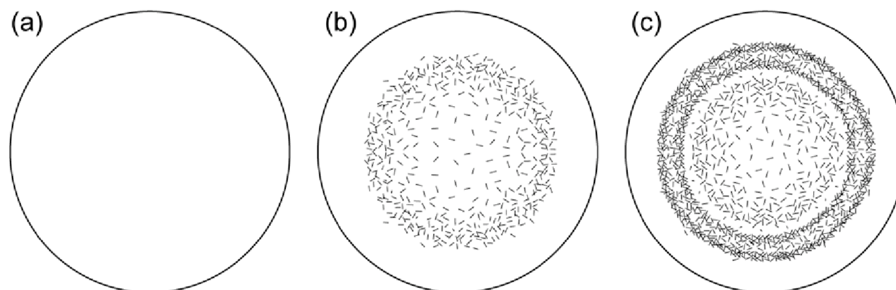

Figure 9.1: OISF distribution observed on the surface of 150 mm heavily boron-doped silicon wafers.(a) Clean wafer, (b) circular OISF pattern, (c) circular OISF pattern with an extra outer ring.

Figure 9.2: A photograph of an OISF pattern observed on the studied heavily boron-doped wafers. This pattern is schematically shown in Fig. 9.1c. The darker and lighter picture areas are photographing artifacts.

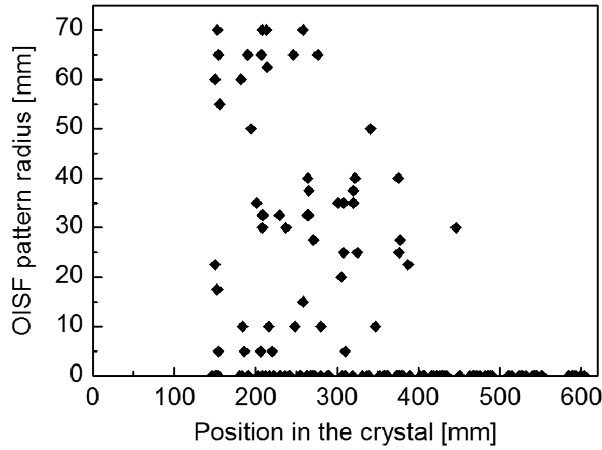

Figure 9.3: Radius of the OISF patterns observed on the surface of 150 mm heavily boron-doped silicon wafers. Zero values represent the case when OISF pattern was not observed. The first 150 mm of the crystal were not sampled for OISF monitoring as this crystal portion was not used for production of wafers.

Radius of the observed OISF patterns was varied among the measured wafers. Fig. 9.3 shows the radii of the observed patterns as the function of position of the wafer in the crystal. Data for the first 150 mm were missing as this material was not used for production and, hence, was not sampled.

9.3. Dependence of OISF distribution on doping level and position in the crystal

The processes of defect formation are driven by the evolution of the temperature field in the crystal, which changes slowly during the many hours of the process. The effect of fluctuations of the pull rate related to crystal diameter control is averaged on the time scale of defect formation processes. It can be therefore expected that the changes in distribution of defects along the crystal are also continuous and relatively slow. The radii of the OISF pattern should therefore change continually and should not form a set of random data.

In order to find possible rules in the crowd of data points in Fig. 9.3 the data were first filtered to remove outlayers. Then, the resistivity of the wafer was found out for each data point. After reprinting the filtered data differentiated according to the doping level (Fig. 9.4a) the apparent dependence of the OISF pattern radius on resistivity is revealed. This dependence is clearly shown in Fig. 9.4b. It is also clear from Fig. 9.4a that there is a dependence of the OISF pattern radius on the position in the crystal. The radial distribution of OISF and its dependence on boron concentration and position in the crystal suggest possible relation to V-I boundary (see Chapter 5).

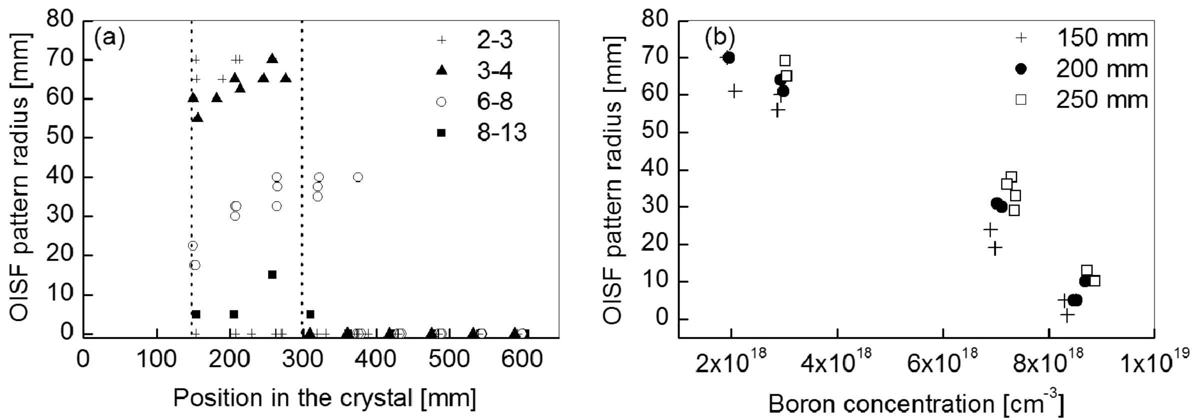

Figure 9.4: (a) Reprint of Fig. 9.3 after data filtering and differentiation according to the resistivity. Legend shows boron concentration in the crystals in [$\times 10^{18}$ cm^{-3}]. Each resistivity range contains data from various crystals grown by the same process with the same amount of dopant introduced into the melt. Zero values represent cases when the radius of the pattern could not be determined due to low OISF density or the wafer was OISF-free. The dotted vertical lines at 150 and 300 mm highlight the range to be compared to Fig. 9.5. (b) Radius of the OISF pattern as the function of boron concentration for three positions in the crystals. Legend shows the distance from the seed end.

9.4. Simulation of the V-I boundary

In order to analyze the possible relation of the OISF pattern to the V-I boundary, information on the V-I boundary must be acquired. We performed computer simulations of the crystal growth process to model the temperature field in the growing crystal. Process simulations were performed for several stages of crystal growth corresponding to the crystal length of 50, 100, 150, ... 500 mm (full crystal length is about 620 mm). The simulations yield a radial profile $G(r)$ of the axial temperature gradient G for the various growth stages. Using the known values of the crystal pull rate v for each growth stage it was possible to construct a map of the v/G parameter over the whole crystal. The function $v/G(r, l)$, where l is distance from the crystal seed-end is shown in Fig. 9.5.

Let us suppose that the critical value v/G_{crit} is constant along the crystal. This assumption is valid for the lightly doped crystals where the dependence on boron concentration is weak [112, 114]. In such case the isolines of $v/G(r, l)$ drawn in Fig. 9.5 correspond to the position of the V-I boundary in the crystal for labeled values of the v/G_{crit}. Comparing the region of axial position of 150–300 mm in Fig. 9.5 and Fig. 9.4a, one can recognize the similarity of the observed radius of the OISF pattern with the modeled radius of the V-I boundary. Radius of the OISF pattern for the boron doping of 2–3, 3–4 and 6–8 $\times 10^{18}$ cm^{-3} increases from the value at 150 mm to the value at 300 mm similarly to the V-I boundary corresponding to the v/G_{crit} values of 0.17, 0.19 and 0.21 mm^2/min K. We will therefore assume that the observed distribution of OISF has a relation to the V-I boundary and we will apply the theory of V-I boundary and v/G parameter to describe the observed OISF pattern. We will temporarily suppose that the V-I boundary lies very close to the outer perimeter of the OISF pattern similarly to the OISF ring.

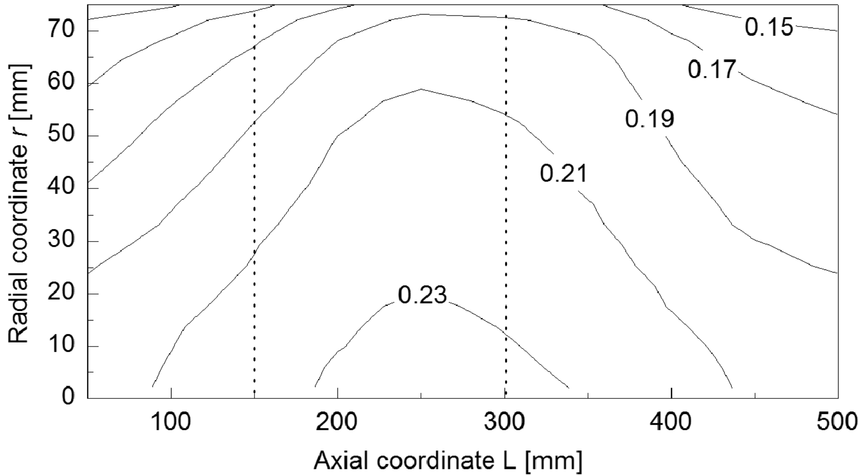

Figure 9.5: Map of the v/G parameter over the crystal constructed using computer simulations of crystal growth. The isolines are labeled with the corresponding value of v/G in [mm^2/min K]. The dotted vertical lines at 150 and 300 mm highlight the range to be compared to Fig. 9.4

9.5. Estimation of the critical value v/G

Supposing that the V-I boundary lies very close to the outer perimeter of the OISF pattern (with radius r_{OISF}), equation $v/G(r_{OISF}) = v/G_{crit}$ holds. Comparison of the region of 150–300 mm in Fig. 9.4a and Fig. 9.5 shows that the values of $v/G(r_{OISF})$ would indeed be quite close to the modeled isolines of v/G_{crit}. As the radius of the OISF pattern depends on the boron concentration (see Fig. 9.4b), the v/G_{crit} is also the function of boron concentration.

No OISF pattern was found on the lightly boron-doped wafers up to the boron concentration of 1.7×10^{18} cm^{-3}. It can be concluded that the lightly doped crystals are fully vacancy-rich. The critical value for the lightly doped crystals must be therefore lower than the lowest value of the calculated v/G map shown in Fig. 9.5 which is about 0.13 mm^2/min K (values in the uppermost left and right corners of the map). The OISF patterns were observed on wafers with boron concentration higher than 1.7×10^{18} cm^{-3} and disappeared when boron concentration exceeded 1.3×10^{19} cm^{-3}. It can be concluded that these most heavily doped crystals are fully interstitial-rich. The critical value for the most heavily doped crystals must be therefore higher than the highest value of the v/G map, which is 0.24 mm^2/min K (value at about 250 mm at $r = 0$ mm).

Published values of the critical v/G value for undoped and lightly boron-doped silicon range from 0.12 to 0.14 mm^2/min K [43, 112–114, 176]. We have chosen the value 0.13 mm^2/min K which agrees to the published values as well as to the conclusion above. The values of the OISF pattern radii from Fig. 9.4a measured at the positions in the crystal of 150–300 mm were interpolated to obtain the radii of the OISF pattern (r_{OISF}) for the positions of 150, 200 and 250 mm. Analogically, boron concentration C_B in the wafers corresponding to these radii was calculated. Using the condition $v/G(r_{OISF}) = v/G_{crit}$ the critical values v/G_{crit} were determined from the modeled $v/G(r)$ curves (these curves served for construction of the v/G map in Fig. 9.5). Assigning the values of boron concentration C_B corresponding to r_{OISF} to the critical values, the function $v/G_{crit}(C_B)$ was obtained. The $v/G_{crit}(C_B)$ values are plotted in Fig. 9.6. The best fit of the data was obtained using a logarithmical function

$$v/G_{crit} = a + b \cdot ln(C_B + c), \tag{9.1}$$

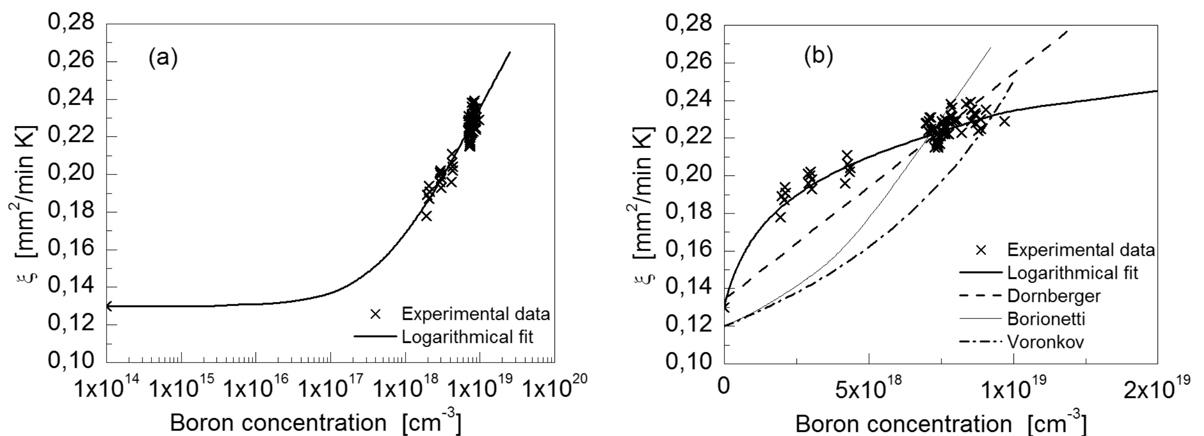

Figure 9.6: Critical value of v/G estimated from the OISF pattern radii as the function of boron concentration in (a) logarithmic and (b) linear representation concentration. The $v/G_{crit} =$ 0.13 mm^2/min K is the estimate for undoped/lightly doped silicon. The data are approximated by the best fit according to Eq. 9.1. Panel (b) shows also published data by Dornberger [112], Borionetti [114] and Voronkov [178] for comparison.

with a $= -1.25 \pm 0.1$ mm^2/min K, b $= -0.034 \pm 0.002$ mm^2/min K, and c $= 4.8\times10^{17} \pm 1\times10^{17}$ cm^{-3}. This empirical dependence is also shown in Fig. 9.6. The $v/G_{crit}(C_B)$ curves reported by various authors (see Fig. 9.6b) differ rather significantly. We suppose that the differences are caused by the insufficient precision of the used thermal models which provide the $G(r)$ functions.

Our results indicate that boron up to the concentration of about 10^{17} cm^{-3} does not influence the critical v/G value and, hence, does not influence distribution of defects in silicon crystals.

9.6. Comparison of V-I boundary simulations with OISF distribution

The process of growing heavily boron-doped crystals in ON Semiconductor has several variations varying by the amount of boron introduced into the melt. Each process results in a typical concentration of boron in the grown crystals. Due to segregation, boron concentration increases from the seed-end to the tail-end of the crystal. The individual growth processes therefore yield crystals of certain concentration range. The individual growth processes will be hereafter represented by the concentration range of the grown crystals (seed-end to tail-end). This representation has been already used in Fig. 9.4a.

Using the known resistivity axial profiles and the empirically determined function $v/G_{crit}(C_B)$ the dependence of v/G_{crit} on the position in the crystal was determined for the growth processes displayed in Fig. 9.4a. Comparison with the map of v/G (Fig. 9.5) yields the V-I boundary radius (r_{V-I}) as the function of position in the crystal (utilizing the condition $v/G(r_{V-I}) = v/G_{crit}$). The modeled V-I boundaries are plotted in Fig. 9.7 together with the radii of the observed OISF patterns.

In the range of position in the crystal of about 150–300 mm, we can identify a reasonable qualitative agreement of the modeled V-I boundary radius and the measured radius of the OISF pattern. We can expect that the radius of the OISF pattern follows the V-I boundary in the beginning of the crystal were no measured data are available. The question to solve is an obvious disagreement of the V-I boundary and the OISF pattern in the second half of the crystal for boron doping below about 6×10^{18} cm^{-3}. The predicted V-I boundary radius steadily decreases from its maximum at around 300 mm while the OISF pattern abruptly and completely disappears (this is represented by zero values).

The doping level of 4–6×10^{18} cm^{-3} was chosen as the suitable material for further tests. Wafers from this crystal were sampled throughout the whole crystal length and the OISF pattern was delineated. We observed that the radius of the OISF pattern steadily increases from the seed end to about 300 mm (Fig. 9.8) where the pattern disappeared and no OISF were found on the wafer surface. The test proved that the radius of the OISF pattern in the first half of the crystal qualitatively follows the modeled V-I boundary.

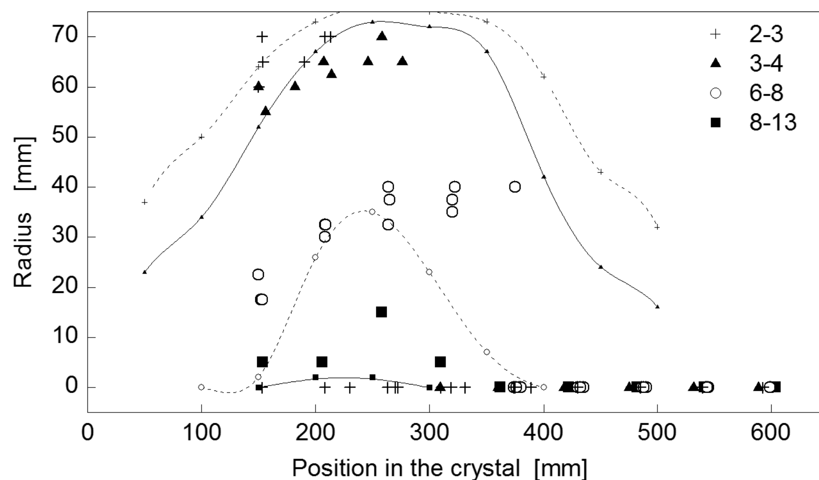

Figure 9.7: Measured radius of the observed OISF pattern (scattered data) and radius of the modeled V-I boundary (lines with small symbols corresponding to the doping level). The V-I boundary was modeled using the v/G map and the $v/G_{crit}(C_B)$ function for several levels of boron doping. Legend shows boron concentration in the crystal in $[10^{18}$ cm$^{-3}]$ (seed-end–tail-end).

Although there are some uncertainties, the above described work shows that the OISF pattern can be qualitatively described by the v/G methodology using computer simulations of crystal growth and the empirically determined function $v/G_{crit}(C_B)$. The discontinuity of the radius of the OISF pattern around 150 mm observed in the case of the test crystal doped to 4–6×10^{18} cm^{-3} and disappearance of the OISF pattern in the second half of all the crystals will be discussed later in section 9.11.

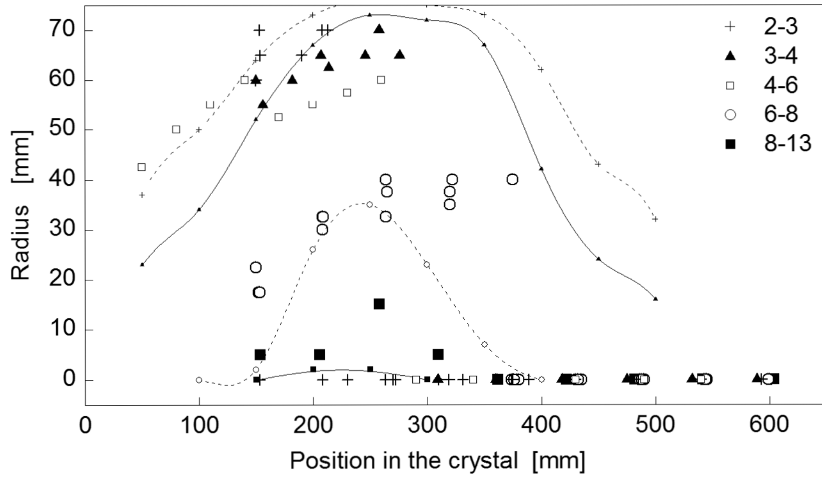

Figure 9.8: Reprint of Fig. 9.7 with added radius of the OISF pattern observed on a test crystal doped to 4–6×10^{18} cm^{-3} (empty squares).

9.7. Radial OISF distribution

Key understanding of the observed OISF patterns was revealed by detailed analyses of the wafers from the test crystal doped to 4–6×10^{18} cm^{-3}. OISF on the wafer surface formed circular patterns whose shape varied with the position in the crystal.

Wafers from the first quarter of the crystal (0–150 mm) show the OISF pattern consisting of the central circle and an outer ring of high OISF density which are separated by a ring of very low OISF density. Essentially no OISF were found outside the outer ring. The pattern is shown in Fig. 9.9a. The OISF density inside the central circle decreases from the rim to the center. Surface density of OISF was measured using the optical microscope. Fig. 9.9c shows the radial profile corresponding to Fig. 9.9a. Both Fig. 9.9a and Fig. 9.9c show that on some wafers it was possible to distinguish a fine substructure of the outer ring of OISF which was formed by two narrow rings of very high OISF density separated by a ring of slightly lower OISF density. Example of such wafer is shown in Fig. 9.2.

Wafers from the second quarter of the crystal (150–300 mm) show the OISF pattern formed only by the central circle (Fig. 9.9b). The OISF density inside the circle decreases from the rim to the center similarly to the inner circle found on the wafers from the first quarter of the crystal. OISF density outside the circle is essentially zero.

The OISF density observed on the wafers from the test crystal doped to 4–6×10^{18} cm^{-3} generally decreases with the distance from the crystal seed-end. The OISF pattern so becomes less and less sharp, the radius becomes less and less measurable and finally no OISF are found on the wafers in the second half of the crystal.

Fig. 9.9e shows the radii of the measurable OISF patterns. The plot shows radius r_1 of the outer ring and radius r_2 of the inner circle found on the wafers from the first crystal quarter and radius r_3 of the circle observed on the wafers from the second quarter of the crystal. The radii are plotted as the function of distance from the seed-end (denoted as L). It is apparent that the $r_3(L)$ curve is the follow-up of the $r_2(L)$ curve. As the circles of OISF corresponding

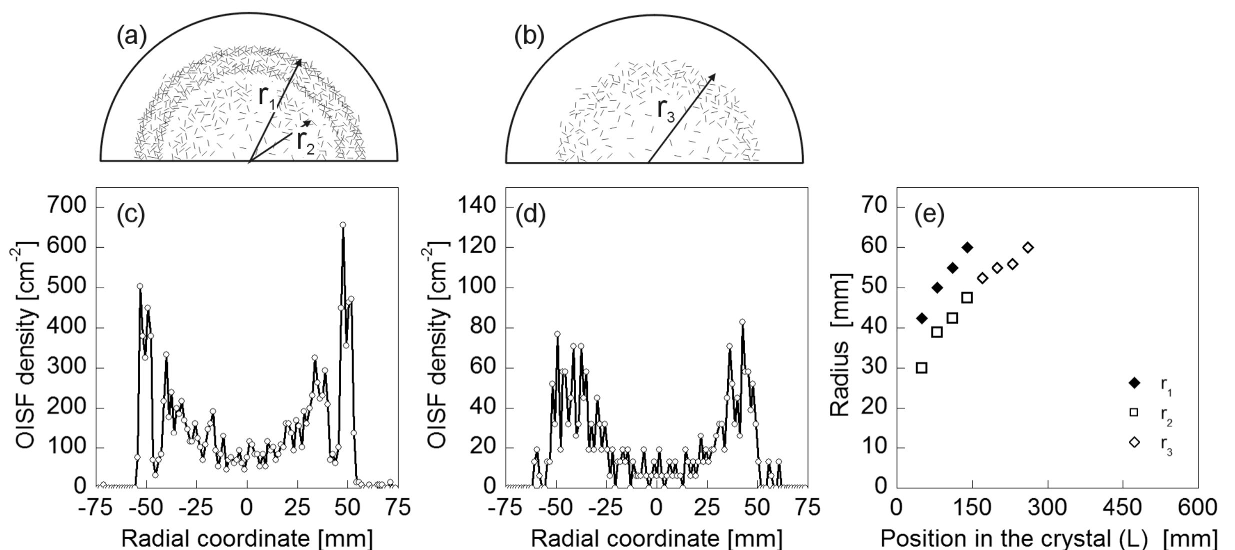

Figure 9.9: Scheme of the OISF pattern observed on the wafers from (a) the first and (b) the second quarter of the crystal (only half of the wafer is shown). Panels (c) and (d) show radial profiles of the surface density of OISF observed on the wafers represented by panels (a) and (b), respectively. Note different scales on the y-axis demonstrating the decrease in OISF density along the crystal. Panel (e) shows the radius of the features forming the OISF pattern. Labeling r_1,r_2,r_3 corresponds to panels (a) and (b).

to r_2 and r_3 show also similar radial dependence of OISF density, it opens that it is a case of the same feature.

Considering the above discussed results we can formulate a hypothesis that the OISF pattern observed in the first quarter of the crystal is the complete pattern, which would appear throughout the whole crystal under optimal circumstances. However, due to decreasing OISF density, the pattern gradually disappears with increasing distance from the crystal seed-end. The outer ring disappears first, the inner circle follows. This scenario is supported by the trace of the outer ring captured at the radius of about 60 mm in Fig. 9.9d, which was not distinguishable by eye on the wafer (as sketched in Fig. 9.9b). The reason for decrease in the OISF density with the distance from the seed end is to be resolved (see section 9.11).

9.8. Relation of OISF to bulk crystal defects

It is known that the OISF ring is formed by nucleation of the stacking faults on oxide precipitates. It is therefore likely that the observed OISF pattern also delineates oxide precipitates in the wafer. Distribution of the oxide precipitates in the bulk of the wafers was studied by the X-ray section topography.

Fig. 9.10a shows the X-ray section topogram of the region of the outer ring of OISF found on the wafer from the first crystal quarter. Oxide precipitates are visible as black dots. The topogram clearly shows non-homogeneous distribution of oxide precipitates depending on the radial position on the wafer. Radial profile of the precipitate density is plotted in Fig. 9.10b together with the radial profile of the OISF density from Fig. 9.9c. Correlation of the two radial profiles is obvious — both curves show the highest values in the region of about 47–54 mm from the wafer center, lower values closer to wafer center and zero values closer to wafer rim.

It can be therefore concluded that the OISF forming the pattern on the surface of our heavily boron-doped wafers nucleate on oxide precipitates located in the near-surface region of the wafer. As the OISF test is the only thermal operation applied to the test wafers, the oxide precipitates certainly nucleated during the crystal growth (nucleation during the OISF test is negligible). These precipitates will be called the grown-in precipitates. Their ability to serve as the nuclei for OISF implies that their size after the crystal growth is larger than the critical radius at the temperature of the OISF test. In other words the OISF pattern is formed by nucleation of OISF on the grown-in oxide precipitates which are supercritical at the temperature of the OISF test.

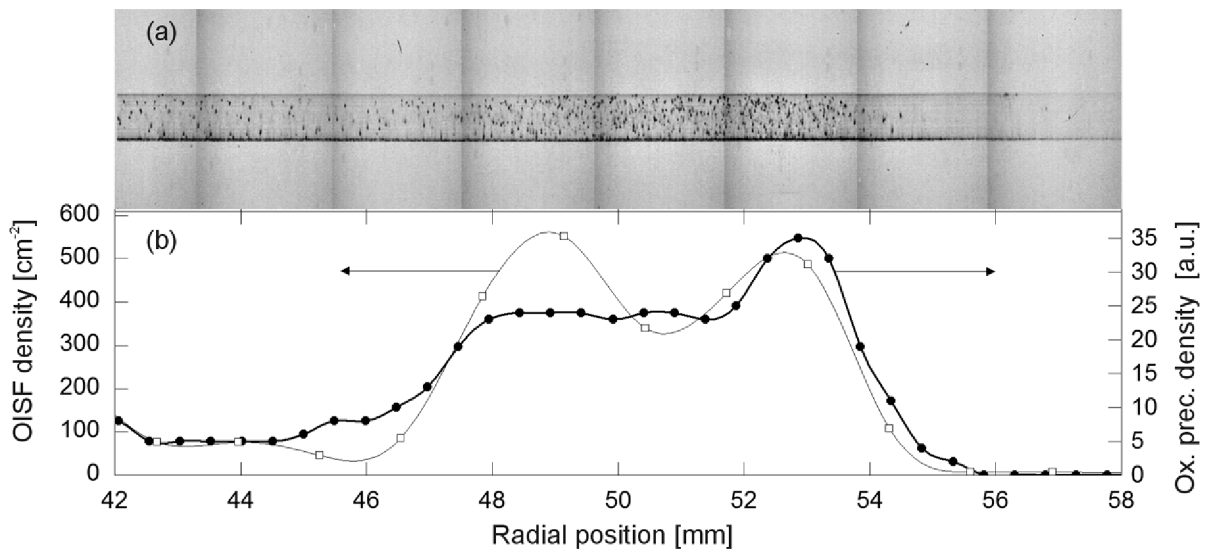

Figure 9.10: (a) X-ray section topogram of the wafer from the first crystal quarter after the OISF test. The topogram shows the region of the outer ring. Picture dimensions are not to scale. (b) Surface density of OISF from Fig. 9.9c (open symbols) and bulk density of oxide precipitates counted from the topogram (full symbols). The radial coordinate represents the distance from the wafer center.

9.9. Origin of the radial OISF pattern

It was explained above (section 5.1) that precipitation of oxygen is supported by the presence of vacancies in the material. According to the Voronkov theory, interactions of point defects during the crystal growth result in the radial profile of concentration of free vacancies showing a double-peak close to the V-I boundary (Fig. 5.2). This distribution of vacancies results in a typical radial distribution of oxide precipitates (Fig. 5.2d,f). Comparing Fig. 5.2e,f with Fig. 9.9c, one can recognize apparent similarity of the OISF profiles with the profile of residual vacancies and small oxide precipitates.

We will compare Fig. 9.9c with Fig. 5.2e which describes the typical distribution of crystal defects in lightly boron-doped silicon crystals. The similarity of the profiles allows us to identify the key features of the OISF pattern. The deduced relations are shown in Fig. 9.11. We believe that:

1. the outer rim of the OISF pattern coincides with the V-I boundary; the interior is the vacancy-rich core and the exterior is the interstitial-rich region;
2. the outer ring of very high OISF density coincides with the L-band;
3. the region of the highest OISF density in the central circle (close to its outer rim) coincides with the H-band;
4. the ring of low OISF density separating the L- and H- bands corresponds to the P-band.

Let us remind that we showed in the previous section that the OISF observed on the surface of our wafers reflect the distribution of grown-in oxide precipitates supercritical at the temperature of the OISF test, which was 1150 °C in this case. The above stated conclusions mean that

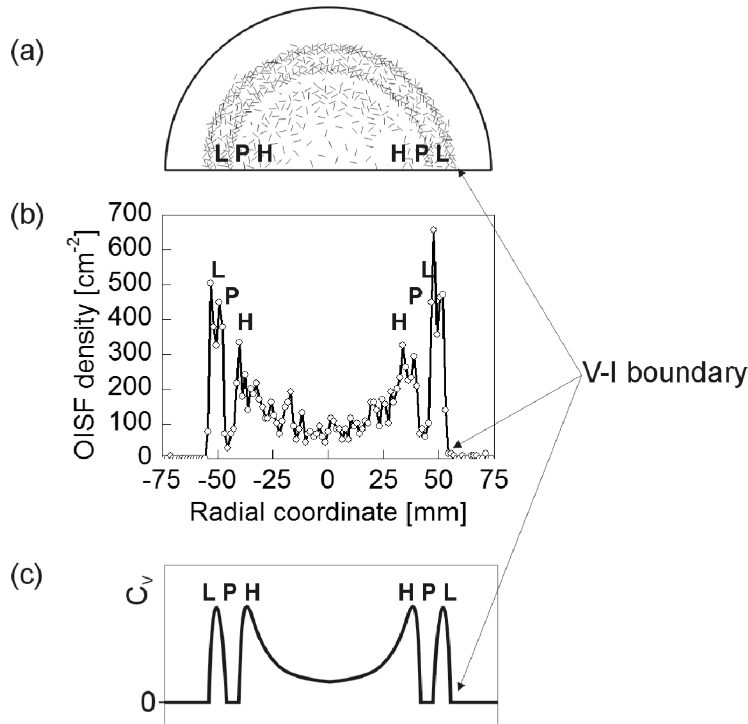

Figure 9.11: The figure demonstrates the relation of the OISF pattern to the microdefect bands and V-I boundary. (a) Typical distribution of OISF on the surface of wafers from the first quarter of the heavily boron-doped crystals. (b) Radial profile of the OISF surface density corresponding to the wafer from panel (a). (c) Schematic representation of the radial profile of concentration of free vacancies (or small oxide precipitates) established typically in lightly boron-doped silicon crystal. Microdefect bands and the V-I boundary are labeled in the picture.

the oxide precipitates formed in the L- and H- bands during the crystal growth are larger than the critical radius at 1150 °C which is a very unusual phenomenon. It was described in sections 5.3 and 5.5 that the L- and H- bands typically contain small grown-in precipitates, and OISF are formed only in the P-band. We see seemingly inverse behavior when OISF are formed in the L- and H- bands in higher density than in the P-band. However, as the OISF density in the P-band is nonzero (see Fig. 9.9c), the observed phenomenon is rather an addition of strong oxygen precipitation in the L- and H- bands superimposed over the usual OISF formation in the P-band.

9.10. Verification of the V-I boundary

The vacancy-rich core of the crystal is characterized by the presence of the vacancy-type defects — voids and COPs. The outer boundary of the COP-containing region is found close to the V-I boundary, usually it is located in the P-band [108, 111] as shown in Fig. 5.2b. The COP test can be therefore used for delineation of the V-I boundary, more specifically of the OISF ring. A nice experimental evidence of this relation was shown also in [179] (see Fig. 9.12a).

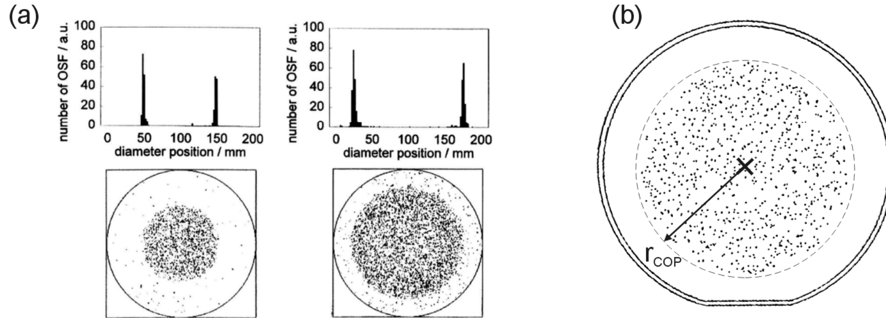

Figure 9.12: (a) Comparison of the position of the OISF ring and the COP containing area adopted from Suhren [179]. The classical OISF ring was observed on 200 mm wafers heavily doped with boron ($C_B \approx 4.6 \times 10^{18}$ cm^{-3}). (b) Example of the COP distribution on the surface of a polished silicon wafer after the COP test. The picture shows the wafer from the position in the crystal of 150 mm from the seed-end. The lower detection limit for the defect size is 130 nm. The dashed circle represents identification of the boundary of the COP region of the radius r_{COP}.

The COP test was performed on our wafers throughout the whole crystal. Fig. 9.12b shows one example of the COP map taken from the measured wafer. The COPs were clearly delineated in compact circles in the center of the wafers; rim of the wafers was COP-free. Radius of the COP region was measured from the COP maps as demonstrated in Fig. 9.12b.

Fig. 9.13 shows the radius of the COP-containing region found on the analyzed wafers together with the radii of the OSF pattern reprinted from Fig. 9.9e. Let us first explore the region of 0–150 mm. The radius of the COP region lies between the radii of the L- and H- bands determined from the OISF pattern. Hence, the radius of the COP region coincides with the estimated position of the P-band. This fact validates the correct identification of the bands and the V-I boundary.

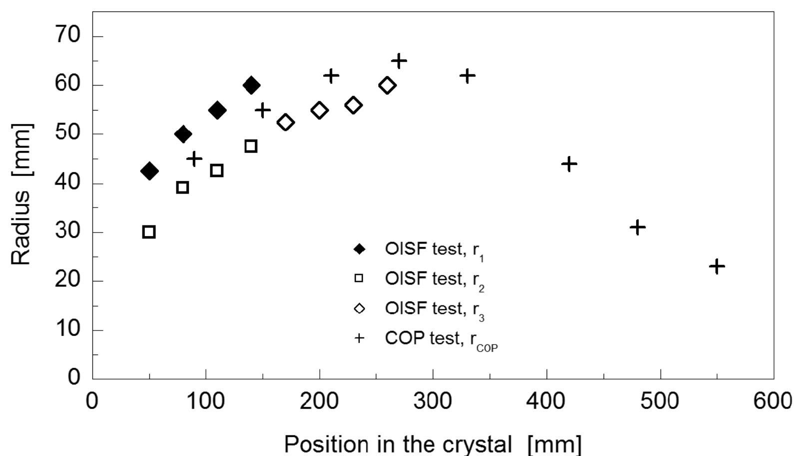

Figure 9.13: The radii of the features of the OISF pattern (labeled according to Fig. 9.9) and radius of the COP (r_{COP}) region as the function of position in the crystal.

9.11. Origin of the axial changes in the OISF pattern

The identification of the bands in the first crystal quarter as shown in Fig. 9.11 seems to be very consistent. As the P-band delineated by the COP test was found throughout the whole crystal (see Fig. 9.13), we expect that also the V-I boundary and all the microdefect bands go through the whole crystal. This assumption is supported by observation of the H-band of the radius r_3 found in the second quarter of the crystal (150–300 mm).

However, if the L-, P- and H-bands go through the whole crystal, there is a question why they are not delineated by the OISF pattern. To deduce the reason we will now analyze the mechanism of OISF formation.

It was shown (section 9.8) that OISF observed on the surface of the wafer nucleate on oxide precipitates located near the surface. In general, oxide precipitates smaller than the critical radius at the temperature of the OISF test quickly dissolve during the temperature ramp-up or early after the temperature is achieved and can not serve as the nuclei for OISF growth.

Let us suppose that the size of the grown-in oxide precipitates is not homogeneous throughout the crystal and that it decreases from the crystal seed-end to the tail-end. We can imagine that the distribution curve of precipitate size shifts to lower values with increasing distance from the seed-end. This situation is schematically demonstrated in Fig. 9.14. With increasing distance from the seed-end larger portion of the distribution curves falls below the critical radius corresponding to the temperature of the OISF test. Simultaneously, larger portion of the precipitates becomes undercritical and dissolves. The OISF density therefore decreases and finally no OISF are formed on the surface because all oxide precipitates are dissolved.

Indeed, this proposed scenario corresponds to the observed behavior of the OISF pattern. As the L-band vanishes earlier than the H-band, it is likely that the grown-in oxide precipitates in the H-band are larger compared to those in the L-band.

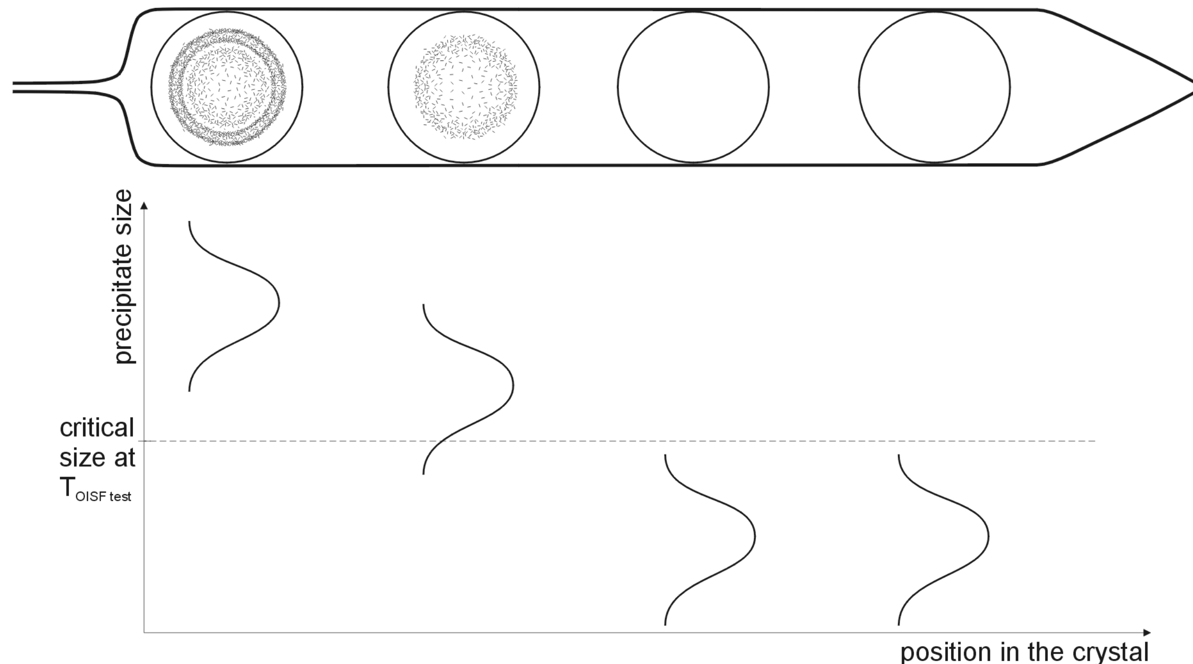

Figure 9.14: Top: Illustration of the OISF pattern observed in various positions in the crystal. Bottom: Proposed distribution curves of the size of the grown-in oxide precipitates corresponding to various positions in the crystal and their relation to the critical radius at the temperature of the OISF test.

9.12. OISF test with pre-annealing

We designed a test to verify the mechanism of axial disappearance of the OISF pattern proposed in Section 9.11. A set of wafers was annealed prior the OISF test at 1050°C for 16 h. The annealing temperature was chosen to be above the typical range for nucleation of new oxide precipitates (which is about 500–900 °C) and below the typical temperature of the OISF test (which is usually 1100–1150 °C). The grown-in oxide precipitates were therefore allowed to grow while no new precipitates should be nucleated.

Indeed, we observed formation of OISF on the wafers from the whole crystal. Radius of the OISF region observed during this test is plotted in Fig. 9.15. It is shown that this radius coincides with the outer radius of the L-band in the first crystal quarter (OISF test r_1, i.e. the V-I boundary) and follows the radius of the P-band delineated by the COP test throughout the whole crystal. It is obvious that the test revealed the V-I boundary in the whole crystal and verified the assumption on the varying size of grown-in oxide precipitates along the crystal. The results are finally consistent with the results of computer simulations which predict the V-I boundary in the whole crystal (see Section 9.4).

However, we have to note few peculiarities of the results. The banded structure was lost and only a full ring of OISF was observed throughout the crystal. As the outer diameter of the OISF region in the first crystal quarter coincides with the outer diameter of the L-band and therefore with the V-I boundary, it is obvious that OISF were formed in the whole vacancy-rich region. As the outer diameter of the full OISF region is larger than the COP region (and rather equidistantly spaced) throughout the whole crystal, we can conclude that OISF were formed in the vacancy-rich region in the whole crystal. Considering the applied pre-annealing this can be explained in a way that the grown-in oxide precipitates were supercritical at 1050°C in the whole vacancy-rich region throughout the whole crystal.

Another peculiarity was that the OISF ring in the first crystal quarter was difficult to resolve after pre-annealing. The reason was a large amount of smaller OISF (5–15 μm) and etch pits over the whole wafer surface. The OISF pattern itself was formed by large OISF (20–30 μm). Formation of etch pits and OISF over the whole wafer surface suggests that huge oxygen precipitation occurred even in the interstitial-rich region outside the OISF pattern where it is usually suppressed.

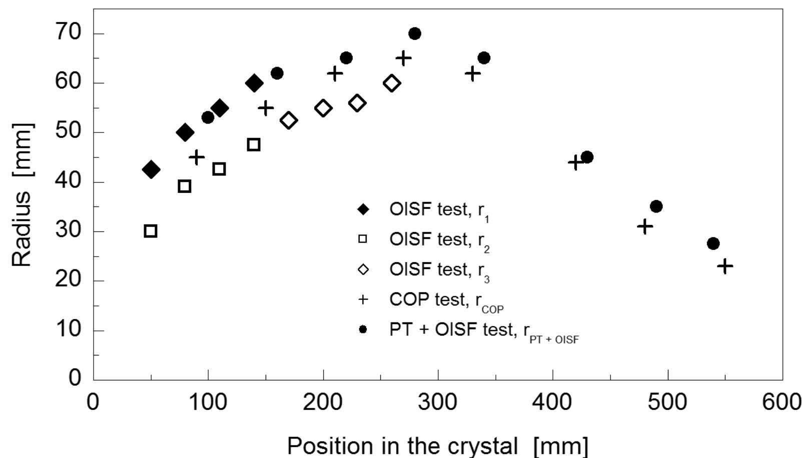

Figure 9.15: The radii of the features of the OISF pattern (labeled according to Fig. 9.9), radius of the COP region and outer radius of the OISF pattern observed after OISF test with pre-annealing ($r_{PT+OISF}$) as the function of position in the crystal.

Oxygen precipitation in both vacancy- and interstitial-type crystal was observed by Kim et al. [180]. Heavily boron-doped wafers of both interstitial-type and mixed-type were examined by heat treatment and OISF test. While BMD (Bulk Micro Defects), i.e., oxygen precipitates, of high density were observed both in the vacancy- and interstitial-type regions, OISF were observed in most cases only in the OISF ring region as in the case of the lightly doped silicon. However, after pre-annealing at 900 °C, OISF were formed over the entire wafer surface regardless of the wafer type. Unlike in our case, precipitates observed by Kim et al. were not stable enough at higher temperature. Above 1000 °C OISF were observed only in the OISF ring again.

Asayama et al. [181] also observed BMD formation over the entire wafer surface regardless of the defect region type. Similarly to Kim et al., the precipitates in the OISF ring showed the highest stability at high temperature. Both these results (a) partly agree and (b) partly disagree with our observations.

ad a) Agreement with our results: Kim and Asayama showed that high boron doping allows oxygen precipitation even in the interstitial-rich crystal region. Precipitates there, however, exhibit lower density and worse thermal stability (thus smaller size) compared to the vacancy-rich region. Grown-in precipitates in our crystals are certainly also smaller in the interstitial-rich region because after OISF test the OISF were observed only in the vacancy-rich region. Behavior of our wafers after pre-annealing is also in accordance with findings of Kim and Asayama. In the first crystal quarter we observed etch pits and OISF also in the interstitial-rich region. We suppose that the etch pits are delineated oxygen precipitates and that all OISF nucleate on oxygen precipitates. OISF in this region were smaller compared to the vacancy-rich region. This suggests that their growth started later because the grown-in precipitates were smaller than in the vacancy-rich region and it took more time to grow to the size large enough to serve as the OISF nuclei.

Oxygen precipitation in the interstitial-rich region can be explained as follows. The growth of an oxygen precipitate is accompanied by the emission of silicon self-interstitials. While supersaturation of oxygen is the driving force for precipitation, supersaturation of self-interstitials acts against precipitation [182]. It has been published that high boron concentration increases the equilibrium concentration of silicon self-interstitials [183], it decreases their supersaturation which in turn allows oxygen to precipitate. The first crystal quarter is characteristic by the highest oxygen concentration. We suppose that lower oxygen content in the rest of the crystal causes lower supersaturation which cannot compete with high supersaturation of self-interstitials. Therefore, precipitation in the interstitial-rich region in the rest of the crystal is not allowed and OISF are not observed even after pre-annealing.

ad b) Disagreement with our results: In most cases reported by Kim the OISF were observed solely in the OISF ring and only pre-annealing at 900 °C led to OISF formation over the entire wafer surface. In the first half of the crystal we observed OISF formation generally in the whole vacancy-rich crystal region excluding the OISF ring (P-band). The OISF over the entire surface were observed after pre-annealing at 1050 °C in the first crystal quarter. Kim's wafers were doped at the same level as our wafers and they were also of the mixed type. A different behavior of the grown-in defects should be thus caused by some other parameters. We conclude these are the crystal thermal history and the oxygen content. Since no information on the thermal history was published by Kim, this parameter cannot be discussed. The oxygen concentration in the first quarter of our crystals was in the range of 30—35 ppma, while Kim reported the content of 25.5–27.5 ppma. A higher oxygen concentration is likely the root cause of the larger size of the grown-in precipitates, which enhances their stability at higher temperature.

Despite some peculiarities of the results the OISF test after pre-annealing verified our conclusions on the size distribution of the grown-in oxygen precipitate which results in changing appearance of the OISF pattern along the crystal.

9.13. Origin of the axial variations in the size of grown-in oxide precipitates

In the former text we came to the conclusion that the size of the grown-in oxide precipitates in the studied crystals decreases from the seed-end to the tail-end. This size distribution results in gradual disappearance of the OISF pattern. In order to support this hypothesis we have to explain the variation of precipitate size throughout the crystal.

It is well known that the key factors controlling oxygen precipitation in the grown crystal are concentration of oxygen and time evolution of temperature, so called thermal history [87,93], [182,184–186]. The window for effective precipitation of oxygen is bound by the temperature when appreciable supersaturation is achieved from the top, and by the temperature when oxygen diffusion is negligible from the bottom. Fig. 9.16b shows oxygen concentration typical for the studied crystals, Fig. 9.16a reminds the OISF pattern and Fig. 9.16c shows the modeled thermal history.

Considering the first three quarters of the crystal it is seen that oxygen concentration decreases while the thermal history is comparable down to about 650 °C. This temperature is almost the lower limit for appreciable nucleation of oxide precipitates [93]. The lower boundary of the nucleation window is similar for the whole considered portion of the crystal as the dependence of the nucleation rate on oxygen concentration at the temperature around 650 °C is weak [93]. The upper boundary of the nucleation window is determined by oxygen concentration. As the oxygen content decreases the temperature of supersaturation shifts to lower

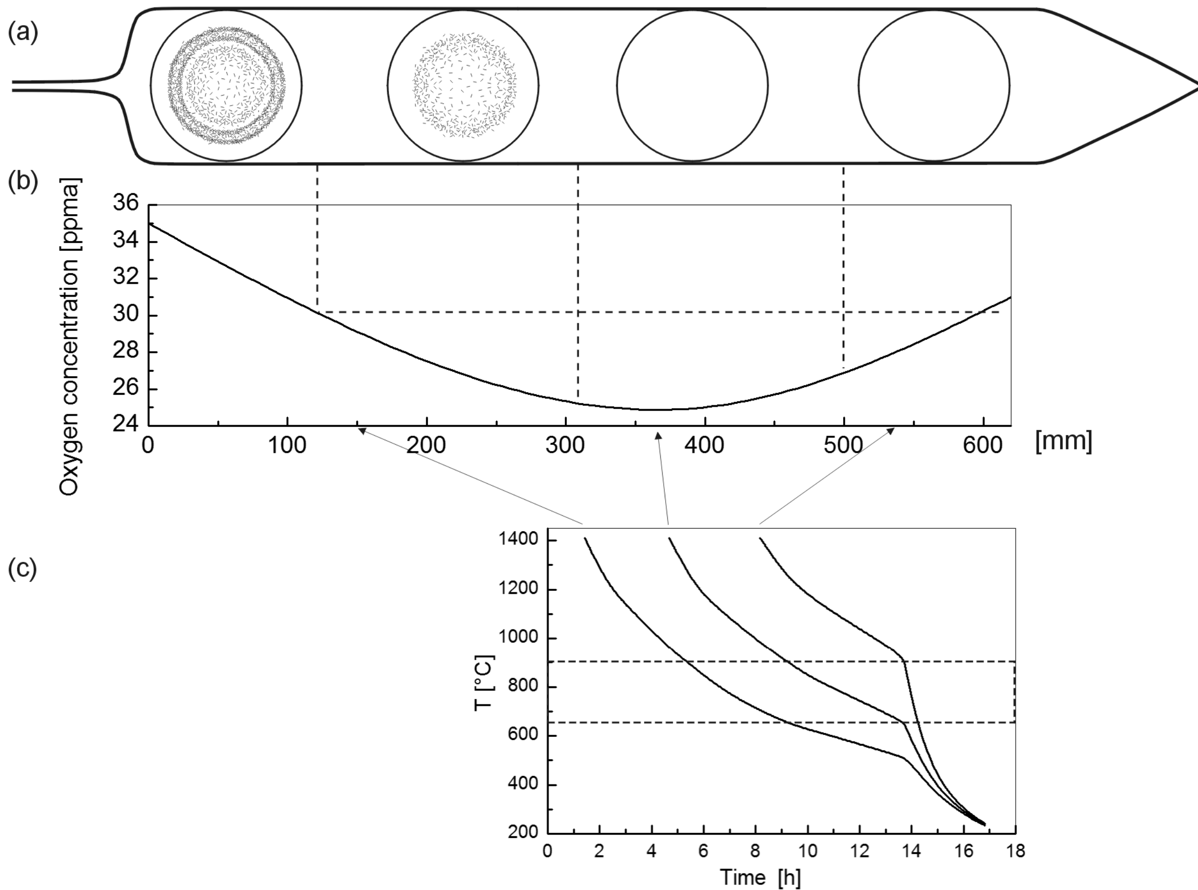

Figure 9.16: (a) Schematic representation of the observed OISF pattern throughout the crystal. (b) Axial profile of oxygen concentration in the crystal. (c) Thermal history modeled for three positions in the crystal shown by arrows.

values and consequently the time for the growth of oxide precipitates is shortened compared to higher oxygen levels. Decreasing oxygen concentration therefore results in reduction of size of the grown-in oxide precipitates. This scenario corresponds to the observed disappearance of the OISF pattern.

Oxygen concentration in the fourth quarter of the crystal rises again to the level of the second crystal quarter. However, while the OISF pattern is observed in the second quarter, no OISF pattern has been found in the fourth quarter. This phenomenon can be explained on the basis of the thermal history. Temperature evolution in these two crystal portions of essentially the same oxygen content differs as it is shown in Fig. 9.16c. It has been reported in [187] that the critical temperature range for formation of oxide precipitates during the crystal growth is about 900–600 °C. Fig. 9.16c shows that it is almost precisely this range where thermal history of the fourth crystal quarter differs from the rest of the crystal. After the growth of the crystal is completed, the crystal is detached from the melt and rather quickly cooled. While most of the crystal body dwells already at rather low temperature (around or below 650 °C), the tail-end of the crystal (the fourth quarter) experiences fast cooling from about 900 °C. It is clear from Fig. 9.16c that the dwell time in the temperature range of 900–650 °C is substantially shorter in the fourth crystal quarter compared to the rest of the crystal (approximately four times). As the result, one can expect formation of substantially smaller grown-in oxide precipitates in the fourth crystal quarter compared to the second quarter, despite the oxygen concentration in these crystal portions is the same.

Thus, the variation of size of the grown-in oxide precipitates along the crystal leading to the observed variation of the OISF pattern can be explained in terms of the axial profile of oxygen concentration and the crystal thermal history.

9.14. Summary on formation of the OISF pattern

Taking the above discussed mechanisms into account we can compile a consistent model qualitatively describing formation of crystal defects in our heavily boron-doped crystals:

1. The critical value of v/G is the function of boron concentration in the crystal; it can be expressed as the empirical logarithmical function (Eq. 9.1).
2. Lightly doped crystals are fully vacancy-rich; heavily doped crystals (boron concentration in the range of 1.7×10^{18}–1.3×10^{19} cm^{-3}) are of the mixed type and contain the V-I boundary; the most heavily doped crystals are fully interstitial-rich.
3. Formation of crystal defects from the crystallization temperature down to about 900 °C is described by the Voronkov theory outlined in Section 5.3 and Fig. 5.2. These processes result in a double peak radial profile of residual vacancies (Fig. 5.2e).
4. Residual vacancies assist in formation of the grown-in oxide precipitates during further cooling of the crystal. The density of the precipitates is proportional to concentration of vacancies. The highest density is achieved in the L- and H- bands; the density in the P-band and in the central region bound by the H-band is lower and no oxide precipitates are formed outside the V-I boundary, i.e. in the interstitial-rich region.
5. Oxide precipitates formed in the first crystal quarter reach the size which is supercritical at the temperature of the OISF test (1150 °C) and serve as the nucleation sites for OISF. The surface density of OISF reflects the bulk density of the grown-in precipitates. The resulting OISF pattern therefore reveals the V-I boundary and the L-, P- and H- bands in the vacancy-rich core.
6. The size of the grown-in oxide precipitates decreases with the distance from the seed-end as the consequence of decreasing oxygen concentration. As the size distribution curve shifts below the value of the critical radius of the nuclei at the temperature of the OISF test, larger amount of the grown-in precipitates dissolves and the OISF density decreases. The OISF pattern therefore gradually vanishes with increasing distance from the seed-end. As the L-band disappears sooner, the size of the precipitates in the L-band seems to be smaller compared to the H-band.
7. The size of the grown-in oxide precipitates in the tail-end of the crystal is reduced as the consequence of the faster cooling in the temperature range of about 900–650 °C. Therefore no OISF are formed in this crystal portion despite the oxygen concentration level sufficient for formation of stable OISF nuclei.

9.15. Enhanced precipitation of oxygen

It was shown in Section 5.5 that the OISF ring is formed on the wafers as the consequence of the fact that only the grown-in oxide precipitates in the P-band are supercritical at the temperature of the OISF test. In our case we see formation of supercritical precipitates especially in the L- and H- bands. Hence, oxygen precipitation in these bands is unusually strong. We reported on this phenomenon in [V, VI] and call it enhanced oxygen precipitation.

The observed OISF pattern following the radial profile of residual vacancies has not been published previously. The published data [177,179,180,188–190] report on formation of the OISF ring in the P-band. Parameters of the crystals studied in this work were compared to the data of other authors who also studied oxygen precipitation and OISF formation in heavily boron-doped silicon. While Dornberger [177] does not specify oxygen concentration in studied crystals, Kim et al. [180] report oxygen concentration of 26–28 ppma. Suhren [179] reports the oxygen content in the range of 23.5–35.5 ppma for 200 mm and 125 mm processes, but it is not clear what combinations of boron and oxygen concentration were studied. Oxygen concentration in the first crystal quarter of our crystals (where the complete OISF pattern and strongest oxygen precipitation is observed) is 29–35 ppma. This high value is likely the reason for the enhanced oxygen precipitation. However, the high oxygen concentration itself can not be the root cause as the standard OISF ring is observed in lightly doped crystals with the same oxygen content [188]. We can conclude that the enhanced oxygen precipitation observed in the L- and H- bands is the consequence of the combination of the high oxygen concentration, high boron concentration and suitable thermal history.

It was shown in section 9.9 that spatial distribution of the supercritical grown-in precipitates follows the radial profile of the residual vacancies. This profile is established around 900 °C (see Fig. 5.2). The temperature of about 600 °C can be considered as the lower limit below which formation of grown-in oxide precipitates is negligible due to very low oxygen diffusivity. Hence, enhanced precipitation of oxygen during the growth of the heavily boron-doped silicon crystals occurs in the temperature range of about 900–650 °C.

The schematic summary of our understanding of defect formation in boron doped silicon is presented in the following scenario:

- Lightly boron-doped crystals with a low oxygen concentration — formation of grown-in oxide precipitates is generally suppressed.
- Lightly boron-doped crystals with a sufficient oxygen concentration — small grown-in oxide precipitates are formed in the L- and H-band, large grown-in oxide precipitates are formed in the P-band. The precipitate density in the P-band is lower than in the L- and H-band.
- Heavily boron-doped crystals with a low oxygen concentration — formation of grown-in oxide precipitates is generally suppressed.
- Heavily boron-doped crystals with an intermediate oxygen concentration — large grown-in oxide precipitates are formed in the H-band and its interior.
- Heavily boron-doped crystals with a high oxygen concentration — large grown-in oxide precipitates are formed essentially in the whole vacancy-rich region. The precipitate density in the P-band and interior of the H-band is lower than in the L- and H-band.

9.16. Influence of boron on oxygen precipitation

Several mechanisms of the influence of boron doping on formation of crystal defects have been discussed in published papers.

In our previous work [V, VI] and section 9.12 we adopted the mechanism when the strain of the growing oxide precipitate is relieved by emission of silicon interstitials and we referred to a work of Ishikawa [183] showing increased equilibrium of self interstitials at higher boron concentration to explain oxygen precipitation in the interstitial-rich region. Other mechanisms of boron influence on defect formation have also been published.

Storage and release of silicon interstitials in boron-interstitial pairs was modeled by Sinno et al. [191]. It was shown that the position of the OISF ring is a function of boron concentration and can be explained by storage of silicon interstitials in BI and B_2I pairs at high temperatures. As free interstitials are consumed during recombination with vacancies, the boron-interstitial pairs start to dissociate and new interstitials are released into the lattice. These extra interstitials recombine with remaining vacancies. The V-I boundary thus shift to the originally vacancy-rich region. In other words, the OISF ring shrinks with increasing boron concentration.

Electronic shift effect on equilibrium concentrations of intrinsic point defects was proposed by Voronkov and Falster [178]. Substitutional boron in the silicon lattice induces a shift in the electron concentration with respect to the intrinsic value. The shifted electron concentration is proportional to boron concentration. As vacancies in silicon are assumed to be single negatively charged, their concentration is influenced by the concentration of free electrons. Taking the law of mass action into consideration it follows that the equilibrium concentration of charged vacancies is shifted in inverse proportion to the concentration of boron. The increasing boron concentration (leading to decreased vacancy concentration) therefore results in shifting of the V-I boundary to the originally vacancy-rich region and shrinking of the OISF ring.

FTIR analyses of oxide precipitates performed by De Gryse et al. [192] indicate that the chemical composition of the precipitates varies with boron concentration. While oxide precipitates in the lightly boron-doped silicon consist of a mixture of SiO_2 and Si, a mixture of SiO_2 and B_2O_3 was identified in the precipitates in the heavily boron-doped silicon. The fraction of B_2O_3 was up to 40% of the precipitate volume in the material doped to about 8 mΩ cm. Due to lower bulk modulus of B_2O_3 oxide precipitates in heavily doped silicon are more easily compressed which has implications for the injection of silicon interstitials into the lattice. It can be concluded that the growth of oxide precipitates in heavily boron-doped silicon is enhanced due to lower emision of silicon interstitials into surrounding lattice.

Reduction of the strain related to the precipitate growth in heavily boron-doped silicon was indicated also by Ono et al. [193] as the result of boron segregation into oxide precipitates. Smaller boron atoms incorporated into the precipitate instead of silicon provide free space for the precipitate growth. Oxygen precipitation in heavily boron-doped silicon is therefore easier compared to the lightly doped material. The effect of stress relief by boron incorporation was simulated with good agreement to the experimental data [194].

Other mechanisms influencing formation of crystal defects in heavily-boron doped silicon were also proposed such as clustering of boron atoms and oxygen which reduces the concentration of interstitial oxygen [195, 196] and thermal donor formation [197, 198]. These do not seem to be much probable and are not further considered in this work.

The mechanisms of boron-interstitial pairing and electronic shift effect were discussed only with respect to establishment of the V-I boundary during the recombination stage of defect formation [178, 191, 199]. On the other hand the effect of strain relief by boron incorporation into the precipitates was studied while the nature of the material (vacancy-rich or interstitial-rich material) and the influence on the V-I boundary were not considered. The older works

have to be considered carefully in general because the authors did not consider vacancy-rich and interstitial-rich material (which is a critical factor) at that time.

Although the mechanism of boron influence on formation of defects in silicon remains uncertain, the basic feature is generally accepted — formation of an oxide precipitate is accompanied by formation of strain which has to be relieved in order to allow the precipitate to grow. As concluded in section 9.15 enhancement of precipitation in the L- and H-band occurs at lower temperatures (roughly 900–650 °C). At these temperatures the suppressed emission of silicon interstitials due to low equilibrium concentration of interstitials is the main force acting against precipitate growth (see section 4.3.4). Let us discuss the possible mechanisms of enhanced emission of interstitials:

- As the equilibrium concentration of boron-interstitial pairs is an increasing function of temperature [191], the population of the BI and B_2I pairs at lower temperature would be saturated by the pairs formed at higher temperature. Formation of new pairs would therefore be suppressed. Besides, decomposition of the boron-interstitial pairs would tend to add interstitials into the lattice. This effect would act against emission of next interstitials from the precipitate. Therefore, boron-interstitial pairing seems not to be the reason for enhanced oxygen precipitation.
- The decreased vacancy concentration due to the electronic shift effect would modify radial position of microdefect bands. To be more precise the microdefect bands would move towards the V-I boundary and the diameter of the void-containing region would increase because the same vacancy supersaturation would be achieved for lower vacancy concentration. The reason arises from the fact that vacancy supersaturation is the driving force for void formation and is also considered as the supportive driving force for oxygen precipitation in Voronkov's models [108, 111]. The defect formation at higher temperatures would be enhanced due to increased vacancy supersaturation and the concentration of residual vacancies would decrease consequently. This effect would act against formation of the grown-in oxygen precipitates below 900 °C.
- The increased equilibrium concentration of silicon interstitials would enhance emission of interstitials by decreased interstitial supersaturation. This effect can enhance oxygen precipitation.
- Incorporation of boron into the precipitate would decrease number of emitted interstitials per size increment. The increase of interstitial supersaturation would be slowed down and precipitation would be enhanced.

Although the position of the V-I boundary was explained by the electronic shift [178] and boron-interstitial pairing [191], it seems that these effects cannot be the root cause of enhanced precipitation of oxygen at lower temperatures. On the other hand the influence of boron on the equilibrium concentration of interstitials [183] or boron incorporation into the oxide precipitates [192–194] might be responsible for enhanced precipitation of oxygen in heavily boron-doped silicon.

10. Summary

This work is focused on the study of crystal defects in silicon single crystals, particularly in silicon crystals doped with boron.

An unusual distribution of oxidation induced stacking faults (OISFs) was observed on the surface of heavily boron-doped wafers. The author performed a detailed analysis of the OISF distribution over a wide range of boron doping levels. The analysis revealed circular OISF patterns whose shape varied as the function of doping level and position in the crystal. The full pattern consisting of a thin ring of OISFs outside a full circle of OISFs is formed in the crystal beginning. The observed OISF patterns have not been published before.

The author identified a qualitative agreement between the radial profile of OISF surface density and the radial profile of residual vacancies described by the model published by other authors. This correlation enabled identification of specific bands of crystal defects within the OISF pattern. The so called H-, P-, and L-bands were identified as well as the vacancy-interstitial (V-I) boundary.

The correct identification of the V-I boundary was experimentally verified by delineation of vacancy type bulk defects — the COPs. Computer simulations of crystal growth were utilized for modeling of the V-I boundary in the crystal. The critical v/G parameter was determined as the function of boron concentration using the measured radii of the OISF patterns. A reasonable quantitative agreement of the modeled V-I boundary and defect distribution in the crystals was achieved.

Based on the results of X-ray section topography and a specific OISF test with pre-annealing the author showed that the oxide precipitates formed during the crystal growth — the grown-in precipitates — are the nuclei for the OISFs observed on the wafer surface. The observed changes in the OISF pattern were explained on the basis of oxygen precipitation dependent on the position in the crystal. This dependence was explicated in terms of oxygen concentration and thermal history.

The performed analyses revealed that the oxygen precipitation in the studied crystals was significantly enhanced in the H- and L-bands. This effect, unpublished by other authors, was explained by a qualitative model of formation of crystal defects in boron-doped silicon. The presented model explains enhanced precipitation of oxygen through coincident effect of high boron concentration, high oxygen concentration, and favorable thermal history. The dependence of the equilibrium concentration of silicon interstitials on boron concentration or incorporation of boron into oxide precipitates were identified as possible mechanisms behind the enhanced oxygen precipitation.

Based on results of this work the author implemented new analytical methods for defect study and optimized crystal growth processes in ON Semiconductor:

- the chromium-free OISF test (section 6.6);
- the COP test (section 6.7);
- the copper decoration technique (section 6.8);
- the crystal growth process optimized through v/G for suppression of defect formation (section 7.6);
- the OISF test with pre-annealing (section 9.12).

Author‘s contribution

The author of this work identified the topic, planned the tests and personally performed the analyses, tests and measurements except:

- the test crystals were grown by ON Semiconductor employees;
- the boron and oxygen concentrations were measured by standard manufacturing procedures by ON Semiconductor employees;
- the X-ray section topograms were acquired by RNDr. Stanislav Banáš, ON Semiconductor;
- the COP maps were measured by Ing. Ivona Pavelkova, ON Semiconductor;
- the cross-sections of the wafers were prepared and pictures taken by ON Semiconductor laboratories;
- the chromium-free OISF test (section 6.6) was developed in cooperation with summer stay student Lukáš Střižík, University of Pardubice;
- the copper decoration technique (section 6.8) was developed in cooperation with summer stay students Jiří Orava and Štěpán Stehlík, University of Pardubice.

References

[1] F. Seitz and N.G. Einspruch, in H.R. Huff, U. Gösele, H. Tsuya, editors, Semiconductor Silicon 1998, PV1998−1, The Electrochemical Society, Penington, NJ (1998), p. 69.

[2] W.M. Bullis, in W.C. O'Mara, R.P. Herring and L.P. Hunt, editors, Handbook of Silicon Technology, Noyes Publications, Park Ridge, NJ (1990), p. 347.

[3] H.J. Queisser, in H.R. Huff, U. Gösele, H. Tsuya, editors, Semiconductor Silicon 1998, PV1998−1, The Electrochemical Society, Penington, NJ (1998), p. 4.

[4] J. Bardeen, W. Brattain, Phys. Rev. 75 (1949) 1208.

[5] W.B. Shockley, Electrons and Holes in Semiconductors, Van Nostrand, New York (1950).

[6] G.K. Teal, J.B. Little, Phys. Rev. 78 (1950) 647.

[7] G.K. Teal, E. Bühler, Phys. Rev. 87 (1952) 190.

[8] G.K. Teal, IEEE Trans. Electron Devices ED−23 (1976) 621.

[9] H.E. Buckley, Crystal Growth, Wiley, New York (1951).

[10] J. Czochralski, Z. Physik. Chem. 92 (1918) 219.

[11] D. Huber, in H.R. Huff, U. Gösele, H. Tsuya, editors, Semiconductor Silicon 1998, PV1998−1, The Electrochemical Society, Penington, NJ (1998), p. 116.

[12] W.G. Pfann, Trans. AIME 194 (1952) 747.

[13] P.H. Keck, M.J.E. Golay, Phys. Rev. 89 (1953) 1297.

[14] W. Dash, J. Appl. Phys. 30 (1959) 459.

[15] W. Heywang, K.H. Zaininger, in P. Siffert, E. Krimmel, editors, Silicon: Evolution and Future of a Technology, Springer−Verlag, Berlin−Heidelberg (2004), p. 25.

[16] M. Kuramoto, in H.R. Huff, L. Fabry, S. Kishimo, editors, Semiconductor Silicon 2002, PV2002−2, The Electrochemical Society, Penington, NJ (2002), p. 163.

[17] D.T.J. Hurle, Crystal Pulling from the Melt, Springer−Verlag, Berlin−Heidelberg (1993).

[18] H.M. Liaw, Crystal Growth of Silicon, in W.C. O'Mara, R.P. Herring and L.P. Hunt, editors, Handbook of Silicon Technology, Noyes Publications, Park Ridge, NJ (1990), p. 94.

[19] W. Zulehner, in M. Schulz, H. Weis, editors, Landolt−Börnstein: Numerical Data and Functional Relationships in Science and Technology, Group II, Vol. 17, Subvol. C, Springer−Verlag, Berlin−Heidelberg (1984), p. 28.

[20] A. Mühlbauer, in M. Schulz, H. Weis, editors, Landolt−Börnstein: Numerical Data and Functional Relationships in Science and Technology, Group II, Vol. 17, Subvol. C, Springer−Verlag, Berlin−Heidelberg (1984), p. 41.

[21] W.C. O'Mara, in W.C. O'Mara, R.P. Herring and L.P. Hunt, editors, Handbook of Silicon Technology, Noyes Publications, Park Ridge, NJ (1990), p. 451.

[22] P. Pichler, Intrinsic Point Defects, Impurities, and Their diffusion in Silicon, Springer −Verlag, Wien, 2004.

[23] Defects in Silicon I−III, a series of proceedings from ECS meetings, The Electrochemical Society, Penington, NJ.

[24] High Purity Silicon I−X, a series of proceedings from ECS meetings, The Electrochemical Society, Penington, NJ.

[25] Gettering and Defect Engineering in Semiconductor Technology (GADEST) I−XIII, proceedings of the GADEST meetings published in Solid State Phenomena, Trans Tech Publications Ltd, Stafa−Zurich, Switzerland.

[26] H.J. Queisser, Solid State Electron. 5 (1962) 1.

[27] T. Abe, T. Samizo and S. Maruyama, Jpn. J. Appl. Phys. 5 (1966) 458.

[28] T.S. Plaskett, Trans. AIME 233 (1965) 809.

[29] A.R.J. de Kock, Phillips Res. Rept. Suppl. No.1 (1973).

[30] H. Föll and B.O. Kolbesen, Appl. Phys. 8 (1975) 319.

[31] P.M. Petroff, A.R.J. de Kock, J. Cryst. Growth 30 (1975) 117.

[32] H. Föll, U. Gösele, B.O. Kolbesen, J. Cryst. Growth 40 (1977) 90.

[33] B. Jakowlew, W. Jeske, J. Weyher, Krist. Tech. Vol. 5, no. 13, (1978) 553.

[34] N.V. Veselovskaya, E.G. Sheikhet, K.N. Neimark, E.S. Falkevich In: Rosti legirovanie polyprovodnikovych kristallov i plenok. Novosibirsk: Nauka, Vol. 2. (1977) 284.

[35] A.J.R. Kock, W.T. Stacy, W.M. van de Wijgert, Appl. Phys. Lett. 34 (1979) 611.

[36] P.J. Roksnoer, M.M.B. van den Boom, J. Cryst. Growth. 53 (1981) 563.

[37] P.J. Roksnoer, J. Cryst. Growth 68 (1984) 596.

[38] K. Tempelhoff, N. Van Sung, Phys. Stat. Sol. 70 (1982) 441.

[39] A.J.R. de Kock, P.J. Roksnoer, P.G.T. Boonen, J. Cryst. Growth 22 (1974) 311.

[40] J.A. Van Vechten, Phys. Rev. B 17 (1978) 3197.

[41] S.M. Hu, J. Vac. Sci. Technol. 14 (1977) 17.

[42] E. Sirtl, Semiconductor Silicon 1977, Electrochem. Soc., Pennington, NJ (1977) 4.

[43] V.V. Voronkov, J. Cryst. Growth 59 (1982) 625.

[44] W. Kaiser, P.H. Keck, C.F. Lange, Phys. Rev. 101 (1956) 1264.

[45] R.E. Chaney, C.J. Varker, J. Cryst. Growth (1976) 188.

[46] W. Kaiser, P.H. Keck, J. Appl. Phys. 28 (1957) 882.

[47] C.S. Fuller, R.A. Logan, J. Appl. Phys. 28 (1957) 1427.

[48] W. Kaiser, H.L. Frisch, H. Reis, Phys. Rev. 112 (1958) 1546.

[49] J.R. Patel, A.R. Chaudhuri, J. Appl. Phys. 33 (1962) 2233.

[50] K. Yasutake, M. Umeno, H. Kawabe, Appl. Phys. Lett. 37 (1980) 789.

[51] Y. Kondo, in H.R. Huff, R.J. Kriegler, Y. Talehishi, editors, Semiconductor Silicon 1981, The Electrochem. Society, Pennington, N.J. (1981), p. 220.

[52] B. Leroy, C. Plougonven, J. Electrochem. Soc. 127 (1980) 961.

[53] H. Shimizu, T. Watanabe, Y. Kakui, Japan. J. Appl. Phys. 24 (1985) 815.

[54] D.M. Maher, A. Staudinger, J.R. Patel, J. Appl. Phys. 47 (1976) 3813.

[55] F. Shimura, H. Tsuya, T. Kawamura, J. Appl. Phys 51 (1980) 269.

[56] T. Abe, in H.R. Huff, U. Gösele, H. Tsuya, editors, Semiconductor Silicon 1998, PV1998−1, The Electrochemical Society, Penington, NJ (1998), p. 157.

[57] B.O. Kolbesen, A. Mühlbauer, Solid−State Electronics 25 (1982) 759.

[58] T. Nozaki, Y. Yatsuguri, N. Akiyama, J. Electrochem. Soc. 117 (1970) 1566.

[59] A.R. Bean, R.C. Newman, J. Phys. Chem. Solids 33 (1972) 255.

[60] S. Kishino, Y. Matsushita, M. Kanamori, Appl. Phys. Lett. 35 (1979) 213.

[61] A.J.R. de Kock, W.M. van de Wijgert, J. Cryst. Growth 49 (1980) 718.

[62] G.A. Rozgonyi, R.P. Deysher, C.W. Pearce, J. Electrochem. Soc. 123 (1976) 1910.

[63] T.Y. Tan, E.E. Gardner, W.K. Tice, Appl. Phys. Lett. 30 (1977) 175.

[64] G.A. Rozgonyi, C.W. Pearce, Gettering of Surface and Bulk Impurities in Czochralski silicon wafers, Appl. Phys. Lett. 32 (1978) 747.

[65] K. Sumino, H. Harada, I. Yonenaga, Jpn. J. Appl. Phys. 19 (1980) 49.

[66] K. Sumino, I. Yonenaga, Jpn. J. Appl. Phys. 20 (1981) 685.

[67] H. Harada, T. Abe, and J. Chikawa, in Semiconductor Silicon 1986, H. R. Huff, Editor, PV 86−4, The Electrochemical Society Proceedings Series, Pennington, NJ (1986), p. 76.

[68] M. Hourai, M. Sano, S. Sumita, and T. Shigematsu, in Progress in Semiconductor Fabrication, SEMICON Technical Conference, Geneva (1993).

[69] S. Sadamitsu, S. Umeno, Y. Koike, M. Hourai, S. Sumita and T. Shigematsu, Jpn. J. Appl. Phys. 32 (1993) 3675.

[70] J. Ryuta, E. Morita, T. Tanaka, Y. Shimanuki, Jpn. J. Appl. Phys. 29 (1990) 1947.

[71] J. Ryuta, E. Morita, T. Tanaka, Y. Shimanuki, Jpn. J. Appl. Phys. 31 (1992) 293.

[72] H. Yamagishi , I. Fusegawa , N. Fujimaki, M. Katayama, Semicond. Sci. Technol. 7 (1992) 135.

[73] M. Itsumi, H. Akia, T. Ueki, J. Appl. Phys. 78 (1995) 5984.

[74] J.G. Park, G.A. Rozgonyi, Solid State Phenomena 47−48 (1996) 327.

[75] Ch. Kittel, H. Krömer, Thermal Physics. W. H. Freeman, New York (2000).

[76] F. Shimura, Semiconductor Silicon Crystal Technology, Academic Press, California (1989).

[77] ASTM F1188−02, "Standard Test Method for Interstitial Atomic Oxygen Content of Silicon by Infrared Absorption with Short Baseline", ASTM International, 2003.

[78] W. Götz, G. Pensl, Phys. Rev. B 46 (1992) 4312.

[79] R. C. Newman, J. Phys.: Condens. Matter 12 (2000) R335.

[80] K. Graff, Metal Impurities in Silicon−device Fabrication, Springer Series in Mat. Science, Springer−Verlag, Berlin Heidelberg 2000.

[81] S. Kawado et al., J. Phys. D: Appl. Phys. 38 (2005) A17.

[82] J.P. Hirth, J. Lothe, Theory of dislocations, McGraw-Hill, New-York (1967).

[83] K.V. Ravi, C.J. Varker, J. Appl. Phys 45 (1974) 263.

[84] M. Itsumi, J. Cryst. Growth 237−239 (2002) 1773.

[85] M. Kato, H. Takeno, Y. Kitagawara, in Proceedings of the MRS Fall Meeting, Defects in Electronic Materials II, Mater. Res. Soc., Pittsburgh, USA (1997), p. 119.

[86] J. Vanhellemont, S. Senkader, G. Kissinger, V. Higgs, M.−A. Trauwaert, D. Graef, U. Lambert, P. Wagner, Measurement, J. Cryst. Growth 180 (1997) 353.

[87] F. Shimura, Oxygen in Silicon, Academic Press, London (1994).

[88] J. Vanhellemont, J. Esfandyari, G. Obermeier, E. Dornberger, D. Graef, U. Lambert, in C.L Claeys, P.Rai-Choudhury, M. Watanabe, P. Stallhofer, H.J. Dawson, editors, High Purity Silicon V, Vol. 98−13, The Electrochemical Society, Penington, NJ (1998), p. 101.

[89] H. Bender, Phys. Stat. Solidi A 86 (1984) 245.

[90] T.Y. Tan, W.K. Tice, Philos. Mag. 34 (1976) 615.

[91] P. Capper, A.W. Iones, J. Appl. Phys. 48 (1977) 1646

[92] W. Bergholz, M.J. Binns, G.R. Booker, J.C. Hutchison, S.H. Kinder, S. Messoloras, R.C. Newman, R.J. Stewart, J.G. Wilkes, Philos. Mag. B 59 (1989) 499.

[93] A. Borghesi, B. Pivac, A. Sassella, A. Stella, J. Appl. Phys. 77 (1995) 4169.

[94] K. Sakai, T. Yamagami, K. Ojima, J. Cryst. Growth 210 (2000) 65.

[95] T. Ono, G. A. Rozgonyi, C. Au, T. Messina, R. K. Goodall, and H. R. Huff, J. Electrochem. Soc. 146 (1999) 3807.

[96] Y. Satoh, T. Shiota, Y. Murakami, T. Shingyouji, H. Furuya, J. Appl. Phys. 79 (1996) 7944.

[97] S. Kim, W. Wijaranakula, in High Density Memory Devices, MRS Proceedings, Vol. 378 (1995) 725.

[98] D. Gräf, U. Lambert, M. Brohl, A. Ehlert, R. Wahlich and P. Wagner, Mat. Sci. Eng. B 36 (1996) 50.

[99] Y. Yanase, H. Nishihata, T. Ochiai, H. Tsuya, Jpn. J. Appl. Phys. 37 (1998) 1.

[100] W. von Ammon, P. Drier, W. Hensel, U. Lambert, L. Kostler, Mater. Sci. Eng. B 36 (1996) 33.

[101] T. Abe, M. Kimura, in: H.R. Huff, et al., (Eds.), Semiconductor Silicon 1990, The Electrochem. Soc, Pennington, NJ (1990), p. 105.

[102] J. L. Vasat, T. Torack, Solid State Technology 46 (2003).

[103] T. Abe, H. Harada, J. Chikawa, Physica B+C 116 (1983) 139.

[104] P.C. Parekh, Solid−State Electron. 14 (1971) 273.

[105] Barson, M. S. Hess, and M. M. Roy, J. Electrochem. Soc. 116 (1969) 304.

[106] D.K. Schroder, in Gettering and Defect Engineering in the Semiconductor Technology, M. Kittler, editor, Sci−Tech, Vaduz, Switzerland (1989), p. 383.

[107] V.V. Voronkov, R. Falster, J. Appl. Phys. 86 (1999) 5975.

[108] V.V. Voronkov, J. Cryst. Growth 310 (2008) 1307.

[109] V.V. Voronkov, R. Falster, Materials Science and Engineering B 159−160 (2009) 138.

[110] W. von Ammon, E. Dornberger, and O.P. Hansson, J. Cryst. Growth, 198/199 (1999) 390.

[111] V.V. Voronkov, R. Falster, J. Cryst. Growth 204 (1999) 462.

[112] E. Dornberger, D. Gräf, M. Suhren, U. Lambert, P. Wagner, F. Dupret, and W. von Ammon, J. Cryst. Growth, 180 (1997) 343.

[113] L. I. Huang, P. C. Lee, C. K. Hsieh, W. C. Shu, and C. W. Lan, J. Cryst. Growth, 226 (2004) 132.

[114] G. Borionetti, D. Gambaro, M. Porrini, and V. V. Voronkov, in Semiconductor Silicon 2002, H. R. Huff, L. Fabry, and S. Kishino, editors, PV 2002−2 The Electrochemical Society Proceedings Series, Penington, NJ (2002), p. 505.

[115] S.M. Hu, J. Appl. Phys., 45 (1974) 1567.

[116] W. Zulehner, in M. Schulz, editor, Landolt−Börnstein: Numerical Data and Functional Relationships in Science and Technology, Group III, Vol. 22, Subvol. B, p. 411, Springer−Verlag, Berlin−Heidelberg (1989), p. 111.

[117] J.R. Patel, K.A. Jackson, H. Reiss, J. Appl. Phys 48 (1977) 5279.

[118] M. Hasebe, Y. Takeoka, S. Shinoyama and S. Naito, Jpn. J. Appl. Phys. 28 (1989) L1999.

[119] F.S. Ham, J. Phys. Chem. Solids 6 (1958) 335.

[120] J. Mikkelsen, Mater. Res. Soc. Symp. Proc. 59 (1986) 19.

[121] J. Vanhellemont, C. Clayes, J. Appl. Phys. 62 (1987) 3960.

[122] J. Vanhellemont, J. Appl. Phys. 78 (1995) 4297.

[123] N. Inoue, J. Osaka, and K. Wada, J. Electrochem. Soc. 129 (1982) 2780.

[124] N.I. Puzanov and A.M. Eidenzan, Semicond. Sci. Technol. 7 (1992) 406.

[125] F1239−02, Standard Test Methods for Oxygen Precipitation Characterization of Silicon Wafers by Measurement of Interstitial Oxygen Reduction, American Society for Testing and Materials, ASTM International, 2002.

[126] F 1809 − 02, Standard Guide for Selection and Use of Etching Solutions to Delineate Structural Defects in Silicon, American Society for Testing and Materials, ASTM International, 2002.

[127] K.R. Wiliams, in R. Hull, Properties of Crystalline Silicon, INSPEC, The institution of Electrical Engineers, London, UK (1999), p. 809.

[128] M. Wright−Jenkins, J. Electrochem. Soc. 124 (1977) 757.

[129] E. Sirtl, A. Adler, Zeitschrift fur Metalkunde, 52 (1961) 529.

[130] D.G. Schimmel, J. Electrochem. Soc. 126 (1979) 479.

[131] K. H. Yang, J. Electrochem. Soc. 131 (1984) 1140.

[132] F. Secco d'Arragona, J. Electrochem. Soc. 110 (1972) 948.

[133] T.C. Chandler, J. Electrochem. Soc. 137 (1990) 944.

[134] W.C. Dash, J. Appl. Phys. 27 (1956) 1193.

[135] A.R. Lang, in S. Amelinckx, R. Gevers, J. Van Landuyt, editors, Diffraction and Imaging Techniques in Materials Science, North-Holland, Amsterdam, Holand (1978), p. 623.

[136] W. Bergholz, in M. Schulz, editor, Landolt−Börnstein: Numerical Data and Functional Relationships in Science and Technology, Group III, Vol. 22, Subvol. B, p. 411, Springer−Verlag, Berlin−Heidelberg (1989), p. 131.

[137] F 1127 − 02, Standard Practice for Detection of Oxidation Induced Defects in Polished Silicon Wafers, American Society for Testing and Materials, ASTM International, 2002.

[138] L. Mule'Stagno, Solid State Phenom. 82−84 (2002) 753.

[139] J. Esfandyari, C. Schmeiser, S. Senkader, G. Hobler, B. Murphy, J. Electrochem. Soc. 143 (1996) 995.

[140] M. Akatsuka, M. Okui, S. Umeno, K. Sueoka, J. Electrochem. Soc. 150 (2003) G587.

[141] R.A. Brown, Z. Wang, T. Mori, J. Cryst. Growth 225 (2001) 97.

[142] E. Dornberger, W. von Ammon, J. Virbulis, B. Hanna, T. Sinno, J. Cryst. Growth 230 (2001) 291.

[143] N. Van Goethem, A. de Potter, N. Van den Bogaert, F. Dupret, J. Phys. Chem. of Solids 69 (2008) 320.

[144] P. Hopfgartner, P. Collareta, M. Porrini, Mat. Science and Engineering B73 (2000) 158.

[145] V.V. Kalaev, D.P. Lukanin, V.A. Zabelin, Yu.N. Makarov, J. Virbulis, E. Dornberger, W. von Ammon, Mat. Science in Semiconductor Processing 5 (2003) 369.

[146] M.S. Kulkarni, J. Cryst. Growth 303 (2007) 438.

[147] K. Sueoka, M. Akatsuka, M. Okui, H. Katahama, J. Electrochem. Soc. 150 (2003) G469.

[148] A. Virzi, M. Porrini, Mat. Sc. and Eng. B17 (1993) 196.

[149] V.V. Voronkov, R. Falster, J. Appl. Phys. 91 (2002) 5802.

[150] M. Kurz, A. Pusztai, G. Müller, J. Cryst. Growth 198−199 (1999), pp. 101.

[151] F. Dupret, P. Nicodeme, Y. Ryckmans, P. Wouters, M.J. Crochet, Int. J. Heat Mass Transfer 33 (1990) 1849.

[152] R.A. Brown, T. Kinney, P. Sackinger, D. Bornside, J. Cryst. Growth 97 (1989) 99.

[153] V.V. Kalaev, I.Yu. Evstratov, Yu.N. Makarov, J. Cryst. Growth 249 (1−2) (2003) 87.

[154] I.Yu. Evstratov, V.V. Kalaev, V.N. Nabokov, A.I. Zhmakin, Yu.N. Makarov, A.G. Abramov, N.G. Ivanov, E.A. Rudinsky , E.M. Smirnov, S.A. Lowry , E. Dornberger, J. Virbulis, E. Tomzig, W. von Ammon, Microelectronic Engineering 56 (2001) 139.

[155] L.Y. Huang, P.C. Lee, C.K. Hsieh, W.C. Hsu, C.W. Lan, J. Cryst. Growth 261 (2004) 433.

[156] A. Raufeisen, S. Jana, M. Breuer, T. Botsch, F. Durst, J. Cryst. Growth 303 (2007) 146.

[157] Th. Wetzel, J. Virbulis, A. Muiznieks, W. von Ammon, E. Tomzig,G. Raming, M. Weber, J. Crys. Growth 266 (2004) 34.

[158] Y. Shiraishi, K. Takano, J. Matsubara, T. Iida, N. Takase, N. Machida, M. Kuramoto, H. Yamagishi, J. Cryst. Growth 229 (2001) 17.

[159] V.V. Kalaev, J. Cryst. Growth 303 (2007) 203.

[160] J. Virbulis, Th. Wetzel, E. Tomzig, W. von Ammon, Materials Science in Semiconductor Processing 5 (2003) 353.

[161] D. Vizman, M. Watanabe, J. Friedrich, G. Muller, J. Cryst. Growth 303 (2007) 221.

[162] J. Virbulis, Th. Wetzel, A. Muiznieks, B. Hanna, E. Dornberger, E. Tomzig, A. Mühlbauer, W.v. Ammon, J. Cryst. Growth 230 (2001) 92.

[163] V. Savolainen, J. Heikonen, J. Ruokolainen, O. Anttila, M. Laakso, J. Paloheimo, J. Cryst. Growth 243 (2002) 243.

[164] C. Wang, H. Zhang, T.H. Wang, T.F. Ciszek, J. Cryst. Growth 250 (2003) 209.

[165] K. Nagasawa, Y. Matsushita, and S. Kishino, Appl. Phys. Lett. 3 (1980) 622.

[166] J. Andrews, in W.M. Bullis, L.C. Kimerling, Defects in Silicon, The Electrochemical Society, Pennington, NJ (1983), p. 133.

[167] S. Nadahara, H. Kubota, S. Samata, Solid State Phenomena 57-58 (1997) 19.

[168] N. Adachi, T. Hisatomi, M. Sano, H. Tsuya, H. in H.R. Huff, U. Gösele, H. Tsuya, editors, Semiconductor Silicon 1998, The Electrochemical Society, Pennington, NJ (1998), p. 698.

[169] D.T.J. Hurle, Crystal Pulling from the Melt, Springer-Verlag Berlin-Heidelberg New York, Berlin, Germany (1993).

[170] W. von Ammon, R. Holzl, J. Virbulis, E. Dornberger, R. Schmolke, D. Gräf, J. Cryst. Growth 226 (2001) 19.

[171] A. Ikari, K. Nakai, Y. Tachikawa, H. Deai, Y. Hideki, Y. Ohta, N. Masahashi, S. Hayashi, T. Hoshino, W. Ohashi, Solid State Phenomena 69-70 (1999) 161.

[172] R. Falster, D. Gambaro, M. Olmo, M. Cornara, H. Korb, Material Research Society Syposium Proceedings 510 (1998) 27.

[173] FEMAGSoft Home Page, `www.femagsoft.com`, August 2012.

[174] F. Dupret, P. Nicodeme, Y. Ryckmans, P. Wouters, M. Crochet, Int. J. Heat Mass Transfer 33 (1990) 1849.

[175] ASTM F723−99, "Standard Practice for Conversion between Resistivity and Dopant Density for Boron−Doped, Phosphorus−Doped, and Arsenic−Doped Silicon", ASTM International, 2003.

[176] M. Porrini, Cryst. Res. Technol. 40 (2005) 1054.

[177] E. Dornberger, Prediction of OSF Ring Dynamics and Grown−in Voids in Czochralski Silicon Crystals, PhD thesis, Universite Catholique de Louvain, Louvain−la−Neuve (1997).

[178] V.V. Voronkov, R. Falster, J. Appl. Phys. 87 (2000) 4126.

[179] M. Suhren, D. Gräf, U. Lambert and P. Wagner, J. Electrochem. Soc. 144 (1997) 4041.

[180] J.−M. Kim, J.−Y. Choi, H.−J. Cho, H.−W. Lee and H.−D. Yoo, Jpn. J. Appl. Phys. 40 (2001) 1370.

[181] E. Asayama, T. Ono, M. Takeshita, M. Hourai, M. Sano, and H. Tsuya, in H.R. Huff, U. Gösele, and H. Tsuya, editors, Semiconductor Silicon 1998, PV 1998-1, The Electrochemical Society, Pennington, NJ (1998), p. 546.

[182] T. Y. Tan, C. Y. Kung, J. Appl. Phys. 59 (1986) 917.

[183] F. Ishikawa, T. Saishoji, K. Nakamura, and J. Tomioka, Extended Abstracts of the 58th Autumn Meeting, Japan Society of Applied Physics (1997) 243.

[184] P. Hopfanger, P. Collareta, M. Porrini, Mater. Sci. Eng. B73 (2000) 158.

[185] B. Borionetti, D. Gambaro, S. Santi, M. Borgini, P. Godio, S. Pizzini, Mater. Sci. Eng. B73 (2000) 218. 30

[186] K. Sueoka, M. Akatsuka, M. Okui and H. Katahama, in H. R. Huff, U. Gösele, H. Tsuya, editors, Semiconductor Silicon 2002, PV2002−2, The Electrochemical Society, Pennington, NJ (2002), p. 540.

[187] M. Porrini, P. Rossetto, Mater. Sci. Eng. B36 (1996) 162.

[188] M. Hourai, H. Nishikawa, T. Tanaka, S. Umeno, E. Asayama, T. Nomachi and G. Kelly, in H. R. Huff, U. Gösele, H. Tsuya, editors, Semiconductor Silicon 1998, PV1998−1, The Electrochemical Society, Pennington, NJ (1998), p. 453.

[189] G. Kissinger, J. Vanhellemont, U. Lambert, D. Gräf, E. Dornberger and H. Richter, J. Electrochem. Soc. 145 (1998) 75.

[190] N. Ono, K. Harada, J. Furukawa, K. Suzuki, M. Kida and Y. Shimanuki, in H. R. Huff, U. Gösele, H. Tsuya, editors, Semiconductor Silicon 1998, PV1998−1, , The Electrochemical Society, Pennington, NJ (1998), p. 503.

[191] T. Sinno, H. Susanto, R.A. Brown, W. von Ammon, E. Dornberger, Appl. Phys. Lett. 75 (1999) 1544.

[192] O. De Gryse, J. Vanhellemont, P. Clauws, O. Lebedev, J. Van Landuyt, E. Simoen, C. Claeys, Physica B 340-342 (2003) 1013.

[193] T. Ono, E. Asayama, H. Horie, M. Hourai, K. Sueoka, H. Tsuya and G. Rozgonyi, J. Electrochem. Soc. 146 (1999) 2239.

[194] H. Takeno, K. Aihara, Y. Hayamizu, Y. Kitawara, in H.R. Huff, U. Gösele, H. Tsuya, editors, Semiconductor Silicon 1998, PV1998-1, The Electrochemical Society, Pennington, NJ (1998), p. 1013.

[195] D.A.P. Bula, W.E. Castro, Jr., V. Stojanoff, F.A. Ponce, S. Hahn, and W.A. Tiller, J. Cryst. Growth 85 (1987) 91.

[196] W. Wijaranakula, J. Appl. Phys. 72 (1992) 2713.

[197] K. Wada, Phys. Rev. B 30 (1984) 5884.

[198] S.K. Bains, D.P. Griffiths, J.G. Wilkes, R.W. Series, G.K. Barraclough, J. Electrochem. Soc. 137 (1990) 647.

[199] L.I. Huang, P.C. Lee, C.K. Hsieh, W.C. Shu, C.W. Lan, J. Crystal Growth 266 (2004) 132.

Author's publications

Patents and applications

[I] D. Lysáček, M. Lorenc, L. Válek, Multilayer gettering structure for semiconductor device and method, US Patent 7,737,004 B2, 2010.

[II] D. Lysáček, J. Vojtěchovská, L. Dorňák, P. Kostelník, L. Válek, P. Pánek, Method of forming a gettering structure and the structure therefor, US patent application 2012/0146024 A1, 2012.

Book chapters

[III] L. Válek, J. Šik, Defect Engineering during Czochralski Crystal Growth and Silicon Wafer Manufacturing, in Modern Aspects of Bulk Crystal and Thin Film Preparation, N. Kolesnikov, editor, In-Tech, Vukovar, Croatia (2012) p. 43–70.

Publications in impacted journals

[IV] D. Lysáček, L. Válek, J. Spousta, T. Šikola, R. Špetík, Thermal stability of undoped polycrystalline silicon layers on antimony and boron-doped substrates, Thin Solid Films 518 (2010) 4052-4057.

[V] L. Válek, J. Šik, D. Lysáček, Enhanced oxygen precipitation during the Czochralski crystal growth, Sol. State Phenom. 131-132 (2008) 167-173.

[VI] L. Válek, D. Lysáček, J. Šik, OISF pattern and grown-in precipitates in heavily boron doped silicon, J. Electrochem. Soc. 154 (2007) H904-H909.

[VII] L. Válek, Š. Stehlík, J. Orava, M. Ďurík, J. Šik, T. Wágner, Limits of the copper decoration technique for delineating of the V-I boundary, J. Phys. Chem. Sol. 68 (2007) 1157-1160.

[VIII] A. Andreev, T. Haber, D.-M. Smilgies, R. Resel, H. Sitter, N.S. Sariciftci, L. Válek, Morphology and growth kinetics of organic thin films deposited by hot wall epitaxy on KCl substrates, J. Crystal Growth 275 (2005) e2037-e2042.

Conference papers and extended abstracts

[IX] L. Válek, Macroscopic signs of crystal structure, in Proceedings of the 21st Joint Seminar Development of Materials Science in Research and Education, K. Koman, V. Jorík, editors, ISBN 978-80-8134-002-4, (2011), p. 72-73.

[X] L. Válek, P. Kostelník, A. Klimsza, Impact of Crystal Originated Defects on Manufacturing of Electronic Devices, in Proceedings of the 20th Joint Seminar Development of Materials Science in Research and Education, K. Nitsch, Z. Kožíšek, editors, ISBN 978-80-254-7237-8, (2010), p. 65-66.

[XI] D. Lysáček, L. Válek, Thermal stability of undoped polysilicon layers, in Proceedings of the 19th Joint Seminar Development of Materials Science in Research and Education, M. Koman, D. Mikloš, editors, ISBN 978-80-89088-81-2, (2009), p. 46-47.

[XII] L. Válek, D. Lysáček, J. Šik, Engineering of defects in heavily boron-doped silicon, in Proceedings of the 19th Joint Seminar Development of Materials Science in Research and Education, M. Koman, D. Mikloš, editors, ISBN 978-80-89088-81-2, (2009), p. 76-77.

[XIII] D. Lysáček, L. Válek, Structural changes of polycrystalline silicon layers during high temperature annealing, in Proceedings of The 11th Scientific and Business Conference, SILICON 2008, Tecon Scientific, K. Vojtechovsky, editor, ISBN 978-80-254-3278-5, (2008) 339.

[XIV] L. Válek, J. Šik, M. Lorenc, Magnetic Czochralski growth of silicon, in Proceedings of the 18th Joint Seminar Development of Materials Science in Research and Education, Czechoslovak Association for Crystal growth (CSACG), K. Nitsch, M. Rodova, editors, ISBN 978-80-254-0564-3, (2008), p. 72-73.

[XV] D. Lysáček, M. Lorenc, L. Válek, Gettering capability and structure of polycrystalline silicon layers, in Proceedings of The 10th Scientific and Business Conference, SILICON 2006, Tecon Scientific, K. Vojtechovsky, editor, ISBN 80-239-7781-4, (2008), p. 408.

[XVI] M. Lorenc, M. Pospíšil, L. Válek, V. Englišová, J. Šik, Advanced Silicon Wafer Manufacturing for Sub-Micron Technologies, in Proceedings of The 10th Scientific and Business Conference, SILICON 2006, Tecon Scientific, K. Vojtechovsky, editor, ISBN 80-239-7781-4, (2006), p. 418.

[XVII] L. Válek, M. Lorenc, J. Šik, Computer simulations of Czochralski silicon growth, (in Czech) in Proceedings of the 4th School of Crystal Growth 2006, Czechoslovak Association for Crystal Growth, Czech and Slovak Crystallographic Association, ISBN 80-901748-8-4, (2006), p. 20-30.

[XVIII] D. Lysáček, M. Lorenc, L. Válek, Structure and gettering properties of polycrystalline silicon layers, in Proceedings of the 16th Joint Seminar Development of Materials Science in Research and Education, Czechoslovak Association for Crystal Growth, Czech and Slovak Crystallographic Association, Praha 2006, ISBN 80-901748-7-6, (2006) p. 40-41.

[XIX] L. Válek, M. Lorenc, J. Šik, Simulations of transient effects during CZ silicon growth, in Proceedings of the 16th Joint Seminar Development of Materials Science in Research and Education, Czechoslovak Association for Crystal Growth, The Czech and Slovak Crystallographic Association, Praha 2006 ISBN 80-901748-7-6, (2006), p. 75-76.

[XX] M. Lorenc, L. Válek, J. Šik, Development of hot zones for Czochralski pulling, in Proceedings of the 16th Joint Seminar Development of Materials Science in Research and Education, Czechoslovak Association for Crystal Growth, The Czech and Slovak Crystallographic Association, Praha, ISBN 80-901748-7-6, (2006), p. 34-35.

[XXI] M. Lorenc, L. Válek, V. Pešat, Silicon wafer gettering ability studied by the method of controlled contamination, in Proceedings of the 15th Joint Seminar Development of Materials Science in Research and Education, Czechoslovak Association for Crystal Growth, ISBN 80-89088-42-2, (2005), p. 42-43.

[XXII] L. Válek, M. Lorenc, J. Šik, Radial distribution of point defects in CZ silicon, in Proceedings of the 15th Joint Seminar Development of Materials Science in Research and Education, Czechoslovak Association for Crystal Growth, ISBN 80-89088-42-2, (2005), p. 72-73.

[XXIII] J. Orava, M. Ďurík, J. Šik, L. Válek, T. Wágner, Technique of OISF-ring Delineating by Copper Decoration, in Proceedings of The 10th Scientific and Business Conference, SILICON 2004, Rožnov p. R., TECON Scientific 2004, K. Vojtěchovský, editor, (2004), p. 46-48.

[XXIV] L. Válek, J. Šik, M. Lorenc, Simulation of Czochralski Silicon Growth: Melt Convection Modelling, in Proceedings of the SILICON 2004, Rožnov p. R., TECON Scientific, (2002), p. 43-45.

[XXV] M. Lorenc, J. Šik, L. Válek, Technologie růstu monokrystalů křemíku Czochralskiho metodou, (in Czech) in Proceedings of the 3rd School of Crystal Growth 2004, K. Nitsch, M. Rodová, editors, Czechoslovak Association for Crystal Growth, MAXDORF Praha, ISBN 80-7345-033-X, (2004), p. 48-57.

[XXVI] L. Válek, J. Šik, M. Lorenc, Computer simulations of melt convection during silicon crystals growth process, in Proceedings of the 14th Joint Seminar Development of Materials Science in Research and Education, Czechoslovak Association for Crystal Growth, MAXDORF Praha, ISBN 80-7345-032-1, (2004), p. 66-67.

[XXVII] J. Šik, M. Lorenc, L. Válek, Control of defects and gettering in Czochralski silicon, in Proceedings of the 14th Joint Seminar Development of Materials Science in Research and Education, Czechoslovak Association for Crystal Growth, MAXDORF Praha, ISBN 80-7345-032-1, (2004), p. 62-63.

Posters

[XXVIII] L. Válek, J. Šik, Defects in Czochralski silicon crystals, at 9th IUVSTA International Summer School on Physics at Nanoscale, Devět skal, Czech Republic, 2008.

[XXIX] L. Válek, J. Šik, D. Lysáček, Enhanced oxygen precipitation during the Czochralski crystal growth,, at Gettering and Defect Engineering in Semiconductor Technology VII, GADEST 2007, Erice, Italy, 2007.

[XXX] L. Válek, Š. Stehlík, J. Orava, M. Ďurík, J. Šik, T. Wágner, Limits of the copper decoration technique for delineating of the V-I boundary, at 7th International Conference Solid State Chemistry, Pardubice, Czech Republic, 2007.

Abreviations

AFM	atomic force microscopy
ASTM	American Society for Testing and Material
COP	crystal originated particle
CZ	Czochralski
DLTS	deep-level transient spectroscopy
DRAM	dynamic random-access memory
EPR	electron paramagnetic resonance
FPD	flow-pattern defect
FTIR	Fourier transform infrared spectroscopy
FZ	float zone
FZ	float zone
GOI	gate oxide integrity
HAc	acetic acid
IR	infrared
MCZ	magnetic Czochralski
MDZ	magic denuded zone
MOS	metal-oxide-semiconductor
OISF	oxidation induced stacking fault
RTA	rapid thermal annealing
SEM	scanning electron microscopy
SC1	standard clean 1
SF	stacking fault
SIMS	secondary ion mass spectroscopy
TEM	transmission electron microscopy
TI	Texas Instruments
VLSI	very large scale integration